

Department of Precision and Microsystems Engineering

Design and realization of a high quality large beam collimator

M.A. Wijnja

Report no : 2021.097
Coach : Dr.ir. L.A. Cacace
Professor : Prof.dr.ir. J.L. Herder
Specialisation : MOOM
Type of report : MSc report
Date : 16 December 2021

DELFT UNIVERSITY OF TECHNOLOGY

**Design and realization of a high quality large beam
collimator**

Author:

M.A. Wijnja

Supervisors:

Ing. G. Aitink-Kroes (SRON)

Dr. R. Huisman (SRON)

Dr.ir L.A. Cacace (TU Delft)

16 December 2021



Contents

Summary	4
List of Figures	5
List of Tables	6
Nomenclature	7
1 Introduction	8
1.1 PLATO	8
1.2 SRON	8
1.3 Test Facility	8
1.3.1 Optical Ground Support Equipment (OGSE)	10
1.3.2 Collimator	12
1.4 Design Objective	12
1.4.1 Exceptions	13
2 Requirements	14
2.1 User Requirements	14
2.1.1 Performance	14
2.1.2 Environmental	14
2.1.3 Physical	15
2.1.4 Organizational	16
2.2 Breakdown	16
2.2.1 Positional Tolerances	16
2.2.2 Alignment	18
2.2.3 Stability	18
3 Design	19
3.1 Concept Design	19
3.1.1 Interfaces	19
3.1.2 Optical Elements	20
3.1.3 Concepts	21
3.2 Detailed Design	32
3.2.1 OAP Assembly	32
3.2.2 Fold Flat Assembly	34
3.2.3 Pinhole Assembly	37
3.2.4 OGSE Structure	42
3.3 Design Validation	43
4 Realization	47
4.1 Assembly	47
4.1.1 Integration of the OAP	47
4.1.2 Integration of Fold Flat Assembly	48
4.1.3 Integration of Pinhole Assembly	49
4.2 Alignment	49
4.2.1 Procedure	50
4.2.2 Report	50
5 Validation	53
5.1 Tests	53
5.1.1 Wavefront	53
5.1.2 Bake-Out	53
5.2 Requirements	53
6 Conclusion and Recommendations	56
6.1 Conclusion	56
6.2 Recommendations	56

Applicable Documents	58
Bibliography	59
A Appendix	60
A.1 Optical Elements	60
A.1.1 Zemax Nominal Design	60
A.1.2 Off-Axis Parabolic Mirror Specifications	61
A.1.3 Fold Flat Specifications	62
A.1.4 Pinhole Plate Specifications	62
A.1.5 Tolerances Collimator Optics	64
A.2 List of Components	66
A.3 Materials	67
A.3.1 Procured Mechanical Components	67
A.4 Assembly	70
A.4.1 Assembly of the Collimator Structure	70
A.5 Alignment	70
A.6 Validation	74
A.6.1 Bake-out	74
A.7 Recommendation Input Optics	77

Summary

With PLATO the European Space Agency (ESA) will launch its third medium-class mission in its Cosmic Vision program. The PLATO satellite consists of 26 optical refractive telescopes where 24 identical wide field cameras form composed images.

Each individual camera must be tested and characterized before being integrated in the satellite. At SRON (Netherlands Institute for Space Research) a thermal vacuum (TV) test facility will mimic the operating conditions of the camera during flight while a star will be simulated by a collimated beam filling the full entrance pupil of the camera.

The aim of this project is to design, build and validate a 150 mm diameter collimator with a $\lambda/4$ wavefront error at 700 nm to be used in the PLATO camera thermal vacuum (TV) test facility at SRON.

A requirement breakdown has been made to further determine the collimator design parameters. Multiple design concepts have been generated for distinct parts of the collimator. After choosing the final concepts, a detailed opto-mechatrical design has been made. In parallel, an alignment procedure was developed.

The designed components have been manufactured, assembled, aligned, and validated. Result after final alignment is a of $\lambda/5.2$ wavefront error at 700 nm over a 150 mm diameter beam, well within the requirement for optical performance.

As the final step of the integration, the collimator has been installed in the TV test facility at SRON where it is now fully operational.

List of Figures

1	Render of the PLATO camera [AD3]	9
2	Cut view of the PLATO camera (colored) mounted to the test structure and inside the TV tank. [AD3]	9
3	PLATO camera in its cryogenic compartment. The overall environment inside the tank and that of the support structure will remain at room temperature. [AD3]	10
4	Complete OGSE light stimulus, the elements of the OGSE are marked in orange. [AD3]	10
5	Real-time LoS measurement of the alignment cubes. Using a theodolite.	12
6	ZEMAX model, used for Δx , Δy and Δz tolerance analysis. [AD4]	16
7	Coordinate systems of the optical components of the collimator, with dimensional parameters. Accurate optical parameters can be found in App. A.1.1	17
8	Schematic overview of the OAP subsystem. OAP diameter is 170 mm	21
9	Trade off table of axial holding mechanisms	22
10	Trade off table of radial holding mechanisms	25
11	Schematic representation of the FF subsystem. The reflective side of the optic is marked in red. Diameter optic: $D_{FF} = 101.6$ mm.	27
12	Two approaches of xy DoF behaviour.	29
13	Vacuum compatible Thorlabs xy -stage. [1]	29
14	Z-motion trade off.	30
15	Overview of OAP assembly. Diameter optic, $D_{OAP} = 170$ mm	32
16	OAP Reference flat with 3 wave washer. Optic diameter $D_{ref} = 25.4$ mm	33
17	Fold flat(FF) assembly. Diameter optic, $D_{FF} = 101.6$ mm	34
18	Locking ring holding the fold flat in place.	35
19	Results of a parametric sweek, using COMSOL Multiphysics 5.6.	36
20	CREO parametric FAE approximations of the fold flat preload ring. Outer diameter of the preload ring is $D_0 = 105.8$ mm.	37
21	Overview of the pinhole assembly. The black xy flexure stage has outer dimensions of 40 mm	37
22	Side view of pinhole stage assembly, with flexible element providing z-motion in red.	38
23	Thermal expansion difference compensators under deflection. Units are in [MPa]	39
24	CREO parametric FAE approximations of the pinhole z stage flexure.	40
25	Pole clamp under loading	42
26	Collimator structure. Overall length of collimator structure front to back is ~ 610 mm	42
27	Cut views of the collimator with subassemblies and light path, which originates from the pinhole assembly. Including the subassemblies, overall length is ~ 750 mm	43
28	Deflection of the OAP's reflective surface under gravity load. Units are in [m]. Diameter of the Optic $D_{OAP} = 170$ mm	44
29	OAP under axial and radial loading. Units are in [m]. Diameter of surface under test $D = 150$ mm	45
30	Fold flat under axial loading. Units are in [m]. Diameter of surface under test $D = 91.4$ mm.	45
31	Fit checking the OAP subassembly in the collimator structure.	48
32	Schematic representatio of step by step procedure of placing the fold flat in its retainer.	48
33	Implementation of fold flat placement strategy during assembly.	49
34	Pinhole subsystem being assembled and integrated.	49
35	Summary of averaged WFE results.[AD2]	51
36	Physically checking the digital mask definition	52
37	Pictures of carrying out the alignment procedure [AD2].	52
38	ZEMAX software screenshot of nominal positioning of optical components. Top: Lens Data Editor window. Bottom: Schematic representation of collimator layout.	60
39	Test data from the manufacturer or the off-axis parabolic mirror. [2]	61
40	Individual tolerance on optical element sensitivities	64
41	CAD representation of Thorlabs XY flexure stage. [1]	67
42	CAD representation of the M6 x 0.25, 25 mm adjustment screw from Thorlabs. [1]	68
43	CAD representation of the M6 x 0.25 bushing from Thorlabs. [1]	68
44	CAD of the wave washer from Amatec. [3]	69
45	CAD of the tension spring from Amatec. [3]	69
46	Assembly of the collimator structure	70
47	Theodolite alignment views.	71
48	Autocollimator. Black ocular is used for measurement.	71

49	Autocollimator in use.	72
50	External using the theodolite as explained in Sec. 1.3.1.	72
51	Measurements during external alignment.	73
52	Offset of fold flat LoS with respect to Collimator LoS	74
53	Offset of the Alignment Cube LoS with respect to Collimator LoS	75
54	Offset of the Alignment Cube LoS with respect to OAP Reference Mirror LoS	76
55	Proposed input optics fiber coupling	77

List of Tables

1	Table of abbreviations	7
2	Table of collimator performance requirements	14
3	Table of environmental collimator requirements	14
4	Table of collimator physical requirements	15
5	Table of organizational requirements	16
6	Point source tolerances [AD4]	17
7	Dimensional parameters as used in Fig. 7. Accurate optical parameters can be found in App. A.1.1	17
8	Overview of tolerances for single element, single DoF perturbations. More in App. A.1.5	17
9	Interfaces of the collimator and the applicable physical regimes	19
10	Specifications of the off-axis parabolic mirror. More specifications can be found in App. A.1.2 [2]	20
11	Specifications of the fold flat [4]. More specifications can be found in App. A.1.3	20
12	Dimensional specifications of the pinhole foil [1]. More material specifications can be found in App. A.1.4	20
13	Offsets of OAP Reference LoS with respect to the OAP optical axis in the OAP coordinate system [AD2]	50
14	Offsets of OGSE Cube with respect to the OGSE LoS in the OGSE coordinate system. [AD2]	52
15	Difference in LoS offsets before and after bake-out	53
16	Table of collimator performance requirements.[AD2]	53
17	Table of environmental collimator requirements.	54
18	Table of collimator performance requirements.	54
19	Table of organizational requirements [AD4]	55
20	Specifications of the OAP catalog.	61
21	Specifications of the fold flat. [4]	62
22	Specifications of the pinhole foil [1].	62
23	Overview of the parts of the collimator assembly. [P/M] denotes whether the component is being manufactured inhouse or being procured. If the material is not specified, the component is either procured or manufactured of Al 6082-T6. *Detailed design not introduced in this thesis.	66
24	Specifications of the xy flexure stage from Thorlabs. [1]	68
25	Specifications of the M6 x 0.25, 25 mm adjustment screw from Thorlabs. [1]	68
26	Specifications of the M6 x 0.25 bushing from Thorlabs. [1]	69
27	Specifications of the wave washer from Amatec. [3]	69
28	Specifications of the tension spring from Amatec. [3]	70

Nomenclature

Abbreviation	Definition
COTS	Commercial Off-The-Shelf
CA	Clear Aperture
CAD	Computer Aided Design
CTE	Coefficient of Thermal Expansion
DOF	Degree(s) Of Freedom
EM	Engineering Model
ESA	European Space Agency
FEA	Finite Element Analysis
FEM	Finite Element Method
FF	Fold Flat
FM	Flight Model
FoV	Field of View
IAS	Institut d'Astrophysique Spatiale
IF	Interface(s)
INTA	National Institute for Aerospace Technology
JAXA	Japan Aerospace Exploration Agency
LoS	Line of Sight
MOC	Molecular Contamination
NASA	National Aeronautics and Space Administration
NWO	Netherlands Organisation for Scientific Research
OAP	Off Axis Parabolic (Mirror)
OFP	Object Focal Plane
OGSE	Optical Ground Segment Equipment
OMTE	Optical, Mechanical, Thermal and Electrical
PAC	Particulate Contamination
PLATO	PLANetary Transits and Oscillations of stars
PP	Pinhole Plate
QM	Qualification Model
SNR	Signal to Noise
SRON	Netherlands Institute for Space Research
TV	Thermal Vacuum
TEB	Thermal Environmental Box
TOU	Telescope Optical Unit
WFE	Wave Front Error

Table 1: Table of abbreviations

1 Introduction

1.1 PLATO

With PLATO the European Space Agency(ESA) will launch its third medium-class mission in its Cosmic Vision program. This mission will study extrasolar planetary systems, with emphasis on the properties of terrestrial planets in the habitable zone around solar-like stars. Hence the mission name PLAnetary Transits and Oscillations of stars (PLATO). This satellite, functioning as space telescope, will gaze at the light of thousands of stars for several years to find dips in intensity which would reveal a planet passing in front. By measuring the depth and duration between transits scientists can obtain information from the planet passing in front, such as its size distance from the host star.

The satellite will be able to stare uninterrupted at the stars for years. This will produce a large, long term data set, which enables astronomers to be able to find small planets with long transit periods. Such as Earth-sized planets in the so-called “habitable zone” around stars similar our Sun. Furthermore the PLATO mission will also shed some light on the statistics of the architecture of planetary systems. In short, the unique properties of PLATO enables a comparison of other planetary systems to our own solar system, and will yield crucial insight in further understanding the universe and the dynamics involved in how planetary systems form and evolve.

The PLATO satellite consists of 26 optical refractive telescopes each with an outer diameter of 200 mm. The telescopes have a mostly overlapping, Field of View(FoV) of $\sim 1100deg^2$ each. The specific arrangement of the cameras allows a total very large FoV of about $2230deg^2$, with a sensitivity similar to a 1 m-class telescope. Four sets of 6 camera’s form composed images with a sample rate of 25 seconds which are combined to observe low frequency phenomena. The other 2 "fast" imaging telescopes will be used to locate and track the astronomical system in survey, imaging every 2.5 seconds. Observed light over multiple cameras allows a high signal-to-noise ratio (SNR) and observation of many stars simultaneously.

As a single observation of a region in space can last for up to two years, the cameras are required to operate at extreme stability, this in order to make sure that the measured fluctuations in the signal are produced by the change in intensity of the stars and not of internal artefacts. It is vital to the space mission to know exactly how every individual camera behaves. Before flight each camera is carefully characterized at the harsh space flight environment.

Testing the cameras in series at a single facility, would require a lead time of over 3 years for the full series of cameras. Therefore testing has been divided into three batches in order to allow parallel testing, thus reducing the total lead time by a factor 3. Institutes in Europe performing the tests are based in France (IAS), Spain (INTA) and Netherlands Intitute for Space Research (SRON) in The Netherlands. SRON performs the validation of the engineering model (EM) and one third of the 24 telescopes flight models (FM). [5] [6] [AD3]

1.2 SRON

Since its foundation, in the early 1960’s, the Netherlands Institute for Space Research(SRON) advises the Dutch government as part of the Netherlands Organisation for Scientific Research (NWO). SRON often had a leading role in pioneering, coordinating, and developing fundamental key contributions to advanced space instruments for missions of the major space agencies; ESA, NASA, and JAXA. These contributions have enabled the national and international space-research communities to explore and pursue fundamental astrophysical research, Earth science and explanatory research.

SRON has two locations, Leiden and Groningen, respectively housing 3/4 and 1/4 of the employees. The Leiden establishment is located on the campus of the Leiden University. The Groningen branch is located on the Zernike campus of the University of Groningen. [6]

1.3 Test Facility

The PLATO satellite will house 26 camera’s, Fig. 1, with identical Telescope Optical Units (TOU), each consisting of 6 lenses. Front mounted baffles are placed to provide unobstructed optical input to each camera on the spacecraft. The baffle acts as a radiator to deep space providing a nominal operating temperature between $-90^{\circ}C$ and $-70^{\circ}C$. The cameras are focused through thermal contraction, by varying the internal temperature. The 2 "fast" cameras have different frame transfer CCDs and therefore different, more heat generating, front

end electronics. This relative extra heat transfer requires the satellite to have different thermal coupling on the front end of the craft, translating into different baffling and thermal strapping compared to the normal slow camera's. The cameras are mounted on a shared optical bench, where each camera is held using individual bipods.



Figure 1: Render of the PLATO camera [AD3]

The test set-up will be placed in a vacuum tank, see Fig. 2 for a cut view of the set-up. The camera is mounted to a gimbal to rotate over the camera's large FoV in the entrance pupil. When the camera is rotated in its entrance pupil plane, the set-up is insensitive to lateral positional inaccuracies. It is important that the entrance pupil remains filled at all circumstance. The gimbal and light stimulus, which will remain stable, are rigidly connected by the support structure, Fig. 4.

The camera resides in a local thermal environment, which can be seen in Fig.3. The parts represented in blue are the cryogenic components which mimic flight conditions. The rest of the structure, in red, will remain at room temperature.

While servicing the camera, a cleanroom ISO 5 environment is required to meet camera cleanliness requirements. To respect building restrictions, this was cleverly done by using the spacial placement in the building

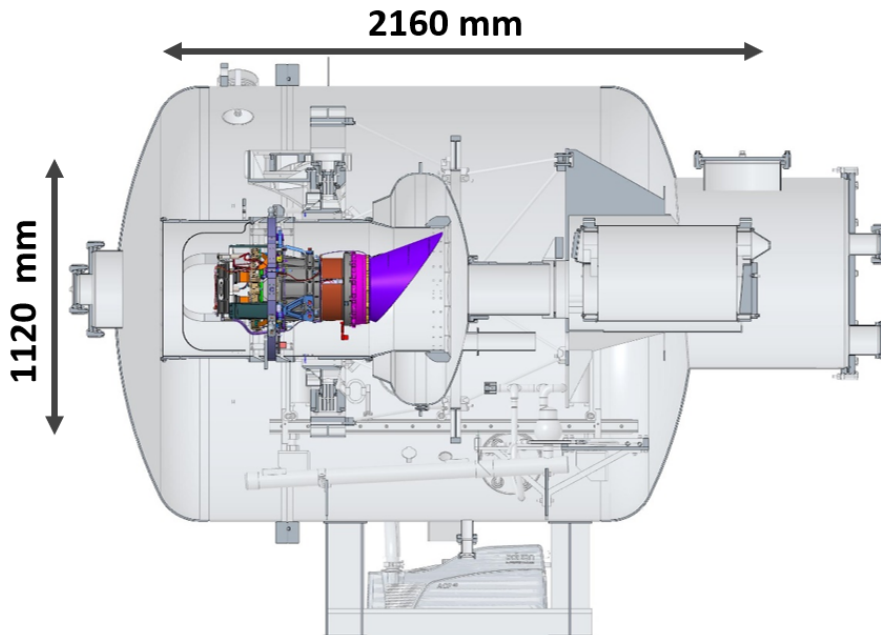


Figure 2: Cut view of the PLATO camera (colored) mounted to the test structure and inside the TV tank. [AD3]

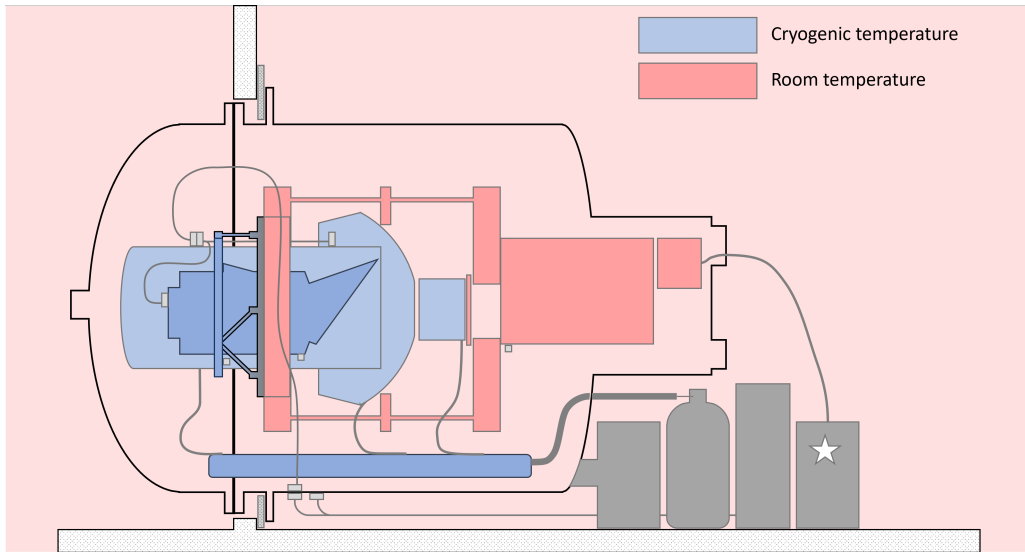


Figure 3: PLATO camera in its cryogenic compartment. The overall environment inside the tank and that of the support structure will remain at room temperature. [AD3]

1.3.1 Optical Ground Support Equipment (OGSE)

The OGSE spans all the optical equipment to support the testing of the PLATO camera. In Fig. 4 a clear overview of the test facility is given, with the components of the OGSE marked in orange. [7] [AD3]

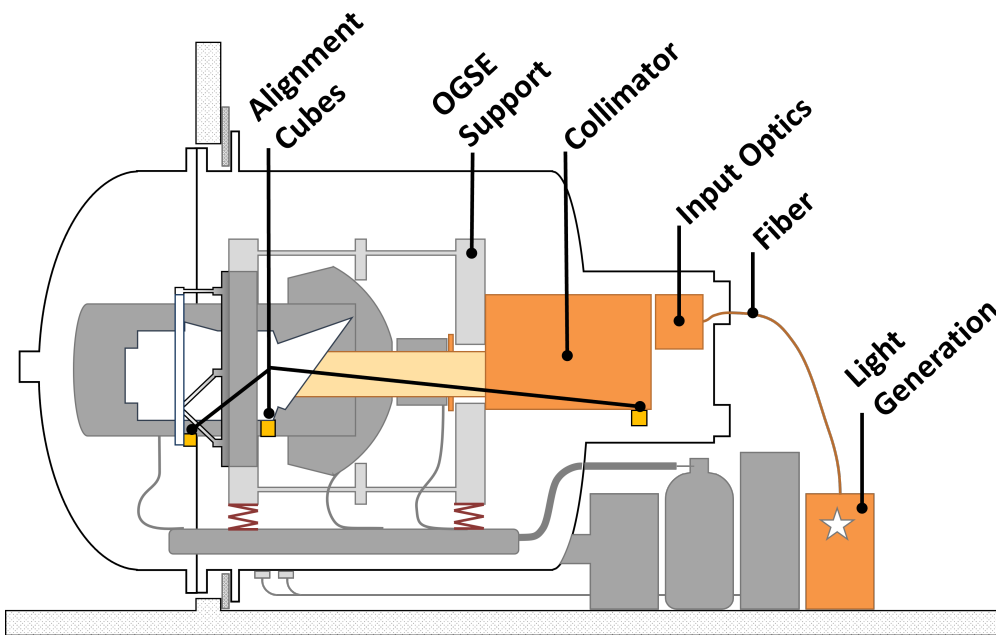


Figure 4: Complete OGSE light stimulus, the elements of the OGSE are marked in orange. [AD3]

Beam Oversizing

To guarantee a fully filled entrance pupil under all circumstances, the light beam is oversized by a generous 15 mm. Thus relaxing translational sensitivity from uncertainties in camera mounting and potential parasitic translational decenters from a gimbal nulling procedure. [AD3] [AD5] [AD6]

Outside Tank

Clear benefits for components outside the vessel is that they will not have to comply to operation in a high vacuum or required clean environment. The following *Light Generation* and *Attenuation* of the OGSE are located outside of the tank, see Fig.4.

Light Generation

A broadband, laser-driven light source provides the required light input. The most important properties of this light source are its spectral coverage, high stability and long operational life. The output is directly coupled to an optical fiber. [AD5]

Attenuation

After this initial light generation the light passes a double reflective collimator set-up with a two filter wheel system in between for attenuation purposes. Optical fibers provide further transport to the fiber-feedthrough into the tank. The fibers used are multi-mode optical fibers. [8] [9] [AD5]

Inside the Tank

From a fiber-feedthrough the light is passed through a multi-mode vacuum compatible optical fiber inside the tank. This fiber feeds the light into the collimator input optics. The components of the OGSE inside the vacuum tank interface directly to the collimator. The collimator is kinematically mounted onto the support structure, Fig. 4.

Input Optics

From the multi-mode fiber the photons are led to the input optics subsystem. Here the pinhole will define the object focal plane (OFP). The input optics is not part of the collimator and therefore considered a separate subsystem although it interfaces directly to the collimator, Fig. 4. [AD5]

Collimator

The light defined by the pinhole is collimated into the required 150 mm light beam, Fig. 4. [AD3] [AD5]

External Metrology

Aside from the main optical science path, there is an external metrology path. Alignment cubes are added onto the PLATO camera (CAM Cube), mounting structure of the PLATO camera (MaRi Cube) and the structure of the collimator (OGSE Cube). Each alignment cube's line of sight (LoS) has a known offset with respect to the camera and collimator's LoS. By measuring the LoS of the cubes, using e.g. a theodolite, the actual LoS alignment between the camera and the collimator can be calculated. These offsets can be corrected by rotating the camera using the gimbal system. The camera team is responsible for the camera cubes characterization. SRON is responsible for the collimator cube characterization. [10] [AD3]

Figures of performing the external metrology can be found in App. A.5.

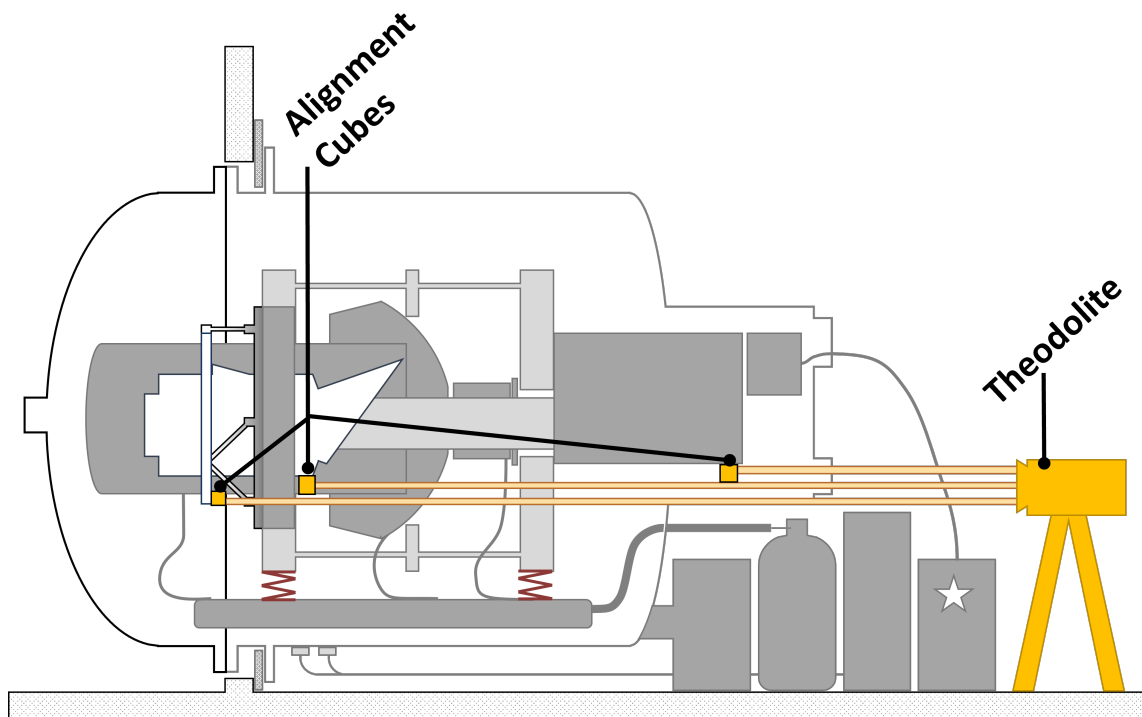


Figure 5: Real-time LoS measurement of the alignment cubes. Using a theodolite.

1.3.2 Collimator

The collimator is based on a single off-axis reflective design. An off-axis parabolic mirror(OAP) collimates light from a point source located in the object focal plane(OFP) of the OAP. In order to reduce overall size of the collimator, a fold flat has been added.

1.4 Design Objective

Main Objective

Provide final design, realize and characterize a 150 mm diameter collimator with a wavefront error of $\leq \lambda/4$ at 700 nm.

The primary objective of this thesis is to design, build and validate a large beam, high quality collimator for the PLATO camera TV test facility at SRON. Before final integration in the satellite, the engineering model camera requires approval testing and each flight model camera needs to undergo acceptance testing and calibration. The specific test set-up will be used to test and characterize each single camera separately. The TV test set-up will mimic the operating conditions during flight while a star will be simulated by a collimated light beam filling the full entrance pupil of the camera, thus providing a point source at infinity.

The collimator has to perform in an ambient temperature, high vacuum environment and under extreme cleanliness requirements. The camera (test specimen) will be held in an local cryogenic container. In this harsh environment the collimator needs to be fed by a very well characterized on axis point source. Moreover, an extreme stability of beam direction and wavefront error during the testing procedures is required.

Secondary Objectives

Determine the requirements further for crucial levels of design

The collimator is part of a larger set-up, which is designed to specific requirements. The global requirements translate into requirements for each level of each subsystem. The global conceptual design choices influence the subsystem requirements. Thus further exploration of the requirements on each level of design for the collimator is therefore crucial.

Generate opto-mechanical design for all optical components of the collimator

First conceptual opto-mechanical approaches will be conceived for the collimator and alignment tooling. The concepts will be explored and their effect of overall design will be analyzed.

After concept selection, a detailed opto-mechanical design will be generated.

Design alignment and validating procedures for the collimator

To ensure realization the necessary procedures will be generated, such as a validation procedure. If required an alignment procedure will be constructed. Interfaces for connecting components will be provided.

Realize, manufacture, assemble and characterize the collimator

The collimator has to be realized and validated for the required optical performance under the given conditions. Furthermore, the collimator has to be characterized and integrated in the test facility.

1.4.1 Exceptions

The entire test facility is a complex and demanding system, it is appealing to extend research and design in other adjacent problems and areas, that are not crucial for completion of the main objective. Therefore, clear boundaries are noted below:

- This thesis will not focus on the light source generation. The last interface will be the pinhole plate, where only mounting and aligning the central pinhole is considered. Other optical properties will not be considered. A short feasibility analysis regarding the mechanical mounting and volume claim will be in order. This will eventually be necessary for the mounting interface between the collimator and its input optics. This includes presenting a well-defined interface surface for the optical elements in front of the pinhole plate.
- Design for wiring and connectors are not included in this thesis.
- Any analysis on components that are not part of the collimator and/or the alignment tooling will not be considered in this thesis.
- Thermal effect due to camera environmental box will not be included in this thesis. The collimator is expected to perform at a constant room temperature.

2 Requirements

2.1 User Requirements

The user requirements have been arranged into the following 4 categories: performance, environmental, physical and organizational requirements. The performance metric contains the optical performance that has to be optimized. Environmental requirements comprises the surrounding boundary conditions. Physical requirements specify the physical boundary conditions of the collimator. Lastly, the organizational requirements specify the boundaries from the project besides engineering, like time and budget.

2.1.1 Performance

Property	Requirement	Remark
WFE (peak-to-valley)	$\leq \lambda/4$ at 700 mm	Acceptable WFE on camera pupil plane [AD3] [AD4]

Table 2: Table of collimator performance requirements

Wavefront Error (WFE)

The WFE is the key metric for required optical quality. WFE is measured in peak-to-valley distance of the wavefront phase surface contour. To characterize and validate the WFE a specific procedure has to be designed and performed. [10] [AD3]

2.1.2 Environmental

Property	Requirement	Remark
Temperature	20°C	Temperature CAM during handling and testing [AD3]
Pressure	1 mPa	During testing [AD3] [AD5]
Cleanliness		Stable after bake-out (20°C – 100°C cycle), [AD7] [AD8] Handling according to cleanliness protocols. [AD6] [AD7] [AD8]

Table 3: Table of environmental collimator requirements

Temperature

The collimator will be placed in the vacuum vessel where ambient room temperature applies, Fig. 3. Only the camera will face the harsh thermal regimes. Therefore the temperature influences will not have to be taken into account for the collimator design. However, thermal insensitivity may need to be proven. [7] [AD3] [AD5]

Pressure

There are specific demands on the design when used in a high vacuum environment, the following aspects are essential: [11] [12] [13]

- **Outgassing**, also called desorption, is the release of gas molecules that are captured inside the material. Gas molecules can get enter when the material is exposed to atmospheric pressure or be inherently part of the material such as softeners in polymers. The outgassing rate highly depends on the time, temperature and pressure. Outgassing can be reduced through a bake-out prior to use in a vacuum chamber. As the term suggest, elevated temperatures (normally $\sim 100^\circ\text{C}$) are used. Outgassing requirements influence the material choice for vacuum use.
- **External leaks** are where external gasses seep in the vessel, e.g. via seals, holes, diffusion etc. Therefore caution is to be taken to avoid damage to the tank, seals, feedthroughs or other vacuum-related equipment.
- **Virtual leaks**, are as the name implies no real external leaks. A virtual leak is a source of gas that is physically trapped within the vacuum chamber that cannot easily be pumped out. For example from, gaps, cracks, surface contacts, contaminations like finger prints, or other volumes of trapped gas inside the vessel. The presence of a virtual leak generally becomes apparent when the correct system pressure takes an excessive amount of time to reach or will not be reached at all.

Cleanliness

There are two main mechanisms of contamination: Molecular Contamination and Particulate Contamination. Contamination of the test article is based on the accumulative build-up of contaminants of a period of time. A cleanroom ISO classification specifies the maximum acceptable amount of airborne particles of a certain particle size per cubic meter. Besides requirements on the size and type of contamination, the accumulative build up over time adds up to a requirement on handling and operating in a certain cleanroom class environment.

To monitor the contamination levels, a molecular contamination (MOC) and particulate contamination (PAC) sample always accompanies the corresponding hardware.

The test facility has been designed to be cleaned in between every camera change by means of cycling through a bake-out procedure consisting of elevating the ambient temperature to $\leq 100^\circ\text{C}$ in a vacuum. This will ensure that the molecular contamination can be kept to a minimum for each camera. This can take multiple days to complete.

This ability to be baked-out will be the primary decontamination requirement of the collimator.[10] [14] [AD6] [AD7] [AD8]

2.1.3 Physical

Property	Requirement	Remark
Exit beam diameter	150 mm	This includes 15 mm oversizing [AD5]
Volume envelope ($\varnothing \times L$)	394 X 900mm	Interface with support and Tank [15]
Mass	15 kg	Due to support interface
Angular beam stability	0.1 <i>arcsec</i>	Long term stability 1σ
Translational accuracy	2 mm	Lateral positioning
External Alignment		Fully characterized alignment cube [AD3]
Integration	\varnothing 651 mm	mount onto support [AD3] [AD6]

Table 4: Table of collimator physical requirements

Output beam diameter

The requirement on exit beam diameter of the collimator is determined by the camera’s nominal entrance pupil size, expected lateral perturbations due to gimbal nulling, camera misalignment and parasitic effects due to misalignment of the gimbals axis of rotation with the camera’s entrance pupil.

Therefore an oversizing of 15 mm is implemented on top of the camera’s nominal 135 mm entrance pupil. Adding up to a required 150 mm. [10] [AD3] [AD5]

Volume envelope

Volume envelope is determined by the support structure design and vacuum vessel dimensions. An envelope of ($\varnothing \times L$) 394 x 900 mm is available for the collimator and the input optics. This being said, care should be taken to allow sufficient space for the input optics in the tank.[7] [AD3] [AD5]

Mass

The maximum mass is 15 kg.[AD3] [AD5]

Angular beam stability

Angular positioning misalignment of the collimator LoS and the camera LoS can be corrected for using the gimbal rotation, Sec. 1.3. Therefore only the long term stability of the collimator LoS is crucial for successful testing of the PLATO camera. The value found in Tab. 4 is the collimator budget for long term stability.

The camera test procedures contain very long integration time routines, over which a stable light stimulus is expected. [10] [AD3] [AD5]

Translational accuracy

Lateral positioning limits the decenter of the output beam with respect to the PLATO camera. The lateral optical axis alignment accuracies are accounted for in the 15 mm collimator output beam oversizing. Therefore the camera is insensitive to its axial location into the collimated beam.

Of the aforementioned 15 mm, 2 mm has been allocated to the lateral positional accuracy of the collimator. [10]

[AD5]

External alignment

For external alignment, the offset of the LoS of the collimator has to be characterized with respect to the LoS of the alignment cube on the test specimen, Sec. 1.3.1. [10] [AD3] [AD5]

Integration

The collimator will be integrated in the vacuum vessel via a port in the tank. Thus the maximum dimension is limited by this port diameter and support structure to \varnothing 651 mm. Furthermore, the collimator has to be mounted onto the support structure. [10] [AD3] [AD5]

2.1.4 Organizational

Property	Requirement	Remark
Time	5 October 2021	Working aligned model
Cost	€30.000,-	Budgeted by project leader

Table 5: Table of organizational requirements

Time

The test facility is to be ready before the first test of the Engineering Model(EM).

Cost

The budget is for procurement of the collimator and alignment tooling hardware. The number is excluding personnel costs.

2.2 Breakdown

2.2.1 Positional Tolerances

The performance metric is WFE with a known tolerance. It is difficult to decouple the WFE into positional tolerances of each DoF of the individual optical components.

However, a detailed WFE analysis of the OGSE collimator by SRON can be utilized, [AD4]. In this analysis, the collimator's optical performance (without a folding flat) has been translated into point source alignment with respect to the off-axis parabolic mirror, Fig. 6. Thus determining an alignment tolerance of the point source in Δx , Δy and Δz . The positional tolerances can be seen in Tab. 6

The coordinate system of the OAP, as seen in Fig. 7 is set as such that the optical axis (z) is the LoS of the collimated beam. This coordinate system orientation is also used by the OAP's manufacturer Optical Surfaces Limited in its alignment procedures. [16]

More importantly, Δx , Δy and Δz misalignment, can be translated into individual DoF misalignment of each of the collimator optical components.

With the geometry of the optical path as presented in Fig. 7 and Tab. 7 individual tolerance budgets for misalignment of the optical components can be calculated. See Tab. 8 for the critical Degrees of Freedom (DoF's), the complete table can be found in App. A.1.5.

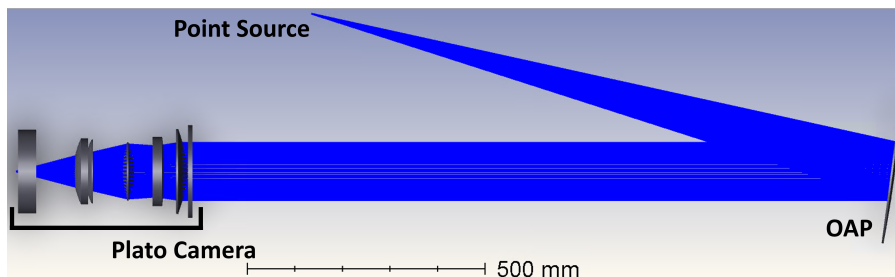


Figure 6: ZEMAX model, used for Δx , Δy and Δz tolerance analysis. [AD4]

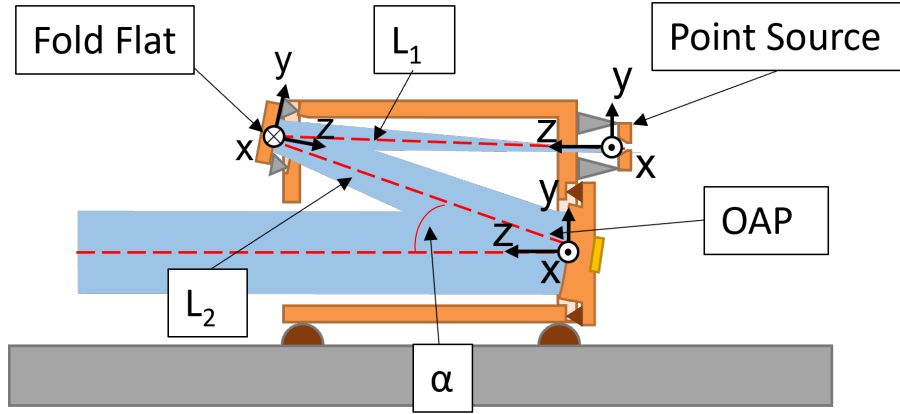


Figure 7: Coordinate systems of the optical components of the collimator, with dimensional parameters. Accurate optical parameters can be found in App. A.1.1

DoF	Value
Δx	30 μm
Δy	30 μm
Δz	50 μm

Table 6: Point source tolerances [AD4]

Parameter	Value
α	15°
L_1	670 mm
L_2	600 mm

Table 7: Dimensional parameters as used in Fig. 7. Accurate optical parameters can be found in App. A.1.1

	x_i	Tolerance	Notes
OAP	x	30.0 μm	Defocus effects due to θ_x and θ_y are negligible* 0°0'5.14" 0°0'10.3" 0°0'10.3"
	y	30.3 μm	
	z	50.4 μm	
	θ_x	0.001 43°	
	θ_y	0.002 86°	
	θ_z	0.002 86°	
Fold Flat	x	N.A.	0°0'9.24" 0°0'9.24"
	y	N.A.	
	z	24.8 μm	
	θ_x	0.002 57°	
	θ_y	0.002 57°	
	θ_z	N.A.	
Focal Point	x	30.0 μm	Coordinate system of focal point coincides with simulated point source
	y	30.0 μm	
	z	30.0 μm	
	θ_x	N.A.	
	θ_y	N.A.	
	θ_z	N.A.	

Table 8: Overview of tolerances for single element, single DoF perturbations. More in App. A.1.5

*Defocus (Δz) effects due to θ_x and θ_y are negligible as they are subject to the cosine effect.

2.2.2 Alignment

When regular production tolerances are insufficient to ensure the required optical performance an alignment strategy is needed. The tolerances specified in Tab. 8, are already very strict for each optical surface, without even considering the actual tolerance build-up of supporting structures.

The collimator structure is expected to span ≥ 700 mm, Fig. 7. It is unrealistic to expect such a large structure, with multiple components to reach the required alignment (of Tab. 8) with doable manufacturing tolerances only. Thus alignment of optical components is necessary.

2.2.3 Stability

The set-up support structure provides a stable platform during testing, ensuring a rigid connection between the collimator and the gimbal. Long term performance stability is needed after the required periodical bake-out procedures, Sec. 2.1.2, and camera changes. Thus, the collimator needs to remain accurately aligned and its function verified, after each of said bake-out procedures. It is crucial to verify that the collimator still performs accordingly after a bake-out cycle.

3 Design

3.1 Concept Design

3.1.1 Interfaces

The interfaces(IF) of the collimator can be separated into the following 4 categories. Where each abbreviation denotes a physical regime.

- [O]ptical
- [M]echanical
- [T]hermal
- [E]lectrical

	Collimator	Camera	OGSE Support	Vessel	Alignment Tooling	Alignment Cube	Test Bench Set-up	Input Optics	Hartman Mechanism	Sensors	Wiring
Collimator	-	OT	M	M	OM	OM	M	OM		M	ME
Camera		-				OM		O	O		
OGSE Support			-	M		M	M		OME	ME	M
Vessel				-				M			
Alignment Tooling					-	OM	M	O			
Alignment Cube						-	M	O			
Test Bench							-				
Input Optics								-		O	OE
Hartman Mechanism									-	ME	M
Sensors										-	E
Wiring											-

Table 9: Interfaces of the collimator and the applicable physical regimes

Highlighted Interfaces

Important interfaces will be explored further below.

Collimator - Input Optics

The most important IF is that of the collimator and the input optics, shown in Fig. 4. The input optics as a separate subsystem is mounted onto the collimator. However, the optical mask (within the input optics subsystem) needs to be mounted accurately and with high stability onto the collimator. [AD3] [AD5]

Collimator - Support Structure

The interface of the OGSE support and the collimator is important, Fig. 4, as this positions the whole subsystem. Essential is that the collimator is mounted without introducing any stresses. Internal stress may cause deformations and thus introduce variance between the alignment phase and operation phase. [17] [AD5]

Collimator - Alignment Tooling

When directly taken into account in the design, integrated interfaces for alignment tooling will streamline the alignment process.

3.1.2 Optical Elements

Off-axis parabolic mirror

The OAP is manufactured by Optical Surfaces Limited [2]. To reach an output beam quality of $\lambda/4$, the surface quality of the OAP needs to be twice as good (at least $\lambda/8$) as a reflective surface doubles the WFE. A test report the manufacturer can be found in App. A.1.2.

Diameter	170.08 mm
Clear Aperture	≥ 150 mm
Focal Length	1250.8 mm $\pm 1\%$
Apparent Focal Length	1272.9 mm
Off-Axis Angle	15.16°
Edge Thickness	~ 23 mm
Surface Flatness	$\lambda/8$ at 633 nm

Table 10: Specifications of the off-axis parabolic mirror. More specifications can be found in App. A.1.2 [2]

The aforementioned test report specifies the performance of the OAP well, however this is poorly linked to the mechanical interfaces. Optical alignment is therefore not easily obtained by the OAP’s non-reflective physical boundaries. The location of the off-axis vertex is crudely marked on the OAP’s side surface. For integration purposes the optical axis will have to be determined. A characterization procedure is required, as well as a mechanism to store the found LoS for subsequent integration in the collimator itself. The characterization will be further described in Sec. 4.2 and separate the Alignment Procedure [AD1].

Fold Flat

A reflective flat is used to fold the optical path allowing for a more compact design. A surface flatness of $\lambda/10$ peak to valley has been selected, to not introduce any significant WFE. Appropriate clear aperture and uniformity specifications over the required wavelength range leads to this specific *1inch* flat of manufacturer Edmund Optics Inc. The following specifications in Tab. 11 and additional specifications in App. A.1.3 apply. [4] [AD3]

Diameter	101.6 mm +0.0-1.0 mm
Clear Aperture	91.44 mm
Edge Thickness	19.10 m ± 1.5 mm
Surface Flatness	$\lambda/10$ Peak to Valley
Substrate Material	Zerodur

Table 11: Specifications of the fold flat [4]. More specifications can be found in App. A.1.3

The optical surface quality allows for ease determining the flat’s LoS, using alignment equipment, e.g. a theodolite or an autocollimator the orientation can be measured. Moreover, the flat’s substrate material, Zerodur, is transparent. The reflective surface is comprised of a metallic coating, App. A.1.3. This enables to take a LoS measurement from the rear of the flat as well, through the substrate material measuring the rear surface of the coating. [5]

Pinhole

The focus of the OAP is defined by a pinhole. This circular aperture defines the x , y and z location of this virtual point source that illuminates the OAP. It is custom that pinholes are delivered as a foil assembled in a mounting supplied by the manufacturer. The foil can be removed from its mount and used directly. The foils dimensional specifications can be found in Tab. 22. Additional material specifications can be found in App. A.1.4. [1] [AD4]

Diameter foil	9.6 mm
Diameter aperture	$30 \mu\text{m} \pm 2 \mu\text{m}$
Foil thickness	50 μm

Table 12: Dimensional specifications of the pinhole foil [1]. More material specifications can be found in App. A.1.4

3.1.3 Concepts

In this chapter, opto-mechanical mounting concepts for each optical component, including the pinhole, are provided. The concepts shown do not represent a detailed solution but a design approach to aid further detailing.

Note that the concepts are compared relative qualitative measures, on performance. No quantitative analyses have been performed.

Mounting Off-Axis Parabolic Mirror

A schematic overview of the OAP in its subsystem, Fig. 8. This assembly mounts the optical element, provides a reference and introduces the required off-axis angle.

Specifications of the optical component can be found in Tab. 10 and in App. A.1.2.

Retaining the optic can be broken apart in radial and axial mounting.

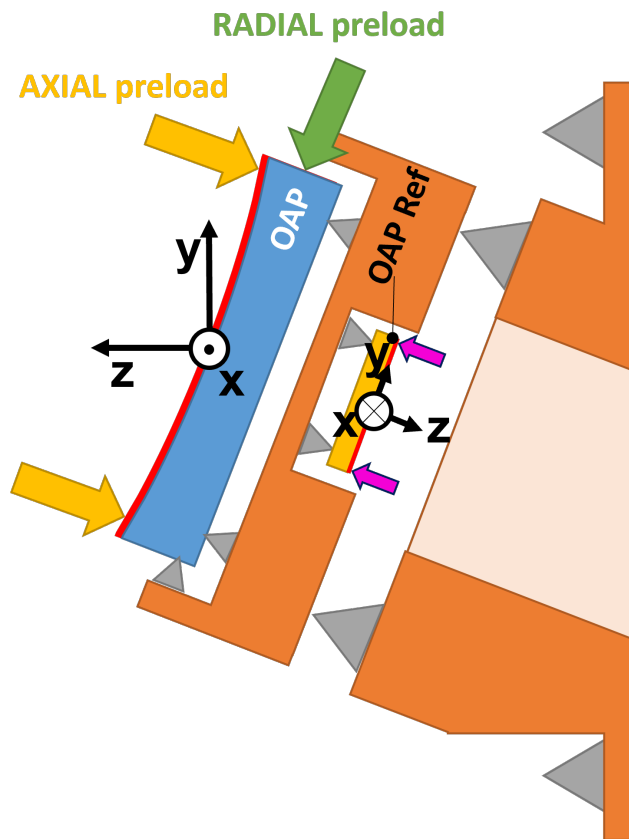


Figure 8: Schematic overview of the OAP subsystem. OAP diameter is 170 mm

Axial trade off

Retaining the off-axis parabolic mirror in axial direction poses some challenges. Firstly the reflective surface of the OAP is not flat. Therefore, it is not possible to use this side as an interface for accurate mechanical positioning, unless the optical form is exactly matched. Because the optical surface is not flat it does not provide a convenient mechanical reference for positioning.

The OAP is oversized by 20 mm, leaving a 10 mm edge that can be used for mounting resulting in a diameter of 170 mm, the required clear aperture is 150 mm. Thus the OAP is oversized by 20 mm,

Constant and sufficient preload force is necessary to maintain a once set orientation of the optic, as the axial retaining strategy keeps the OAP positioned in its local θ_x , θ_y and z orientation and/or location. The sensitivity of Tab. 8 notes, very little perturbation is allowed in the mentioned degrees of freedom.

For exploring axial retaining 4 options are compared and rated on a number of metrics. The strategies below all exert a preload, or another approach of locking, on the reflective face or rear side of the optic.

The concepts in Fig. 9 can be found further specified below. Note that the figures, Fig. 9, are only to represent a group of solutions.

(A) Integrated, flexure based force application

This approach is based on adding flexures integrated in the overall optic retaining structure. Leaving a monolithic design with very few parts. Deflection of the flexures apply the required preload.

(B) Separate mounted spring components

Supplying the preload force using separate components, such as multiple springs. These components are tensioned after the optic is placed. As there is a wide range of components that can individually provide a preload force, options are numerous. Also, the eventual interface that pushes against the reflective surface can easily be chosen.

(C) Wave ring

A wave ring, which on the one side is locked in place using fasteners. The other side interfaces with studs, that in turn interface with the optic applying preload to the optic. This approach has similarities with (B), as the ring is essentially a separate mounted spring, what makes this concept different is that the ring is one added component.

(D) Bonding agent

This approach uses an adhesive to mount the optic. A bonding agent can be added in between the optic and the overall structure. Once cured it locks the optic in place.

Other bonding approaches consist of flexure based bonding, where the bonding pad is placed on a flexure component. More on this approach in the Radial Trade-Off, Fig. 10.

Using adhesive mounting, not only axial direction is set. Also radially the component is fixed in place. Decoupling of radial or axial mounting strategies is often not possible.

When using this strategy, once the optic is mounted it can no longer possible to be removed or replaced.

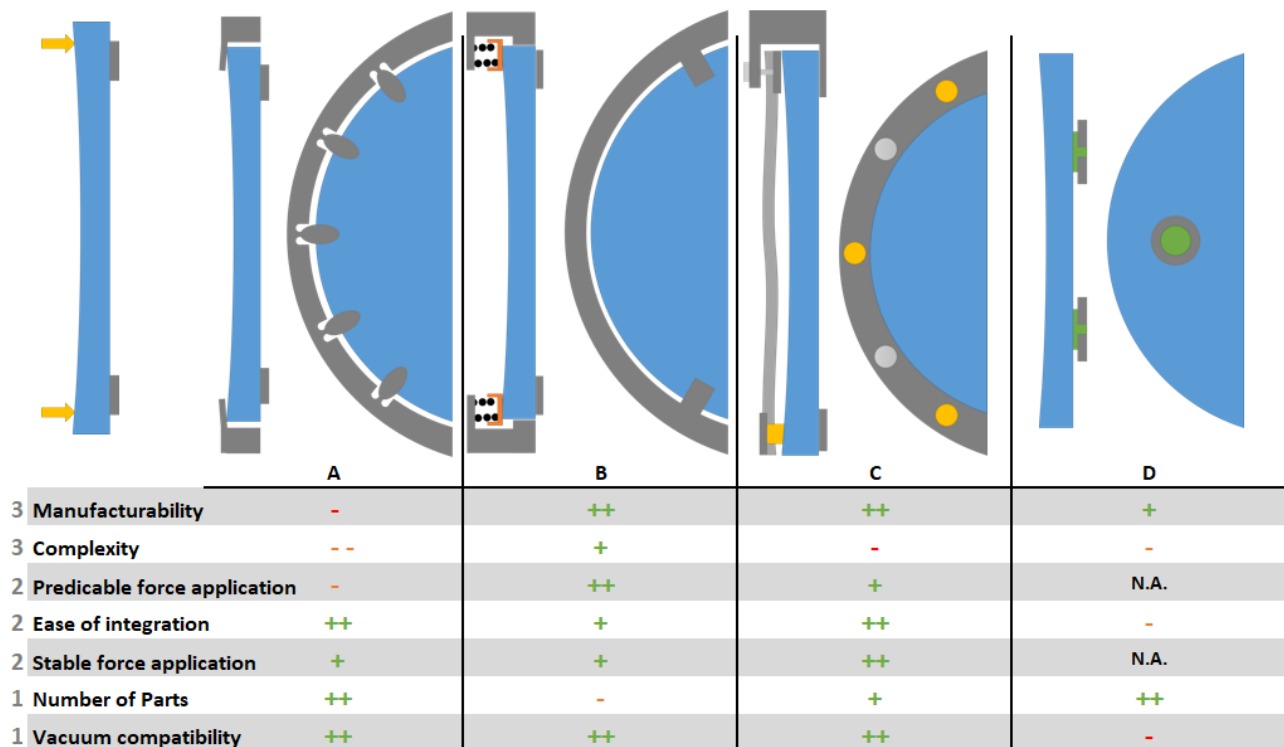


Figure 9: Trade off table of axial holding mechanisms

The concepts are compared using the following metrics.

- **Manufacturability** The ability to manufacture the required components. Preferably based on the facilities at SRON Groningen.

- **Complexity** Complexity is a parameter to estimate the required design effort and analysis necessary to find a viable solution. Complexity is thus an important metric in realization.
- **Predictable force application** Level of predictable application of force with respect to its designed level.
- **Ease of integration** The ease of placing the optical component and applying the retaining mechanism.
- **Stable force application** Stable force application under perturbing conditions such as during the bake-out temperature cycle.
- **Number of parts** Amount of parts necessary to for this mechanism.
- **Vacuum compatibility** How suitable the strategy initially is for use in a vacuum environment.

Weights

The weight of the metrics is based on an estimation of how much the metric contributes to the eventual realization, however, the grading can vary on application.

Manufacturability is very important in realization of structures. If no production methods are available, the design cannot be realized. Very complex designs are not realistic to implement given the amount of effort required to develop and realize. If thorough analysis is necessary other options should be considered. Thus complexity is a very important metric. Therefore, both *manufacturability and complexity* receive a weight parameter of [3].

Predicting the eventual applied force is important as too high preload will cause stresses, while too low preload will not retain the mirror properly. Hard to predict loading generates uncertainty and deters from using and integrating the concept. A concept that integrates well reduces risk in handling and unwantedly damaging the optic. This also applies for the stable force application metric. To realistically retain the piece of optic during perturbations or temperature cycles, a constant stable preload is required. These metrics are important to consider for generating a realistic detailed design. However, the metrics are not considered as important as manufacturability and complexity. Therefore *Predictable force application, ease of integration and stable force application* receive a weight parameter of [2].

The amount of required parts can be considered to be a factor for realization. More parts translates into more detailed design, more manufacturing, added complexity to the assembly, more internal interfaces etc. Resulting in more accurate components (thus more expensive) and lower final accuracy. As such, initial vacuum compatibility translates as well in realistic design, as less analysis has to be done to enable for vacuum implementation. A concept which is by definition suitable for a vacuum application requires less modifications. However, both metrics can be overcome easily, as reducing the number of parts or providing vacuum compatibility can be solved during final design. Thus both *number of parts and vacuum compatibility* receive a weight parameter of [1].

Manufacturability

The flexures of concept (A) are the most difficult to machine conventionally, they require high tolerances and on relative flexible small elements, which hampers the ability to constrain the parts during manufacturing.

Concept approaches (B) and (C), Fig. 9, are considered to be easiest to manufacture. In comparison to the remaining designs, they comprise the least complex geometries and/or dimensions. This eases the manufacturing process of the components using CNC milling or lathing.

Concept (D), requires adding adhesive, which translates in more intricate elements such as channels and pockets which could be can be more difficult to machine. It also inhibits the option to correct and disassemble the mirror in a later stage.

Complexity

Concept approach (B), Fig. 9, is estimated to score well on this metric. To determine the dimensions of the tensioning components, many examples and design solutions exist for concept (B). Here the main point of analysis will be interfacing with the extra force application device. As assembly requires very few parts and little operations. Concept (D) requires effort in determining the optimized bonding parameters as well as analysis for extra tooling that is necessary for correct mounting. Working out optimized dimensions for the flexures of concept (A) is considered to require the most thorough analysis. The force applicator of concept (C) is expected to require more analysis. Especially because little design envelope is available on the reflective surface already

requiring tightly packaged design.

Predictable force application

The solutions of (A) contain separate individual elements which can be often used for applying force. The preload delivered by these elements should be easy to predict with respect to the other concepts. (B) with a wave ring spring is expected to be well predictable, however less so than concept (A). The flexures of concept (A) should be well predictable as well. As flexure design has many use-cases and thorough design guidelines. However, production errors can produce uncertainty and unexpected behavior.

Ease of integration

Concepts (A) and (C) are considered to be the most straightforward to assemble. Thanks to a tensioning devise that is activated after the optic is placed. The concepts have the fewest parts, which makes them easy to assemble. The solution of (B) contains some difficulties as there are more components involved and preload devices might already exert force while mounting. Most intricate to assemble will be concept (D) as the optic has to be positioned correctly, as the optic has to be retained in place while the adhesive is added and cured. However, the bonding agent ensures that not only axially the optic is locked, but also radially.

Stable force application

In comparison with the other concepts (C) is expected to show the most stable mounting force. The large ring component could allow for most deflection and most gradual spring constant. Making sure that perturbations in deflection result in small force deviations. Also, during thermal cycling few components are expected to settle using approach (C). For concept (B), more parts can settle through temperature cycles. Concept (C) is expected to have a very steep spring constant, ensuring that perturbations exhibit large deviations in applied force.

Number of parts

Using the approach (A) is expected to have the fewest number of parts, as using integrated flexures allow for a monolithic design. The use of adhesive in (D) is expected to require very few parts. The concept of using a single spring element in (C) is expected to require more components than (A) and (D) but fewer than (B) as this concept uses more spring elements.

Vacuum compatibility

The concepts of (A), (B) and (C) are expected to be equally suited for a vacuum application, if the materials used allow for vacuum application and the design does not contain trapped gasses and large contact areas between parts. The approach of (D) requires a bonding agent, however most adhesives are generally not suitable for vacuum, thus extra care has to be taken implementing this solution.

Selection

Reviewing the trade-off, the approach of (C) with separate mounted spring components has been chosen. This concept reveals the highest score in Fig. 9.

Radial trade Off

It was decided to separate the radial from the axial retaining. This allows statically determined mounting without cross talk between DoFs. The radial mounting strategy is retaining the OAP in its local x , y and θ_z location and/or orientation. The sensitivities from Tab. 8 show very little movement is allowed in the mentioned degrees of freedom.

As the collimator is only used at a fixed temperature, a well-defined thermal center is not necessary. Locating the OAP in a radially balanced force equilibrium is therefore not necessary. This allows for, the classic V-groove set-up, Fig. 9. This requires one location to supply the preload force and 2 well defined mechanical stops. The xy location is then based on the well defined V-groove end stops. Moreover, the OAP assembly will be characterized before integration in the collimator. The OAP, in this characterization set-up, will have a different orientation than in the collimator. Therefore the direction of gravity will change and a radially balanced location in the characterization set-up will not be representative in the final set-up.

Exploring radial retaining options, 5 main approaches have been selected and rated on a number of metrics. The strategies all exert preload force on the side face of the optic, as shown in the green arrow of Fig. 10. Note that the figures, Fig. 10, are only to represent a group of solutions and not a well-defined singular approach.

The metrics used are the same metrics as mentioned before for the trade-off from Fig. 9.

(A) Extra spring element

This extra element has to be integrated, with the sole purpose of supplying preload force. The spring element can be of any kind and integrated in any way. Much like the conceptual solution group of (B) from Fig. 9.

(B) Monolithic integrated flexure

Integrated in the circumference of the mount, certain types of flexures can be integrated within the structure. The idea of this approach is that, once the optic is placed, the preload is active. The fully monolithic flexure, when dimensioned well, does not require any additional actuation.

(C) Integrated flexure, later actuated

A separate approach with respect to concept (B) is the actuated flexure design, where flexure component delivers the preload force. However, this now is being actuated by another component. The approach still mainly relies on an integrated flexure.

(D) Bonding based

Bonding is often used in combinations with flexures to allow for differences in thermal expansion. Bonding the optic radially does also lock the optic in axial direction, bonding strategies for axial or radial mounting is expected to be coupled.

(E) Off-the-shelf element that supplies force

Adding an customer-off-the-shelf (COTS) component that supplies the preload force. This component can be any plug-and-play component applying preload. The main difference with concept (A) is that the force supplying part is an integrated subassembly, allowing easy to work with interfaces and integration.

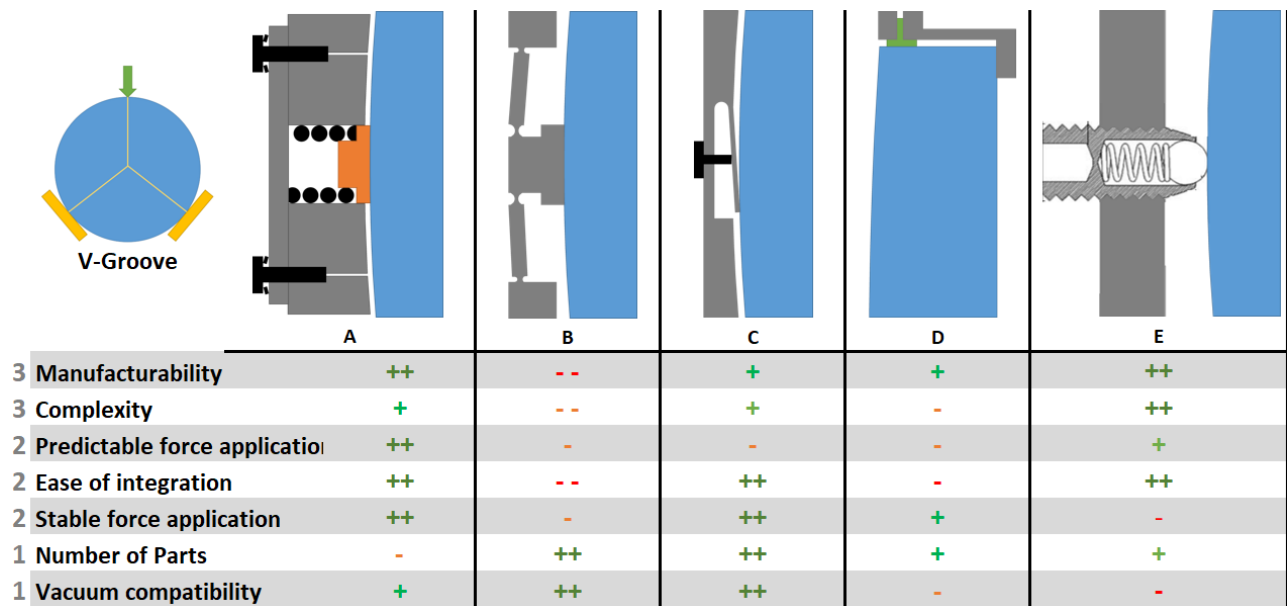


Figure 10: Trade off table of radial holding mechanisms

Manufacturability

The concepts of (A) and (E) are considered easiest to manufacture. Concept (A) is well manufacturable due to it consisting of multiple components, allowing for design freedom in IF's and manufacturability of subparts. The approach of (E) is good because only IF to COTS have to be made. Both concepts (C) and (D) are similar as (C) has no complex flexures and actuation is added later. Approach (D) requires a simple flexure design, but includes intricate machining for the adhesive bonding slots. Concept (B) most likely requires a complex flexure design which is hard to manufacture.

Complexity

Concept (E) is the least complex, as it consists of only COTS components, with manufacturer specifications

provided. Concept (A) is relatively simple in design, with a force application device that is used for this purpose only, therefore idea to work-out the optical parameters. Concept (C) is expected to contain relative simple flexure design, as well as concept (D), however approach (D) requires some extra thought in implementation using a bonding agent. The concept of (B) contains the most complex flexures and requires thorough analysis to get this design approach working.

Predictable force application

Using a single force application element, concept (A) is expected to have the best force predictability. The COTS solution of approach (E) is expected to be well characterized by its manufacturer and usable with a look-up table. However, the exact dynamics of what happens in the COTS component may remain unclear, thus somewhat less predictable as conceptual solution (A). Flexure based designs are well studied and have many design guidelines usable to calculate what force can be expected. However, to predict what happens exactly in somewhat less straightforward flexures and boundary conditions, as found in (B), (C) and (D), exact force application requires analysis to predict.

Ease of integration

For assembly, concepts (A), (C) and (E) score equally well. As the preload force in these three conceptual approaches can be added after the optic has been placed. For the bonding approach of (D), integration is expected to be more difficult. Extra tooling is required to position the optic and a strategy has to be designed to apply the bonding. Therefore concept (B) should be most difficult to implement.

Stable force application

During perturbations or temperature cycles, it can be expected that approaches (A) and (C) exhibit the most stable force application behavior. Due to its longer range, thus shallower spring constant. Depending on the flexure design of concept (D), this can be considered slightly worse than for concepts (A) and (C). As the approach from approach (B) is expected to be very stiff, small perturbations result in large preload deviations. For concept (E) the COTS component is hard to predict stability through perturbations and therefore difficult to implement.

Number of parts

The approach of (A) requires the most parts, whereas approach (B) proposes to utilize a monolithic design with very few parts needed. This applies for concept (C) as well, where part count is only to be increased by a fastener. The approaches (D) and (E) require few components as well, however more expected to concepts (B) and (C).

Vacuum compatibility

Concepts of (B) and (C) can be considered to be well suited for vacuum application by definition. Approach (A) is expected to function well in a vacuum application, however design effort has to be implemented. The concept using COTS components in (E) can be considered least suitable or even not allowed if vacuum capabilities is not specified. If specified, this will yield no problem.

Selection

Concept (A) has been selected as the radial preload application mechanism. Concept group (A) and (C) do have equal rating in Fig. 10. While concept (C) is the more elegant solution, with significantly fewer parts. But as explained, the added complexity in requires thorough analysis. Looking at the overall design of the collimator, where a number of mountings, interfaces, analyses and other work has to be done a less complex radial mounting design of this optic will be more time efficient and robust.

Reference flat

As explained in Sec. 3.1.2, the optical axis of the OAP cannot be directly measured, thus requires an extra measurable reference component. Such a reference flat is able to store line of sight(LoS) information and can be reached by a theodolite during alignment, further explained in 4.2 and [AD1]. The reference flat is to be positioned stable with respect to the OAP.

This translates in that only θ_x and θ_y of the reference flat's orientations are crucial. Other degrees of freedom do not have to be maintained with a high degree of stability or positional accuracy. Therefore only axial mounting

is considered in the trade off.

The reflective side of the reference flat is a polished surface. This side, thus very flat, can be used for a well defined mechanical interface. Leaving the rear of the optic available for mounting strategies. Therefore, it is chosen to constrain the reference flat on the optical surface.

With respect to the trade off table of Fig. 9. The concept of (C) receives a different score for complexity, here it will no be regarded as a ++. As previously complexity was expected to be added due to very limited design envelope to implement this strategy. For this application this is not maintained.

The metric **Ease of integration** receives more weight. As the entire package is most likely to be a lot smaller which hampers proper integration.

For small optics, relative small pretension rings can be used. Off-the-shelve "wave washers" are be well suited for this application. Therefore concept-group (C) has been chosen.

Mounting Fold Flat

The fold flat (FF) assembly has to position and retain the FF itself and allow for correcting for orientation and axial positioning the FF. These two functions can be separated. Firstly the FF is retained in structure. Secondly the mounted FF can then be adjusted. Fig. 11 shows the fold flat in its retaining structure and, in black, the adjustable motion.

Specifications of the FF can be found in Tab. 11 and in App. A.1.3.

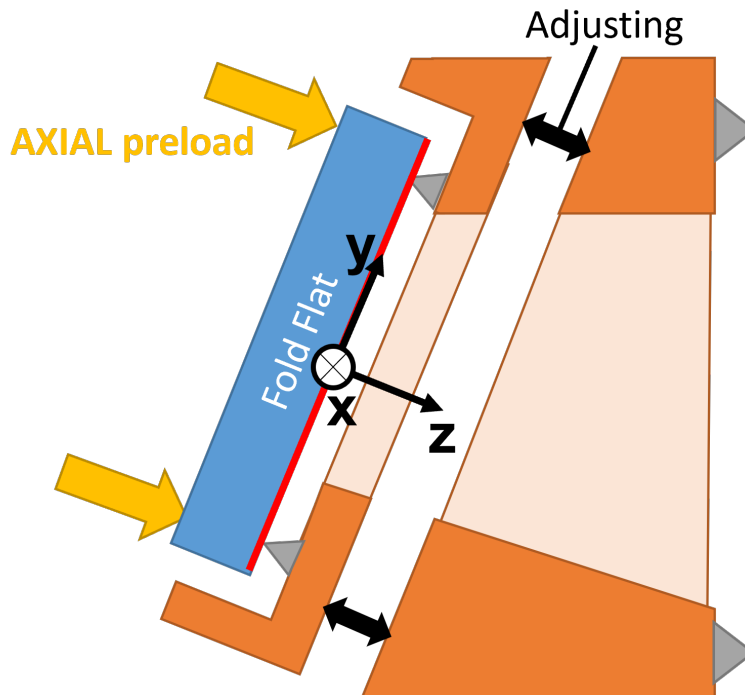


Figure 11: Schematic representation of the FF subsystem. The reflective side of the optic is marked in red.
Diameter optic: $D_{FF} = 101.6$ mm.

Finding a mounting solution to retain the FF allows for a different strategy than the OAP. The reflective surface is flat and can be utilized as an accurate mechanical positioning surface, allowing for a mechanical interface to define the position of the flat. This also allows for the rear to be available to receive the axial retaining force.

The FF is insensitive in its local x , y and θ_z location and/or orientation as long as the full beam will always reach the mirror surface, Tab. 8. The radial retaining therefor is not considered crucial. The flat is sensitive in its local θ_x , θ_y and z orientation and/or location, once positioned these degrees of freedom have to remain stable.

Off-the-shelf solutions for mounting flats exist. However, few COTS solutions are available for this application that ensure stable mounting of such large flats, and adhere to the environmental vacuum requirements, Sec. 2.

Therefore in-house manufacturing has been chosen.

Axial trade off

A similar trade off can be made for axial mounting of the FF as with axial mounting of the OAP. Therefore, the same Fig. 9 is in effect and, with some alterations, can be used.

Previously complexity rating in Sec. 9 was based on the expected complexity due to the limited design envelope to implement the approach of (C). For this application this is not true, as the rear of the optic is available for preload structure and no volume has to be excluded to maintain a clear aperture. Therefore the trade off table of Fig. 9 has been adjusted. The concept of (C) receives a different score for complexity, here it will no be regarded as a "++".

Selection

Using Fig. 9 the optimum solution appears to be conceptual approach (B). However, with the different rating on complexity of concept (C), this approach now receives the best grading with used metrics and weights.

Adjustability

The sensitivity Tab. 8 reveals harsh positional requirements on the fold flat's θ_x , θ_y and z . In Sec. 2.2.2, alignment is said to be required for this optical component. In Fig. 11 volume for the alignment option is denoted with black arrows. For a given solution there are multiple existing mechanisms available.

Off-the-shelf options, for certain large mirrors are often not vacuum compatible or suitable for cleanroom applications. [1] [5] [18]

The iterative nature of aligning the fold flat (more in Sec. 4.2) makes that orientation of the adjusters is not important.

Pinhole stage

The pinhole subsystem has to present a well-defined interfacing surface for the pinhole. The pinhole defines the Object Focal Plane (OFP). The sensitivity specified in Tab. 8 shows that the pinhole location is sensitive in x , y and z translation and needs to be aligned in these DoF's, Sec. 4.2. While, the pinhole orientation in the rotational DoFs are insensitive for perturbations.

Following the optical path, the pinhole is located in the focus of the OAP. It is chosen to fix the OAP and move the pinhole, in x , y and z translation, to the optimum position with respect to the OAP. In many xyz -stage solutions the planar xy -motion is decoupled from its orthogonal z motion.

XY motion

Commonly mechanism for providing x and y motion is a stacked linear guide. In Fig. 12a an example of a stacked linear guide can be seen, where body (1) exhibits xy degrees of freedom with intermediate body (2) with only 1 DoF. Such linear guides can be constructed with hole hinges, (reinforced) leaf flexure or many other options. Other options consist of 3 folded leaf springs, as shown in Fig. 12b. This approach does allow for rotation in θ_z . But most optical elements, and the pinhole as well, are insensitive in θ_z .

Other solutions, such as: loosen-reposition-tighten or shimming come to mind as well. These are often used mechanisms for stable, set-and-forget, alignment.

COTS xy -stages are readily available, easy to implement and proven designs, e.g. Thorlabs' solution, Fig. 13. Which is a clean and vacuum environmental compatible stage, utilizing the stacked linear guide set-up. Note that for such a particular system, the mounting options are often based on other COTS components which results in loss of freedom to choose interfacing solutions. Moreover, using a COTS component material choice is lost, which has implications on thermal expansion differences. [1] [4] [18]

Concluding, the benefits of COTS components outweigh the previous mentioned drawbacks. Therefore the COTS components were used, App. A.3.1. [1]

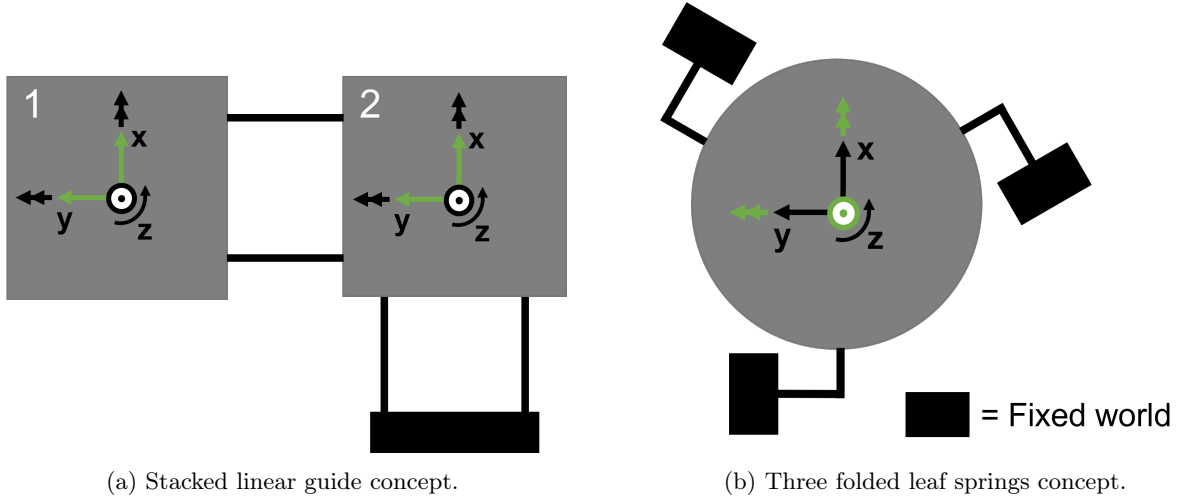


Figure 12: Two approaches of xy DoF behaviour.



Figure 13: Vacuum compatible Thorlabs xy -stage. [1]

Z motion

To apply the single degree of freedom z -motion for the pinhole bears a wide range of solutions. Exploring linear guidance options, 5 main direction of approaches have been selected.

An estimation of the required range in z -direction has been made a worst case z -direction uncertainty of each subassembly has been approached in Eq. 1. The OAP and fold flat are reflective, thus uncertainties of the OAP, fold flat and collimator structure in z -direction are doubled. Totalling to a worst case 0.9 mm required two sided range, as found in Eq. 1.

$$Total \ uncertainty = 2FF_{Assy} + 2OAP_{Assy} + 2Collimator_{Assy} + PP_{Assy} = 0.9 \text{ mm} \quad (1)$$

Fold flat assembly:	$\delta FF_{Assy} = 0.1 \text{ mm}$
OAP assembly:	$\delta OAP_{Assy} = 0.1 \text{ mm}$
Collimator assembly:	$\delta Collimator_{Assy} = 0.2 \text{ mm}$
Pinhole assembly:	$\delta PP_{Assy} = 0.2 \text{ mm}$

(A) Flexure based linear stage

Using two flexures to form a linear stage is a very often used approach. The leaf flexures can be executed in multiple designs such as a reinforced leaf or hole hinged flexure.

(B) Rotating hinge

A single rotating hinge does not directly form a linear stage. However, an arbitrary point with an offset of the

hinge experiences one degree of freedom, however moving over an arched trajectory, thus resulting in additional secondary parasitic translation and rotational motion. The combination of a large offset hinge-point and small rotations follow the cosine effect and can be approximated to be linear of a small range of motion.

(C) Three struts

Using the kinematic constraint of three struts that connect to the stage each tangential to a same circle, constrain 3 DoFs, in Fig. 14 local x , y and θ_z are constraint. The z direction is to be moved, as well as the θ_x and θ_y . However, for the pinhole plate, these DoFs are not sensitive for perturbations, Tab. 8.

(D) Shimming

Concept (D) proposes to use shimming as an alignment mechanism. Adjusting the pinhole z location by placing, removing or re-manufacturing spacers in between the stage and the fixed world.

(E) Loosen, reposition and fasten

A simple approach for alignment can be to loosen the component, reposition the component and lock again. Without guidance or actuators. Repositioning would be achieved by hand, iteratively until set correctly.

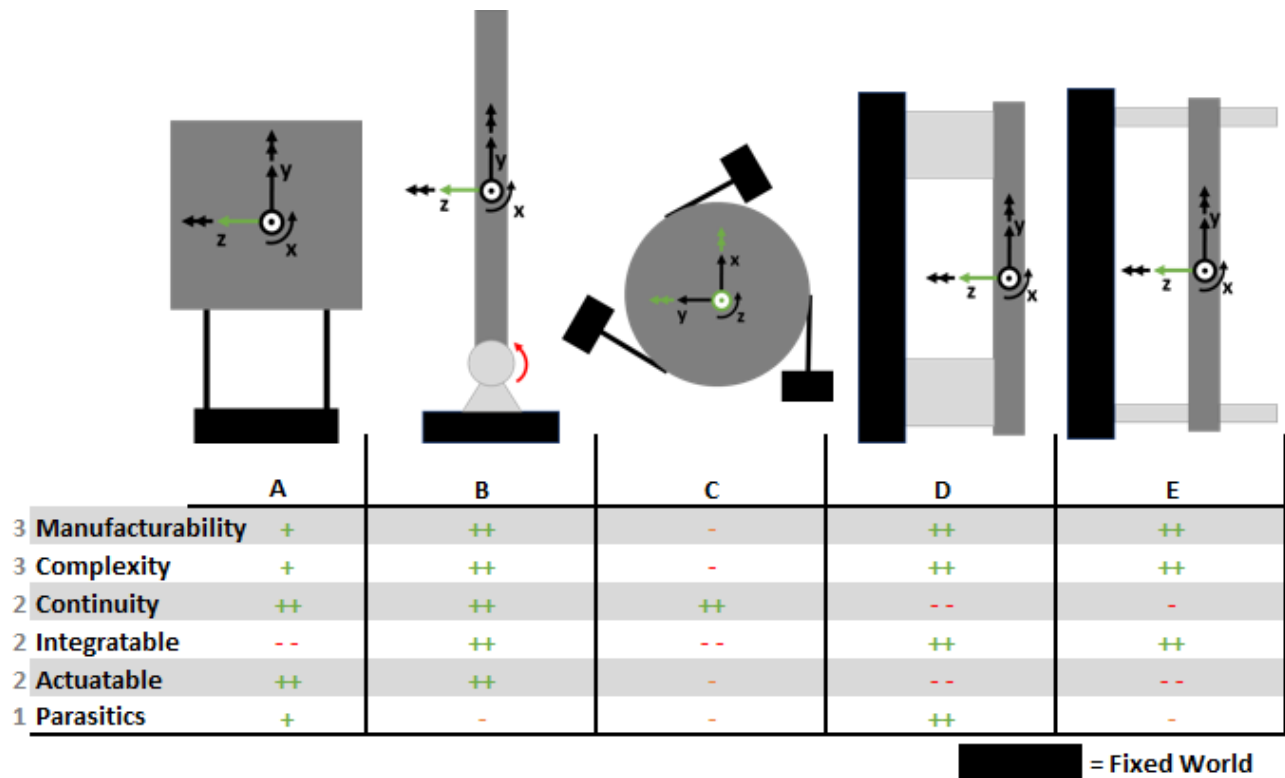


Figure 14: Z-motion trade off.

The weight of the metrics is based on an estimation of how much the metric contribute to the eventual realization. The grading can vary on application. The concepts are compared using the following metrics:

- **Manufacturability** The ability to manufacture the required components. Based on the facilities at SRON Groningen.
- **Complexity** Amount of thorough analysis necessary to implement this strategy.
- **Continuity** Ability for continuous motion guidance.
- **Actuable** Possibility to actuate the motion
- **Integratability** Ease of integrating this strategy with existing structure.
- **Parasitics** Presence of parasitic motion.

Weights

The weight of the metrics is based on an estimation of how much the metric contributes to the eventual realization. The grading can vary on application.

Manufacturability is very important in realization. Complex designs are not realistic to implement given the amount of effort it takes to develop and realize, thus a very important metric. Therefore, both *manufacturability* and *complexity* receive a weight parameter of [3].

Continuous motion and availability to be actuated greatly increase success of alignment, thus also the success of realizing the required performance. The z motion stage is only part of the pinhole alignment assembly. Being able to inherently successfully integrate with the other assembly components without too much modifications increase potential realistic detailed design. Therefore, *Continuity*, *Actuable* and *integratability* receive a weight parameter of [2].

The parasitics metric does add complexity during the alignment stage. However, as the alignment is often iterative, any parasitics can be adjusted for quite easily. Thus *parasitics* receives a weight parameter of [1].

Manufacturability

The concepts of (B), (D) and (E) are expected to be well machinable using conventional machining. As a hinge element of approach (B) can be designed to be well manufacturable. Concept (D) requires machinable parts that are well suited for adjusting to a new dimension or for manufacturing at high tolerances. Concept (E) opts for a conventional locking mechanism which is expected to be easily manufacturable. Approach (A) can be considered to require more attention, as the leaf springs are often thin and flexible. The concept of (C) incorporates thin elements as struts, to achieve the degrees of freedom that characterizes a strut. Thin elements however, are difficult to machine using conventional CNC or lathe.

Complexity

The amount of analysis required for the design to be realized for the concepts of (B), (D) and (E) is minimal. For a single hinge element many design cases and design guidelines exist. For a spacer element, no movement and flexing in parts is required. Concept (E) only requires a locking mechanism. Approach (A) is expected to require more analysis. A linear guide using two flexures is widely used and clear design guidelines exist, however this approach still needs more analysis than (B), (D) and (E). Concept (C) is expected to require most attention to optimize to a realizable design.

Continuity

From approaches (A), (B) and (C) it is very clear that a continuous motion is supported. Whereas from concept (D) this most certainly is not, requiring remounting each time an adjustment is introduced. For concept (E) some continuity can be expected during the repositioning stage. However this is not over a guided motion path and can or will be effected by stick/slip behavior.

Integratability

To combine the z motion stage with the xy motion component, the concepts of (B), (D) and (E) can be expected to be very suitable. Allowing easy interfacing surfaces or mounting options. Approach (C) is expected to leave a small volume envelope for the xy -stage. Approach (A) requires a large volume envelope in the direction of motion, which is expected to be not available.

Actuatability

The concepts of (A) and (B) should be relatively easy to actuate, requiring one adjustment element to supply the motion. Due to the multiple degrees of freedom of concept (C), multiple locations are required to supply a representative amount of motion. Concepts (D) and (E) cannot be actuated.

Parasitics

Concept (D) can contain no parasitic movement when the shimming process is designed and executed well. Approach (A) inherently contains a small amount of movement in local x when moved over in z direction. The same yields for concept (B), which introduces a rotation in θ_z as well. Due to the loosely constraining of concept (C), parasitic movement in θ_y , θ_x and θ_z can be expected, however these are insensitive to focal spot positioning. The concept of (E) is expected to contain parasitic motion, as no guidance path is well define, only loosely on the pole sliding fit.

Selection

From Fig. 14, the conceptgroup of (B) received the best rating, using the given metrics overall, and concept has therefore been chosen to be developed further. However, concept (E) has the option of being used as well. To add the required initial positional offset between the collimator structure and the pinhole, components have to be added. Integrating the adjustability proposed by concept (E) into the structure a rough z positioning can be achieved. Extra z range can prove to be very useful during the assembly and/or alignment phas(es).

3.2 Detailed Design

An overview of all the manufactured and/or procured components can be found in App. A.2.

3.2.1 OAP Assembly

Retaining the OAP the following design (Fig. 15) has been designed, manufactured and integrated.

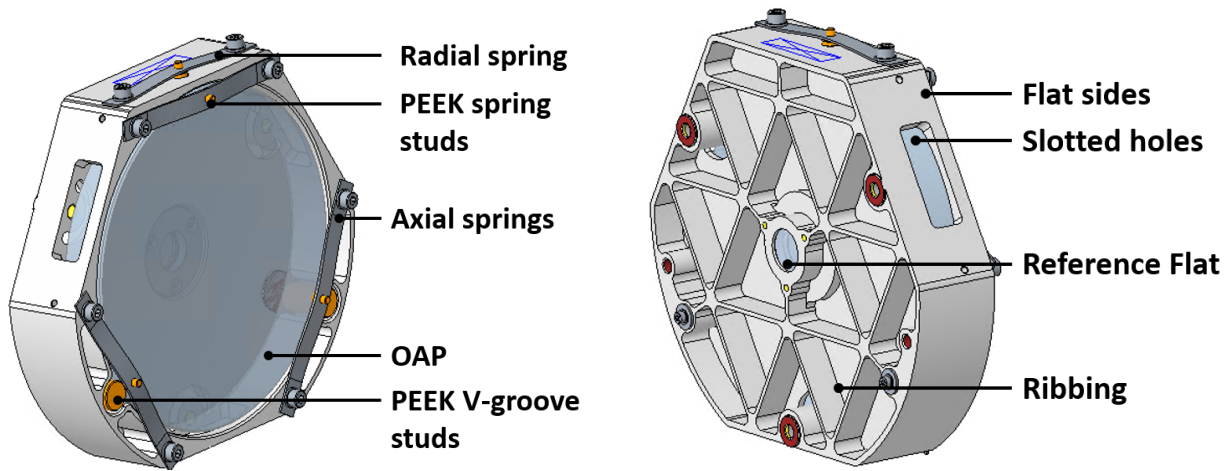


Figure 15: Overview of OAP assembly. Diameter optic, $D_{OAP} = 170$ mm

Mounting

The side and rear of the OAP are used as mechanical surfaces to define the OAP's position. The rear of the optic is axially supported by 3 mounting pads, constraining the OAP in z , θ_x and θ_y in the optic's local coordinate system as seen in Fig. 8. For positioning the translational DoFs, x and y , the side of the OAP is used.

As the collimator is operated at a fixed temperature, a well-defined thermal center (in local xy) is not necessary. Locating the OAP in a radially balanced force equilibrium is therefore not required. This allows for, the classic V-groove set-up, Fig. 9. This requires one location to supply the preload force and 2 well defined mechanical stops. The x and y location is then based on the well defined V-groove end stops, which are constructed of the material PEEK, App. A.3. These PEEK stops do not damage the optic due to a relative low Young's Modules, in comparison with metals, however the material is still suitable in the vacuum environment.

Rotation in θ_y is fixed constraint by friction generated by mounting preload force.

Leaf Springs

To mount the off-axis parabolic mirror in axial direction, 3 leaf springs are used. These double-sided bolted leaf springs supply the retaining force in axial direction. The the preload force is applied perpendicular to the surface and located directly opposite from the 3 mounting pads, leaving only compression stresses in the optic. Another separate leaf spring is used to supply the preload force in radial direction. PEEK studs translate the force from the springs onto the mirror, ensuring minimal hazard damaging the reflective surface.

Structure

The overall structure of the mount envelops the OAP's non-reflective surfaces.

To shaving off unnecessary material, thus mass, while leaving most of the structure's stiffness intact, ribs have been made in the mount's back side. Unnecessary mass would eventually leave the collimator hard to handle. Following the 1:6 to 1:8 rule of thumb, the distance between the ribs and the thickness of remaining base material is connected.

For integration of the optical component in its mount, holes have been added in the mount's side. This will enable guidance of the optic while placing the OAP on its pads. As well as rough positioning.

For storing, handling and servicing the OAP assembly, flat sides have been added. These ensure that the assembly can rest on its side. The flat sides also remove unnecessary material.

To mount the OAP mount structure to the collimator structure, 3 threaded inserts are placed and mounting pads are implemented in the OAP mount. The OAP's off-axis wedge angle is introduced in the collimator structure.

Reference Flat

For the reference mirror, a *Thorlabs* 1" (25.4 mm) flat has been procured. In Sec. 3.1.3 a wave washer approach of mounting has been selected for this application. Fig. 16 shows a CAD representation of the reference flat mounting. The reflective side of the reference flat is used as interface for accurate positioning. The wave washer applies the preload onto the reference flat's rear surface, here the optic is protected from the washer using a PEEK ring. The wave washer from manufacturer Amatec exerts 37.9 N of force when fully compressed, more can be found about the wave washer in App:A.3.1. The force exerted by the wave washer is orthogonal to the rear surface of the flat and opposite the mechanical stop, ensuring only compression stresses in the optic. Finally a retaining cap holds the components in place. [1] [3].

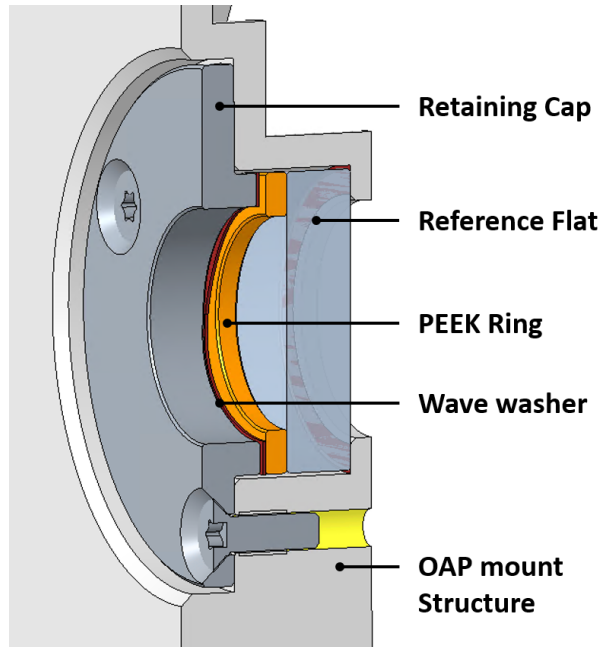


Figure 16: OAP Reference flat with 3 wave washer. Optic diameter $D_{ref} = 25.4$ mm

Dimensioning

Leaf Springs

As a rule of thumb, a force is applied resembling 5 times the OAP's gravitational pull. The material density and dimensions of the OAP can be found in Tab. 10 and App. A.1.2. Using Eqs. 2 and 3 we find "5G" to be equal to $F_{5G} = 65.4$ N.

The length (L) of the spring elements are based on mirror and OAP mount geometry. Material thickness is based on readily available material and spring width (w) is kept equal for the axial and radial springs if possible. The readily available material used for construction of the leaf springs is 1 mm thick AISI316 stainless steel, App. A.3. Used dimensional parameters of the springs can be found below. All the while iterating to the "5G" goal and not to exceed the materials yield criteria. The deflection has been the main tunable parameter.

The proposed deflections(u). For the axial preload(u_{ax}), using Eqs. 4 and 5) a force application with 3 springs results in $F_{ax} = 63.5$ N. This resembles the "5G" goal. Other spring parameters can be found below.

The same yields for the radial spring.. Using proposed deflection of u_{rad} for the radial springs and Eqs. 4 and

5 a force application of $F_{rad} = 75.4 \text{ N}$. Which is slightly more than the proposed "5G".

Maximum stress in the material is calculated using Eq. 6. Resulting for the axial spring in 2.86 MPa and for the radial spring in 2.89 MPa, which is below yielding of the material.

Specifications of the materials used can be found in the App. A.3 [19] [20]

$$M_{OAP} = \rho_{OAP} V_{OAP} = \rho_{OAP} \frac{1}{4} \pi D_{OAP}^2 t_{OAP} = 1.33 \text{ kg} \quad (2)$$

$$F_{5G} = 5g M_{OAP} = 65.4 \text{ N} \quad (3)$$

$$I_{xx} = \frac{1}{12} w h^3 \quad (4)$$

$$F_{spring} = \frac{96u E_{316} I_{xx}}{L^3}, \quad 3 * F_{ax} = 63.5 \text{ N}, \quad F_{rad} = 75.4 \text{ N} \quad (5)$$

$$|\sigma_{Max}| = \frac{|F_{spring}| L u}{4 I_{xx}}, \quad |\sigma_{rad}| = 2.86 \text{ MPa}, \quad |\sigma_{ax}| = 2.89 \text{ MPa} \quad (6)$$

$$D_{OAP} = 170 \text{ mm}, \quad t_{OAP} = 23 \text{ mm}, \quad \rho_{OAP} = 2550 \text{ kgm}^{-3}, \quad g = 9.81 \text{ ms}^{-2}$$

$$L_{ax} = 90 \text{ mm}, \quad w_{ax} = 10 \text{ mm}, \quad u_{ax} = 1.0 \text{ mm}$$

$$L_{rad} = 85 \text{ mm}, \quad w_{rad} = 10 \text{ mm}, \quad u_{rad} = 3.0 \text{ mm}$$

The used Eq. 5 holds for leaf springs that are free to shorten, being constraint parallel but can move translational. Calculating the parasitic motion of the end of the leaf springs, the Eq.7 is used. Resulting in parasitic motion for the axial springs of $u_{para}^{ax} = 6.7 \mu\text{m}$ and $u_{para}^{rad} = 64 \mu\text{m}$ for the radial leaf spring. For this purpose, the mounting holes of the leaf springs are oversized, which translates in 5.5 mm diameter holes. Ensuring 0.5 mm play with the M5 bolts that used for mounting. Which proves free motion is available, and Eq. 5 is usable. [19] [20]

$$u^{para} = \frac{3}{5} \frac{u^2}{L}, \quad u_{ax}^{para} = 6.7 \mu\text{m}, \quad u_{rad}^{para} = 64 \mu\text{m} \quad (7)$$

3.2.2 Fold Flat Assembly

Mounting the fold flat (FF), the following structure, as seen in Fig. 17a has been designed, manufactured and integrated.

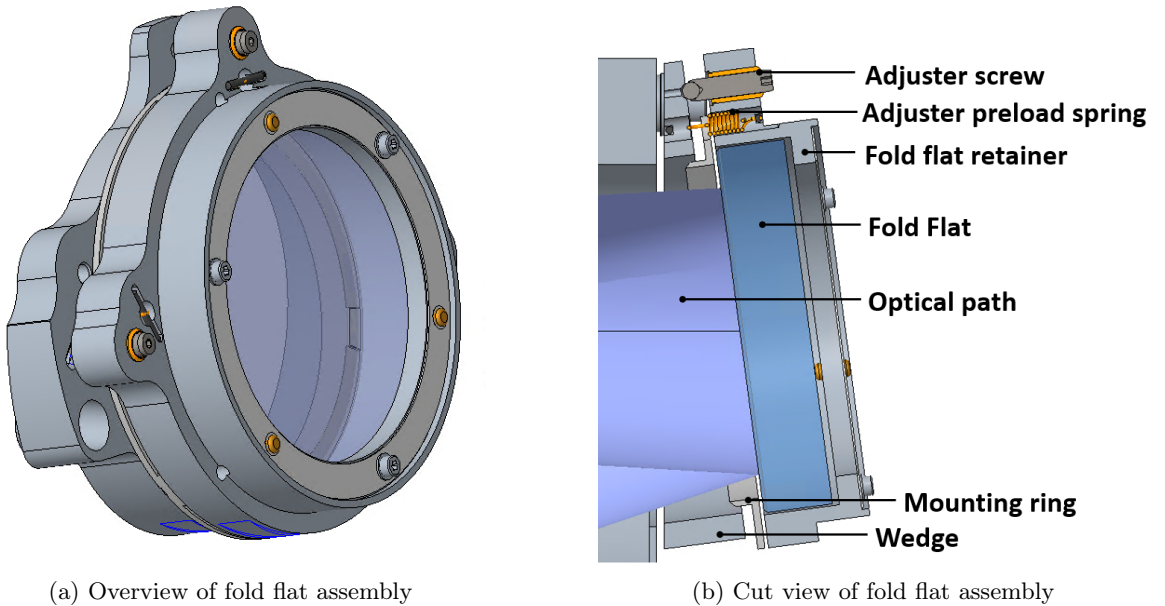


Figure 17: Fold flat (FF) assembly. Diameter optic, $D_{FF} = 101.6 \text{ mm}$

Mounting

As mentioned in Secs.2.2.1 and 3.1.3, the sensitive DoFs of the FF are θ_x , θ_y and z in its local coordinate system, as seen in Fig. 11. For mechanical positioning, a three point mounting pad interfaces with the FF's reflective surface, constraining the optic in θ_x , θ_y and z . Other DoFs are not accurately positioned.

In Sec. 3.1.3 a wave ring approach to supply the preload force for mounting has been selected. This ring is constrained onto the fold flat retainer at 3 locations using fasteners. The preload is by generating 3 deflection waves in the ring. The produces preload is transferred to the optic using PEEK studs. In Figs.33 the preload ring can be seen in undeflected state.

Structure

The FF is placed in a retainer, this structure contains the components to mount and retain the optic. The open back design of the FF retainer allows for LoS measurements, Sec. 3.1.2. This is useful for stability measurements and post bake-out checks, Sec. 4.2. Moreover, this opening allows for easy assembly of the optic in its mount. This can further be seen in Sec. 4.

The FF resides against 3 mounting point pads as a well defined mechanical interface. These pads, are part of a separate ring, Fig. 18. This ring is mounted after the optic is placed, further explained in Sec. 4, and includes a short baffle for stray light reduction.

To introduce the required angle of the FF with respect to the collimator structure, a separate wedge component is designed. This wedge is mounted onto the collimator.

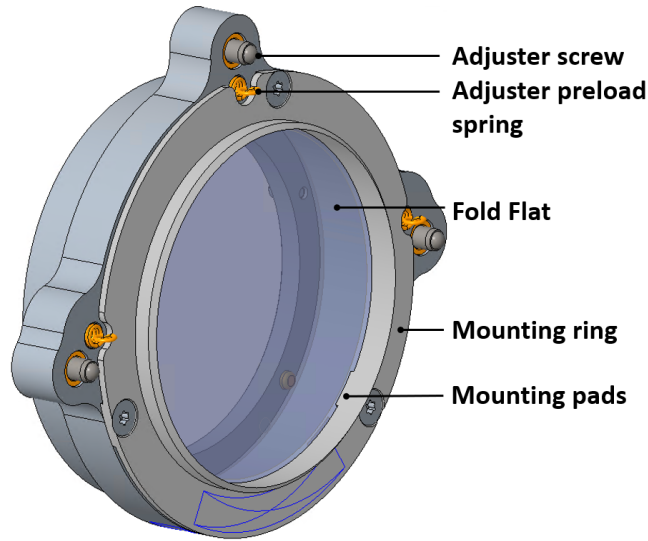


Figure 18: Locking ring holding the fold flat in place.

Adjustment

Adjusting the fold flat's local θ_x and θ_y a very often used solution has been implemented. Where the optic retaining structure is repositioned as a whole. As seen in numerous COTS applications.[1] [5] [18] [21]

Using 3 adjustment push screws, with a ball head, supplying the tunable offsets. A preload force ensures continuous contact of the adjustment screws with a mechanical stop, found in the wedge component. 3 adjustment screws, residing in a cone, groove, flat configuration, have the ability to adjust for θ_x and θ_y . The cone, groove, flat configuration (Kelvin kinematic coupling) ensures a well-defined kinematic positioning. Which results in high repositionability. [22]

Due to the use of 3 adjustment screws, seen in Fig. 17a, parasitic movement in the flat's z direction is introduced.

The *Thorlabs* 0.25 fine thread M6 adjustment screws and bushing counter part (App. A.3.1), given a realistic 5° resolution by hand, realize an expected $5.7arcsec$ resolution in θ_x and θ_y of the fold flat.

Dimensioning

Wave Ring

The mass of mirror is calculated using Eq. 8. and the FF dimensions found in Sec. 3.1.2. A "5G" rule of thumb, Eq. 9 results in 19.4 N. The ring's material is AISI316 stainless steel, App. A.3. To find suitable wave ring dimensions, COMSOL Multiphysics 5.6 has been used. A parametric sweep, Fig. 19, revealed suitable dimensional parameters. The sweeping parameters ring thickness t_{ring} and ring width (w_{ring}) have been swept while outer diameter (D_o) had been set and looking for a "4G" preload force. Found parameters can be seen below.

Using these specifications, maximum deflection reaches $u_{ring} = 2.0$ mm. The force will be applied onto the optic by PEEK studs which protrude the deflection distance (u_{ring}) from the holes they reside in, as such the required displacement can be accurately determined using the machined PEEK studs.

$$M_{FF} = \rho_{FF} V_{FF} = \rho_{FF} \frac{1}{4} \pi * D_{FF}^2 t_{FF} = 0.39 \text{ kg} \quad (8)$$

$$FF_{4G} = 5g M_{FF} = 15.6 \text{ N} \quad (9)$$

$$D_{FF} = 101.6 \text{ mm}, t_{FF} = 19.10 \text{ mm}, \rho_{Zerodur} = 2550 \text{ kgm}^{-3}$$

$$D_o = 105.8 \text{ mm}, t_{ring} = 0.5 \text{ mm}, w_{ring} = 9 \text{ mm}$$

$$u_{ring} = 2.0 \text{ mm}$$

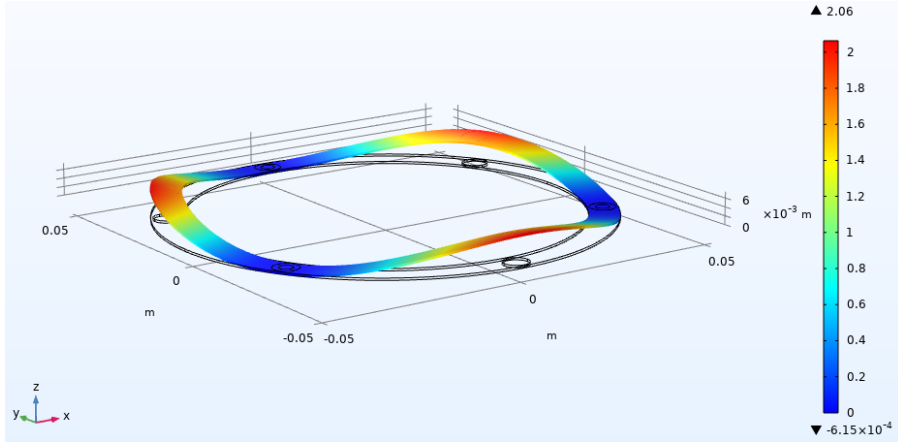


Figure 19: Results of a parametric sweep, using COMSOL Multiphysics 5.6.

Adjuster Preload

The preload force for the adjustment mechanism has been approached by a rule of thumb to required "10G". A rigid connection is required between the adjusted body and the wedge, which is mounted onto the collimator. Especially during the alignment procedure, Sec. 4.2, when the FF adjusters are used. High repositioning accuracy is required and the surface friction of the cone and groove of the Kelvin mount have to be overcome. Moreover, the FF assembly can be bumped into, as it is mounted on the outside of the collimator structure. The designed structure allows for such "10G" rule of thumb, as from the design of the FF assembly, negligible deformation can be expected that jeopardizes the FF's optical performance due to the adjuster preload.

The mass of the movable components has been estimated to be a total of $M_{FF}^{tot} = 0.70$ kg, this estimation includes the FF optic and the rest of the moveable FF retainer. Using Eq. 10 we find an estimate of the total required "10G" preload force. Thus, over 3 springs an estimate of 22.9 N remains per spring. The tension springs from the manufacturer *Amatec* which have been chosen, App. A.3.1, exert a force of 27 N at their loaded length. [1] [3]

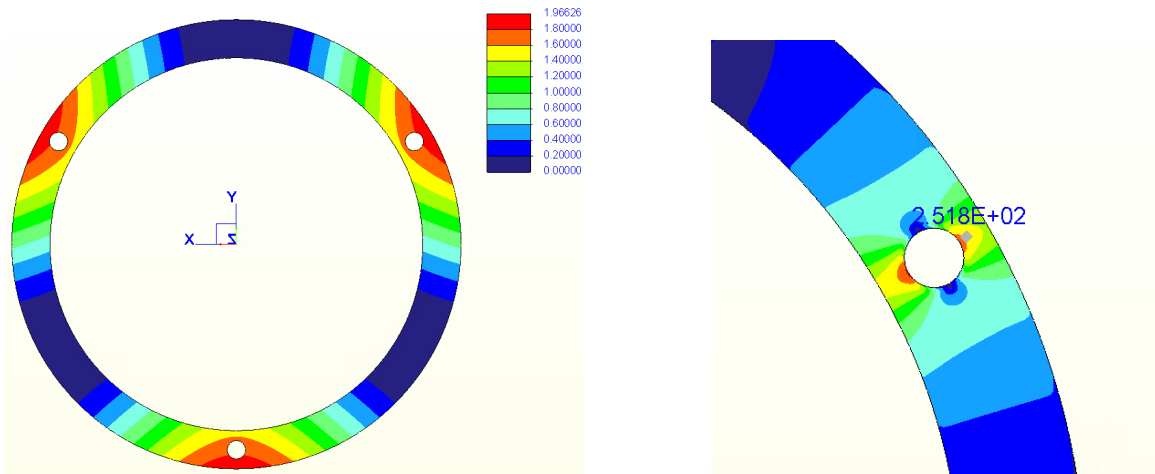
$$F_{FF,10G} = 10g M_{FF}^{tot} = 69 \text{ N} \quad (10)$$

$$F_{FF, Spring} = \frac{1}{3} F_{10G} = 22.9 \text{ N} \quad (11)$$

The COMSOL Multiphysics 5.6 package has been used to find suitable dimensional parameters. With the PTC CREO Parametric 4.0 simulate toolbox and the parameters from Sec. 3.2.2, the results have been recreated and verified. For the FEA method, a maximal mesh element size of half the ring's thickness have been created. Which results in a maximum element size of 0.25 mm

Using the CREO package for chosen ring parameters. Similar values have been obtained. A 19.4 N force as input parameter generates ~ 1.97 mm maximum displacement, Fig. 20a.

Unrealistic stress concentrations due to the simulated boundary conditions and mesh options for such a thin ring limit a thorough analysis on maximum stress. An estimation has been made for a maximum stress concentration of 2.51 MPa, concentrated near the ring's mounting holes, Fig. 20b. Which is below the materials maximum yield, App. A.3.



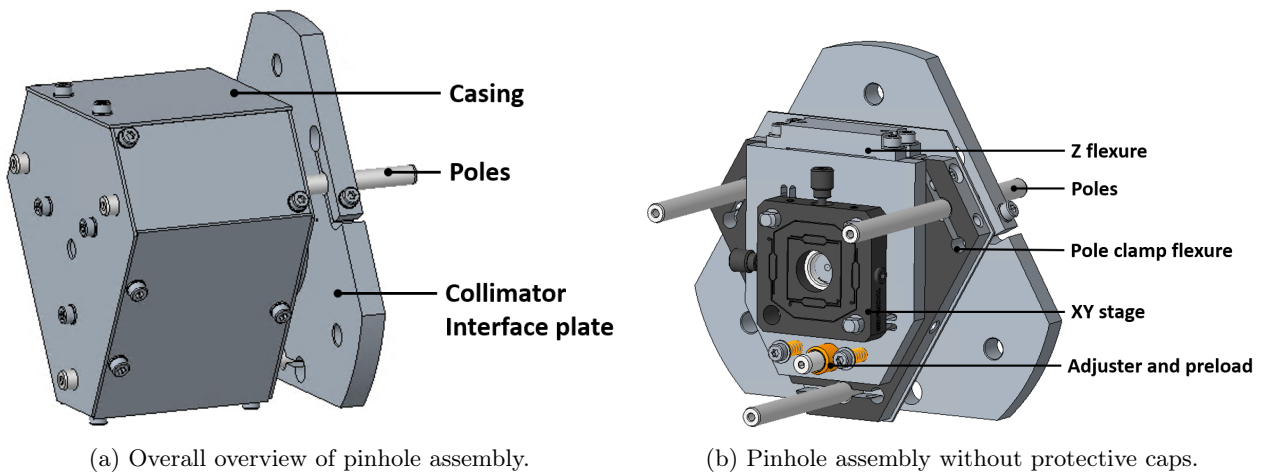
(a) Fold flat ring deflection using CREO parametric. Units in [mm]

(b) Ring stress concentration. Units in [MPa]

Figure 20: CREO parametric FEA approximations of the fold flat preload ring. Outer diameter of the preload ring is $D_0 = 105.8$ mm.

3.2.3 Pinhole Assembly

The pinhole assembly which is used to mount and align the pinhole plate.



(a) Overall overview of pinhole assembly.

(b) Pinhole assembly without protective caps.

Figure 21: Overview of the pinhole assembly. The black xy flexure stage has outer dimensions of 40 mm

XY stage

The xy -flexure stage from Thorlabs, App. A.3.1, is used to provide fine xy -motion, Fig. 21b. A range of 0.5 mm in both x and y with a resolution of $200 \mu\text{m}/\text{rev}$. The fold mirror is also adjustable, this ensures that little range is required for the xy stage. The stage's material is stainless steel and therefore has a different coefficient

of thermal expansion (CTE) than the rest of the assembly's structure. In order to prevent thermal effects such as creep in between bake-out cycles, CTE compensators have been implemented. This allows for the xy stage's mounting components to move and reposition, ensuring that the position of the xy -flexure stage after a bake-out maintained. More about the CTE compensation in 3.2.3. [1]

Rough Z positioning

For the first positioning of the xyz -pinhole stage, the assembly can slide over 3 poles. Using integrated clamps a rough z -location of the pinhole can be obtained, see Fig. 21b. The poles are fixed with flexures on the collimator interface plate, and on the xyz stage structure. The collimator interfacier place is mounted on the collimator structure and can easily be placed or removed. As required pinhole location is at an offset from the interfacing collimator plate, a muzzle is added. This muzzle reduces stray-light being coupled in, Fig. 22.

Z stage

In Sec. 3.1.3 a single hinge stage has been selected to provide the required z stage motion. The rotational motion is provided using a single flexure hinge element Fig. 24a mounted at an offset of the pinhole plate, Fig. 22.

The fine tunable z motion can be obtained using an adjustment screw. The preload of two springs are used to ensure constant contact of the adjustment screw with the structure.

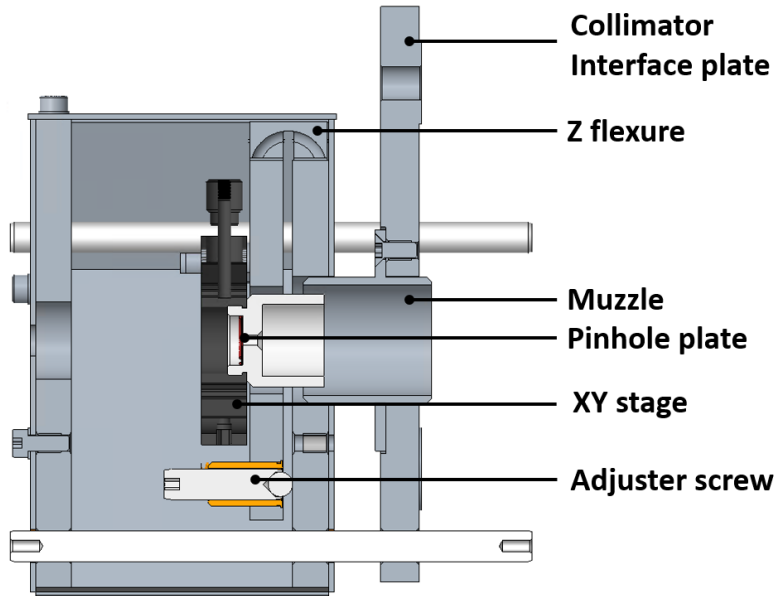


Figure 22: Side view of pinhole stage assembly, with flexible element providing z -motion in red.

Casing

As seen in Fig. 21a, plating has been added to the pinhole assembly. These elements ensure a light tight environment around the pinhole plate. The lids also protect the alignment of the pinhole against unwanted perturbations.

The point source is generated by the pinhole, however multiple light input sources can be chosen still during the PLATO testing campaign to illuminate the pinhole. The casing allows for a modular interface to allow for future input optic elements, while still retaining a light tight environment.

Dimensioning

CTE flexers

Difference in thermal expansion of the Thorlabs xy flexure stage (made from stainless steel Construction) compared to the rest of the pinhole assembly (made from AL6082-T6) is small but significant. For the temperature cycling through a range of $20^{\circ}\text{C} - 100^{\circ}\text{C}$, the distance between mounting location of the stage and of the base differs at its maximum $14.4\ \mu\text{m}$. This has been calculated using Eq. 12 and the thermal expansion coefficients of the used aluminum (α_{AL}) and stainless steel (α_{316}), App. A.3

Using the Eqs. 12, 13, 14, 15 an approximation of the maximum stress in the material of ≈ 112 MPa is found. The approximations, are a first estimation. As the Eqs. 13, 14 and 15 are based on beam theory, which holds for long and slender beams. The flexures in survey are short and thick.

With the simulation toolbox of PTC Creo, an approximation has also been made to verify the predicted values. The element size of the FAE mesh has been limited to a maximum of 0.5 mm. A maximum stress of ≈ 97 MPa is found, Fig. 23

Both approximations for maximum stress remain well below yielding properties of the aluminum, App. A.3. [19] [20]

$$dL = L_0(\alpha_{AL} - \alpha_{316})\Delta T = 14.4 \mu\text{m} \quad (12)$$

$$\sigma_{max} = \frac{1}{4} \frac{F_x L t}{I} \approx 112 \text{ MPa} \quad (13)$$

$$F_{CTE} = C_{CTE} dL \quad (14)$$

$$C_x = \frac{E_{SS} w_{CTE} t_{CTE}^3}{L_{CTE}^3} \quad (15)$$

$$\alpha_{AL} = 23 \times 10^{-6} K^{-1}, \alpha_{SS} = 16 \times 10^{-6} K^{-1}, \Delta T = 80^\circ C$$

$$E_{SS} = 70 \text{ GPa}$$

$$w_{CTE} = 6.5 \text{ mm}, t_{CTE} = 1 \text{ mm}, L_{CTE} = 5.2 \text{ mm}$$

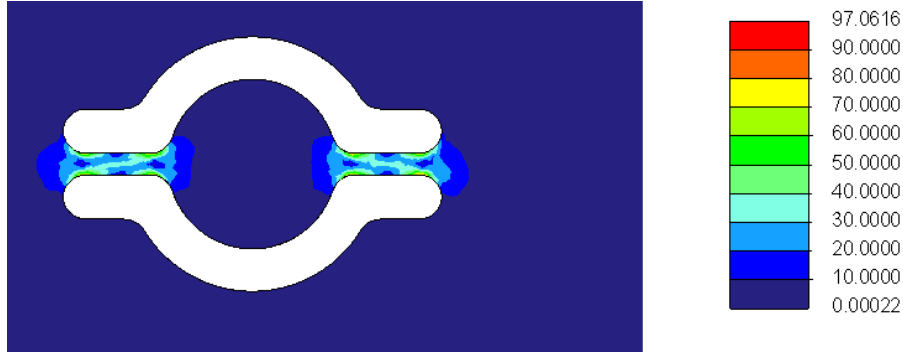


Figure 23: Thermal expansion difference compensators under deflection. Units are in [MPa]

Z stage The stage consists of a single flexure hinge element. Fig. 24a. To allow for a minimum total range of $z_{range} = 0.9$ mm, as approached in Sec. 3.1.3. The parameters of the flexure element are as follows: thinnest wall of the hinge h , diameter of the circular cutout of D . The width of the flexure element is t . The arm from the axis of rotation to the pinhole location is $L_{pinhole}$ with an arm further to the actuating adjustment screw at L_{screw} . There has been optimized for a maximum adjustment range, minimum stresses in the component and remaining in-house manufacturability.

The material of the flexure element is of Aluminium 6082-T6, which is the same of the overall pinhole assembly structure. Using Eqs. 16 and 17 we find a maximum stress of $\sigma_{max} = 189$ MPa at a maximum achieved range of the pinhole of $z_{range} = 0.6$ mm. However stress concentrations can be expected due to the flexure's geometry. Further verification using a FEA has therefor been performed. [20]

$$R_y = \arcsin\left(\frac{z_{range}}{L}\right) \quad (16)$$

$$\sigma_{max} = 0.58E \sqrt{\frac{h}{D}} R_y = 189 \text{ MPa} \quad (17)$$

$$(18)$$

$$h = 1.6 \text{ mm}, D = 15 \text{ mm}, t = 20 \text{ mm}$$

$$L_{pinhole} = 42 \text{ mm}, L_{screw} = 70 \text{ mm}$$

Preload Adjusters

A force is required to move the pinhole and actuate the z hinge flexure to max deflection against the stiffness of the hole hinge. Using Eq. 22 with stiffnesses of Eqs. 18, 20 and 21 a force can be estimated. Using the differences distance of the pinhole to the flexure $L_{pinhole}$ and the adjuster to the pinhole L_{screw} , Eq. 23 predicts the force required for maximum range for the adjustment screw is $F_{screw} = 22.5$. [20]

Springs supply the pretension ensuring constant contact between the adjustment screw and its mechanical interface. As a rule of thumb for the pretension, 5 times the required adjustment force has been decided, at maximum deflection.

$$K_{Ay} = 0.093Eth^2 \sqrt{\frac{h}{D}} \quad (19)$$

$$C_{Az} = 0.56Et \sqrt{h/D} \left(\frac{1}{1.2 + \frac{D}{h}} \right) \quad (20)$$

$$C_{bz} = \frac{C_{Az}K_{Ay}}{K_{Ay} + C_{Az}L^2} \quad (21)$$

$$F_{screw} = z_{range}C_{bz} = 36.9 \quad (22)$$

$$F_{Bolt} = F_{pinhole} \frac{L_{Pinhole}}{L_{bolt}} = 22.5 \quad (23)$$

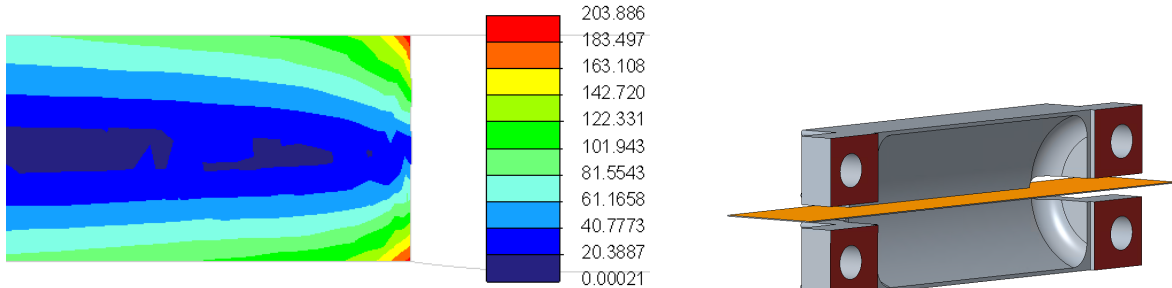
Verification Z stage

The z stage flexure is expected to contain stress concentrations. Recall that, using the Eqs. 16 - 23, an estimation has been made for amount of actuating force that is necessary at the adjuster screw location ($F_{screw} = 22.5$ N). In order to achieve a $z_{range} = 0.6$ mm of one sided deflection. Doing so, a maximum stress of $\sigma_{max} = 189$ MPa has been found.

To verify that the maximum stresses in the flexure remain below the yield limit and that the predicted load on the adjuster screw is correct a FAE simulation has been done. The simulation uses the aforementioned parameters for the z stage and the *PTC CREO Parametric 4.0 simulation* package, with maximum mesh element size of 0.5 mm, which is $\sim 1/3$ of the smallest wall thickness of the component. Fig. 24a, is contour plot of the Von Mises stresses in the plane as seen in Fig. 24b. The contour plot is zoomed in around the expected stress concentrations of the hole hinge.

The force F_{screw} is presented as input at the actuation offset of L_{screw} . Here the software calculates a deflection of $z_{range} = 0.56$ mm, using $F_{screw} = 19$ N of force as input parameter. While generating a maximum of $\sigma_{max} = 203$ MPa of localized stress. As the number do seem to be in the same ball park as the calculations in Sec. 3.2.3, there are discrepancies. Most likely the difference in values can be accounted to local stress hot-spots.

Here, the localized stresses are difficult to remove. Conventional CNC milling always leaves some fillets, due to a minimum mill head diameter.



(a) Stress concentrations due to fillets around the slotted holes. Units are in [MPa]

(b) Cut plane from Fig. 24a

Figure 24: CREO parametric FAE approximations of the pinhole z stage flexure.

Pinhole pole clamp mechanism

To lock the pinhole assembly in place along 3 poles a clamping mechanism is introduced. A hinge flexure supplies the required motion to secure the structure based on friction along the poles.

The hole flexure has been designed with AL6082-T6 as the base material and the following parameters. The plate thickness (t), hole diameter of the hinge (D), the thin wall of the hinge (h) and the distance from the rotating hinge to the hole that acts as the clamp (L_{clamp}). For the suitable deflection (u_{clamp}) a worst-case misaligned and oversized hole was considered.

Using the Eqs. 24 and 29, a maximum stress in the hinge of 205 MPa is found at maximum single sided deflection which is below the materials yield.

Furthermore, with the same maximum perturbation, a fastener is used at a distance of L_{bolt} from the hinge. Using Eqs. 24 - 30, it is found that the fastener has to produce $F_{bolt} = 40.6$ N, working against the hinge's stiffness. [20]

The M3 A2-70 bolt, which is used, considering a friction coefficient of 0.3, can supply a maximum preload force of 1.35 kN, which is well above the required clamping force. Leaving most of the fastener's potential preload available for clamping the pole. [23]

$$[H]R_y = \arcsin\left(\frac{u_{clamp}}{L_{clamp}}\right) \quad (24)$$

$$C_{ax} = 0.56Et\sqrt{\frac{h}{D}}\left(\frac{1}{1.2 + \frac{D}{h}}\right) \quad (25)$$

$$K_{ay} = 0.093Eth^2\sqrt{\frac{h}{D}} \quad (26)$$

$$C_{bz} = \frac{C_{az}K_{ay}}{K_{ay} + C_{az}L^2} \quad (27)$$

$$F_{clamp} = u_{clamp}C_{bz} \quad (28)$$

$$\sigma_{max} = 0.58E\sqrt{\frac{h}{D}}R_y = 205 \text{ MPa} \quad (29)$$

$$F_{bolt} = F_{clamp}\frac{L_{clamp}}{L_{bolt}} = 40.6 \text{ N} \quad (30)$$

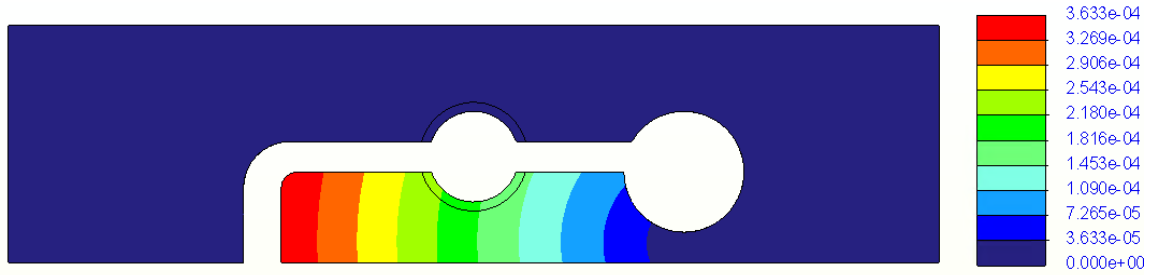
$$t = 7 \text{ mm}, D = 8 \text{ mm}, h = 2 \text{ mm}$$

$$L_{clamp} = 14 \text{ mm}, L_{bolt} = 22 \text{ mm}$$

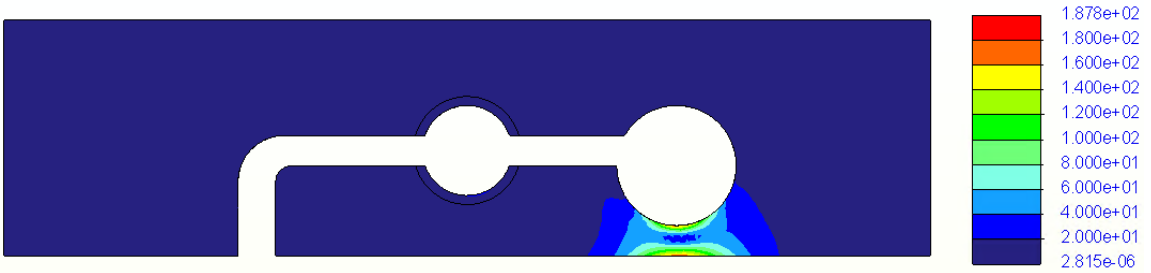
$$u_{clamp} = 0.2 \text{ mm}$$

In order to verify the approached maximum stress and predicted required actuation force a CREO FAE simulation has been done, using the above parameters.. The meshed element size has been limited to a maximum of 0.5 mm, which is $\sim 1/4$ of the smallest wall thickness.

The actuating force $F_{bolt} = 40.6$ N has been used as input at the location of the fastener hole. This resulted in a displacement plot, Fig. 25a. From which a displacement of $\sim u_{clamp} = 0.2$ mm can be approximated. Fig. 25b is a display of stresses in the material, reaching a maximum of $\sim \sigma_{max} = 188$ MPa, which is less than found using Eqs. 24 and 29, and below the yield of the material, App. A.3.



(a) Displacement plot of the pole clamping mechanism. Units in [m]



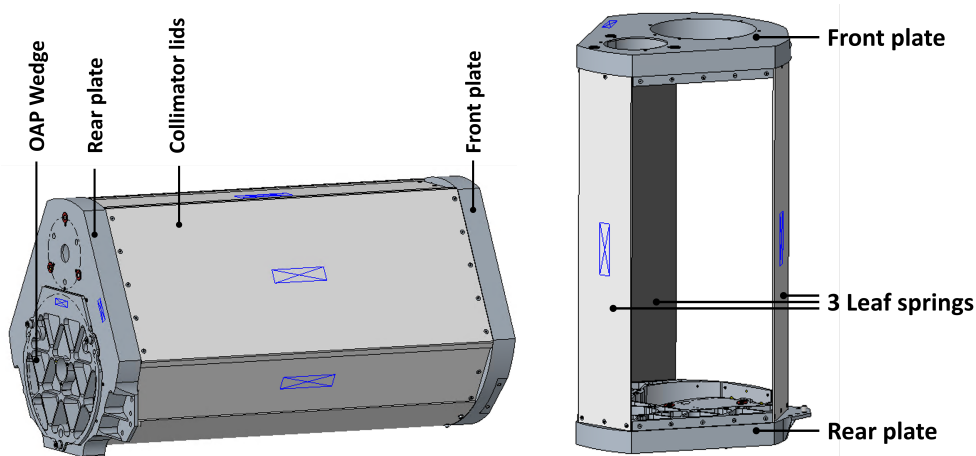
(b) Stress view of the pole clamping mechanism. Units in [MPa]

Figure 25: Pole clamp under loading

3.2.4 OGSE Structure

The overall collimator structure ensures an interface of the optical components to the OGSE support structure, Sec. 1 and/or the test-bench set-up. Doing so, the OGSE structure is a rigid base interfacing to the OAP assembly, fold flat assembly, pinhole assembly, alignment cube, OGSE Support, wiring equipment, etc. as seen in Tab. 9. Assembly results can be seen in App. A.4.1.

Concept generation and selection as well as detailed design are beyond the scope of this thesis.



(a) Overall CAD representation of assembled collimator structure without subassemblies. (b) Representation of the collimator structure during assembly, without light tightness caps. Leaving 3 leafspring.

Figure 26: Collimator structure. Overall length of collimator structure front to back is ~ 610 mm

Kinematic base of the structure

The overall OGSE structure consists of 2 main plates, these plates have ribs added to remove unnecessary mass but remain stiff. The rigid plates are connected with 3 leaf springs. On one side thoroughly fastened. The other side bolted with one center fastener, effectively generating a hole hinge in each leaf spring. This ensures the 2 main plates of the structure to be kinematically exactly constrained. The three leaf elements can be seen

in Fig. 26b. Assembly of the structure occurs in the upright position from Fig. 26b, to introduce as little stresses while assembling as possible. Figures of assembly can be seen in App. A.4.1 and Fig. 46, where the Figs. 46a and 46b denote Figs. 26a and 26b respectively.

Lids

Closing the OGSE structure lids are placed. Preventing unwanted light from coupling in. The lids also ensure a closed environment around the optical component, such that contamination is kept out of the collimator's vital parts. The closed structure can be seen in Fig. 26a.

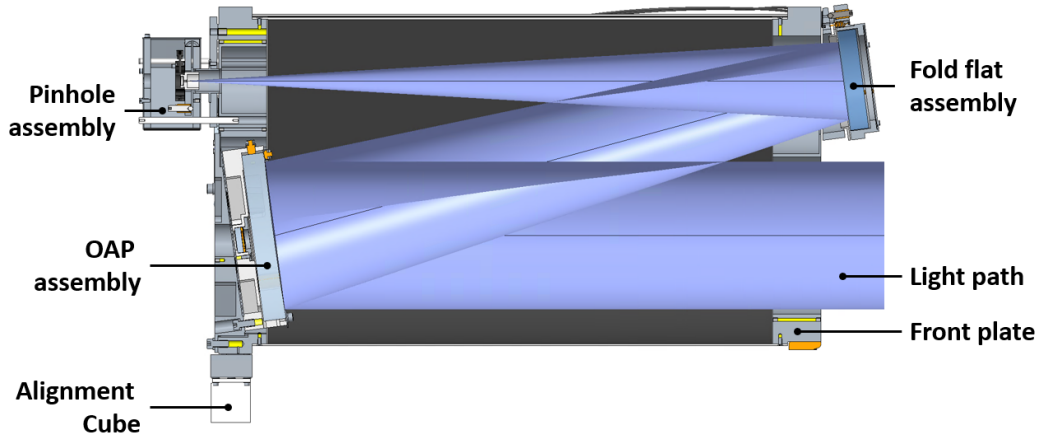


Figure 27: Cut views of the collimator with subassemblies and light path, which originates from the pinhole assembly. Including the subassemblies, overall length is ~ 750 mm

3.3 Design Validation

To validate the design, the optical performance of the individual optical components has been investigated. This to verify that the mechanical design does not jeopardize required optical performance.

Multiple FEA have been performed using the "Simulate" Toolbox of PTC CREO Parametric 4.0. Input for the analyses has been predicted mechanical loading and gravity effects.

OAP surface deformation

The off-axis parabolic mirror is under mounting load and gravity load. Before the OAP is integrated in the collimator, it will be characterized, as mentioned in Sec. 3.1.2 and 4.2. The proposed set-up, see [AD1], for this characterization will feature the OAP assembly in a different orientation as in the collimator. Thus, the direction of the gravity load acting on the optic differs during characterization with respect to final use. To verify that the gravity load does not introduce significant WFE, an FEA has been performed. The element size has been limited to a maximum 2 mm. OAP material and dimensional parameters can be found in Sec. 3.1.2 and App. A.1.2.

Fig. 28 shows a deflection plot for deflections in x -direction (coordinate system as taken from the figure), which is the orthogonal direction with respect of the reflective surface. As seen in the figure, the surface under deflection of gravity load resembles a coma wavefront aberration. Subtracting the maximum positive deflection with the maximum negative deflection, an approximate peak-to-valley surface error of 0.11 nm is estimated. At the required operational 700 nm wavelength (Tab. 2), this results in a $\sim \lambda/64$ surface error. The eventual WFE due to the surface error of the optic is doubled. Thus a $\sim \lambda/32$ exit WFE is introduced and therefor can be considered negligible.

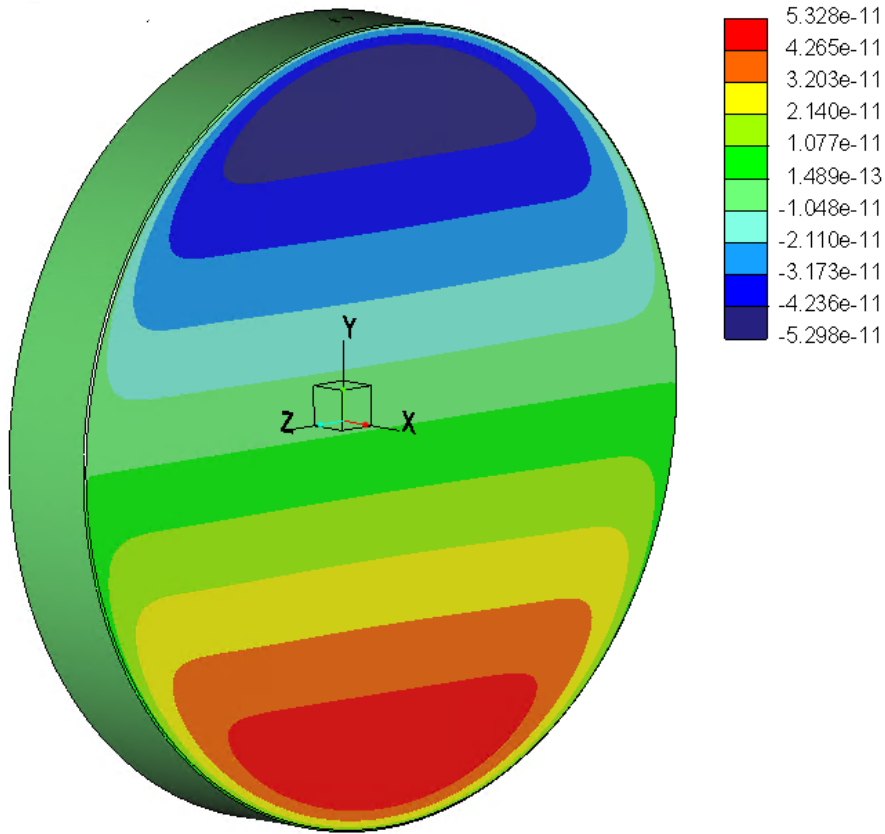


Figure 28: Deflection of the OAP's reflective surface under gravity load. Units are in [m]. Diameter of the Optic $D_{OAP} = 170$ mm

The OAP experiences loading due to mounting forces. These forces interact with the OAP structure, causing stress, strain and thus surface deformations. The mounting forces, calculated in 3.2.1 are used as input, as well as the axial and radial supports.

Deformations are expected to be largest at the locations where the mounting force interacts with the OAP substrate. However, for optical performance, only the central 150 mm of the OAP is of interest.

In Fig. 29, the out-of-plane displacement of the central 150 mm is plotted, subtracting the maximum with the minimum deflection adds up to an approximate peak-to-valley surface error of 33.0 nm. Which results in a $\sim \lambda/21$ surface deformation of the optic, which translates to $\sim \lambda/11$ WFE peak-to-valley. Which can be considered negligible with respect to the required $\sim \lambda/4$ peak-to-valley output beam WFE.

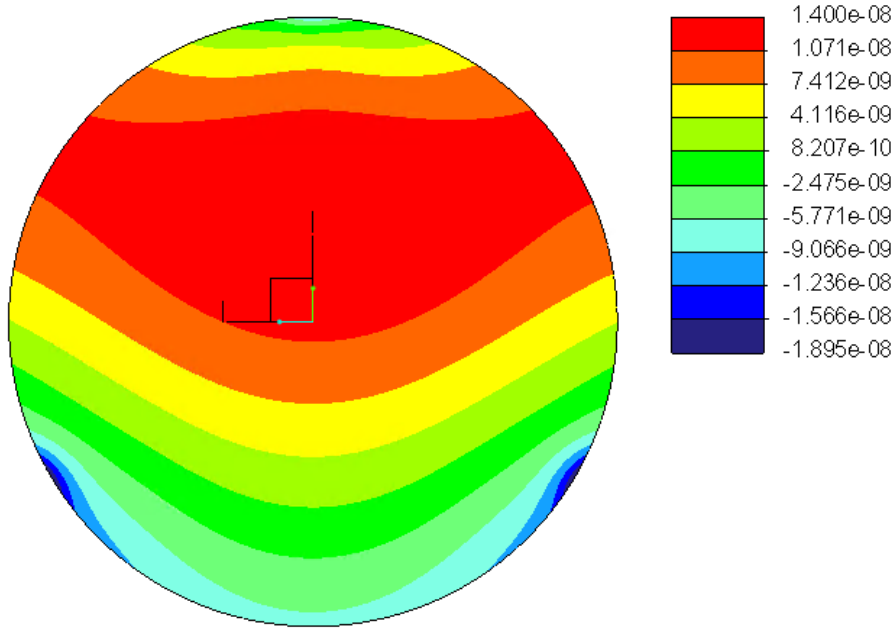


Figure 29: OAP under axial and radial loading. Units are in [m]. Diameter of surface under test $D = 150$ mm

Fold flat surface deformation

As with the OAP, the fold flat experiences a mounting and gravity load. Fig. 30 is the deflection plot of the deflection orthogonal to the reflective surface.

Using the ZEMAX model parameters, see App. A.1.1, the aperture of the fold flat that is nominally being used has a diameter of ~ 80.3 mm. The flat is oversized, without any markings that enable localization of the nominal center. Therefore a margin is introduced, and the central 91.4 mm is analyzed.

The mesh element size has been limited to a maximum of 2 mm.

Subtracting the maximum positive and negative deflection a total of 4.70 nm is approximated. Which results in a surface deformation in the order of $\sim \lambda/149$, for the 700 nm wavelength for operational use. Contribution of output WFE will result be in the order of $\sim \lambda/74$ peak to valley. This can be considered as negligible.

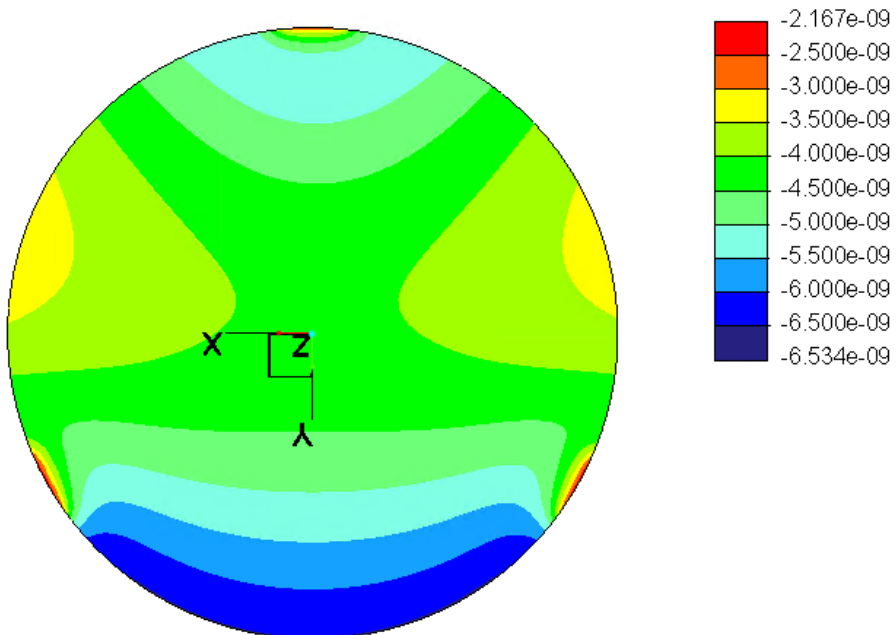


Figure 30: Fold flat under axial loading. Units are in [m]. Diameter of surface under test $D = 91.4$ mm.

Deformed pinhole

Nominally, the pinhole is a circle with diameter D_0 . Actuating the z motion, there is rotation generated about the z hinge flexure, Sec. 3.2.3. This changes the virtual shape of the pinhole as observed by the collimator optics into an oval, where one diameter remains unchanged (D_0), and the other does not (D_1).

Maximum deflection of the z motion at z_{range} is considered. The distance of the pinhole with respect to the rotation of the z hinge is $L_{pinhole}$. Using Eqs. 31, 32 and 33 we find that $D_1 - D_0 = -3.1$ nm. Which is expected to have insignificant effect on the performance of the collimator.

There is also a small lateral parasitic effect, being Δy . As defined in Fig. 7. The amount of parasitic movement in its maximum adjustment range (z_{range}) and pinhole offset with respect to the hinge element ($L_{pinhole}$), can be calculated using Eq. 34. Which results in a lateral parasitic movement of $\Delta y = 0.14$ μm . This, regarding the tolerances of Tab. 8, can be seen as negligible.

$$\theta_y = \arctan\left(\frac{Range_z}{L_{pinhole}}\right) \quad (31)$$

$$D_1 = \cos(\theta_y) D_0 \quad (32)$$

$$D_1 - D_0 = -3.1 \text{ nm} \quad (33)$$

$$\Delta y = Range_z \tan(\theta_y) = 0.14 \mu\text{m} \quad (34)$$

$$D_0 = 30 \mu\text{m}$$

$$z_{range} = 0.6 \text{ mm}$$

$$L_{pinhole} = 42 \text{ mm}$$

4 Realization

The amount of energy, financial costs and time spend on a project significantly increase when the manufacturing, assembly and alignment testing phase commence. A thorough realization plan is therefore vital in keeping the aforementioned costs of a project within reasonable boundaries.

4.1 Assembly

A structured approach to assembly ensures that as time and effort spent during this phase is minimized. Before the start of this step, it is vital to have preparations in order.

The order of manufacturing and assembly is as follows.

1. **OAP assembly**, starts with characterizing the off-axis parabolic mirror, as other elements can still be manufactured. Potential unexpected offsets of the OAP's mechanical interfaces with respect to the optical known coordinate system can still be accounted during design and manufacturing the collimator structure - OAP interface.
2. **Collimator structure**, manufacturing and assembling starts after the OAP, which allows for following components to be directly placed, removing the necessity of storing sub-assemblies separately. No detailed design has been provided in for this thesis. Assembly results can be seen in App. [A.4.1](#).
3. **Fold flat assembly** is aligned before the pinhole is aligned ([AD1]).
4. **Pinhole assembly** is the final step in the alignment procedure after optimizing towards the required WFE ([AD1]).
5. **Alignment cube assembly** after the collimator is fully aligned, its line of sight can be characterized with respect to the line of sight of the alignment cube. No detailed design has been provided in for this thesis.

Integration of the subassemblies onto the collimator structures has been described in the alignment procedure [AD1]. Here, placing the optical components at a nominal position is described, ensuring a first rough alignment. This assembly procedure is therefore handled in the alignment procedure [AD2].

4.1.1 Integration of the OAP

Before the alignment procedure, Sec. [4.2](#), the OAP assembly has been test-fitted in the collimator structure. As seen in Fig. [31](#).

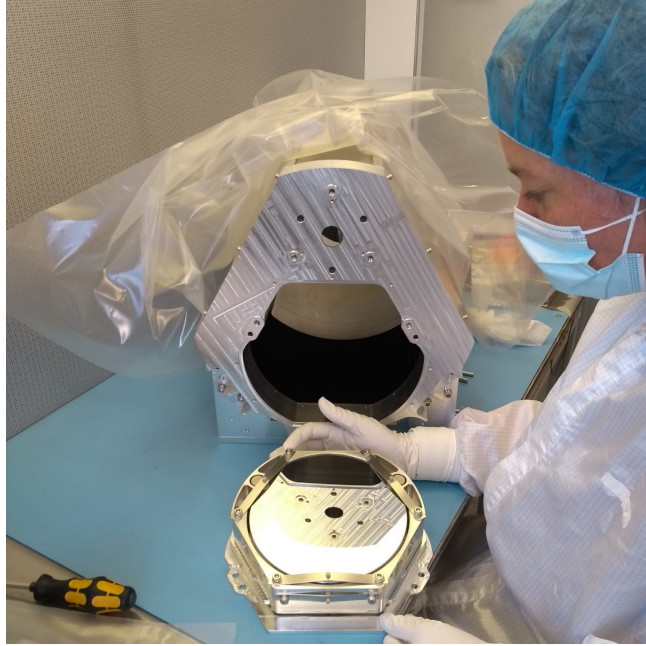


Figure 31: Fit checking the OAP subassembly in the collimator structure.

4.1.2 Integration of Fold Flat Assembly

Placing an optical component requires extra care in order not to damage or contaminate the optic. To place the fold flat in its structure, a simple procedure has been developed, Fig. 32. Which shows that, firstly a separate tool (shown in black) is placed that supports the fold flat, Fig. 32(a). In Fig. 32(b) the assembly is lifted, lifting the optic as well. Next, in Fig. 32(c), the black tool can be removed. In such a way, the optical component can be placed without the need to touch the reflective surface or the sides of the component. Now, the retainment ring can be placed, Fig. 32(d), and the preload ring can be tensioned as well, Fig. 32(e). Resulting in a structurally placed optical component in its retaining assembly.

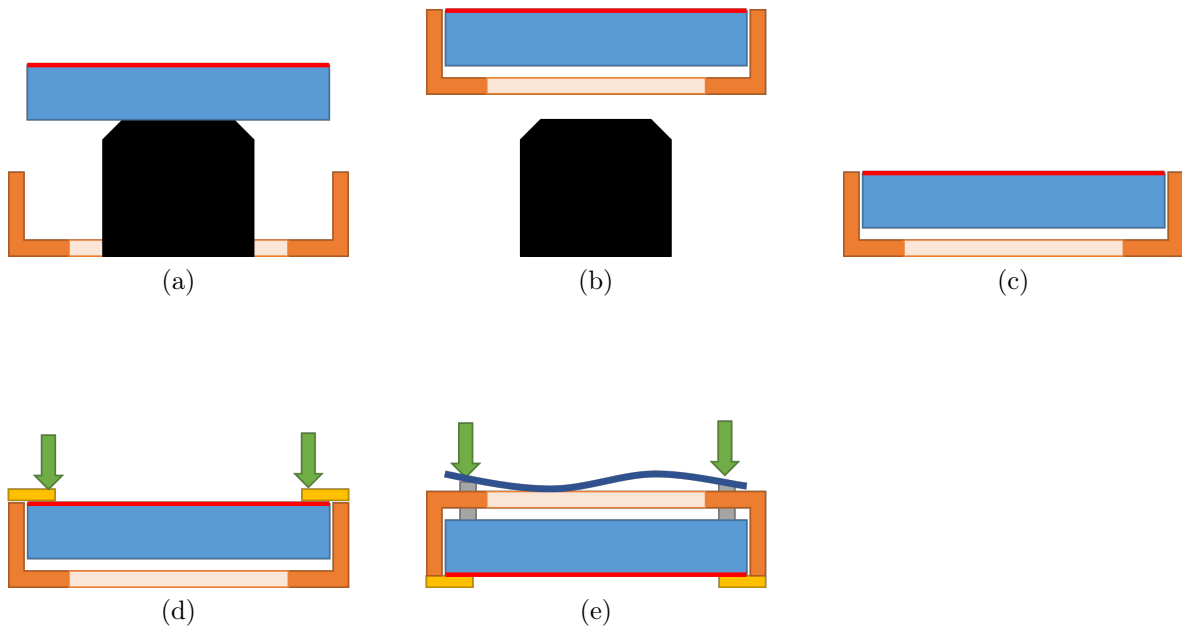


Figure 32: Schematic representatio of step by step procedure of placing the fold flat in its retainer.

Assembly of the fold flat subsystem has successfully been completed, using the above mentioned integration strategy, Fig. 33. The figure caption per step from Fig. 32 correspond with Fig. 33. The final step, in Fig.

33(f), shows the fold flat assembly as integrated onto the collimator structure.

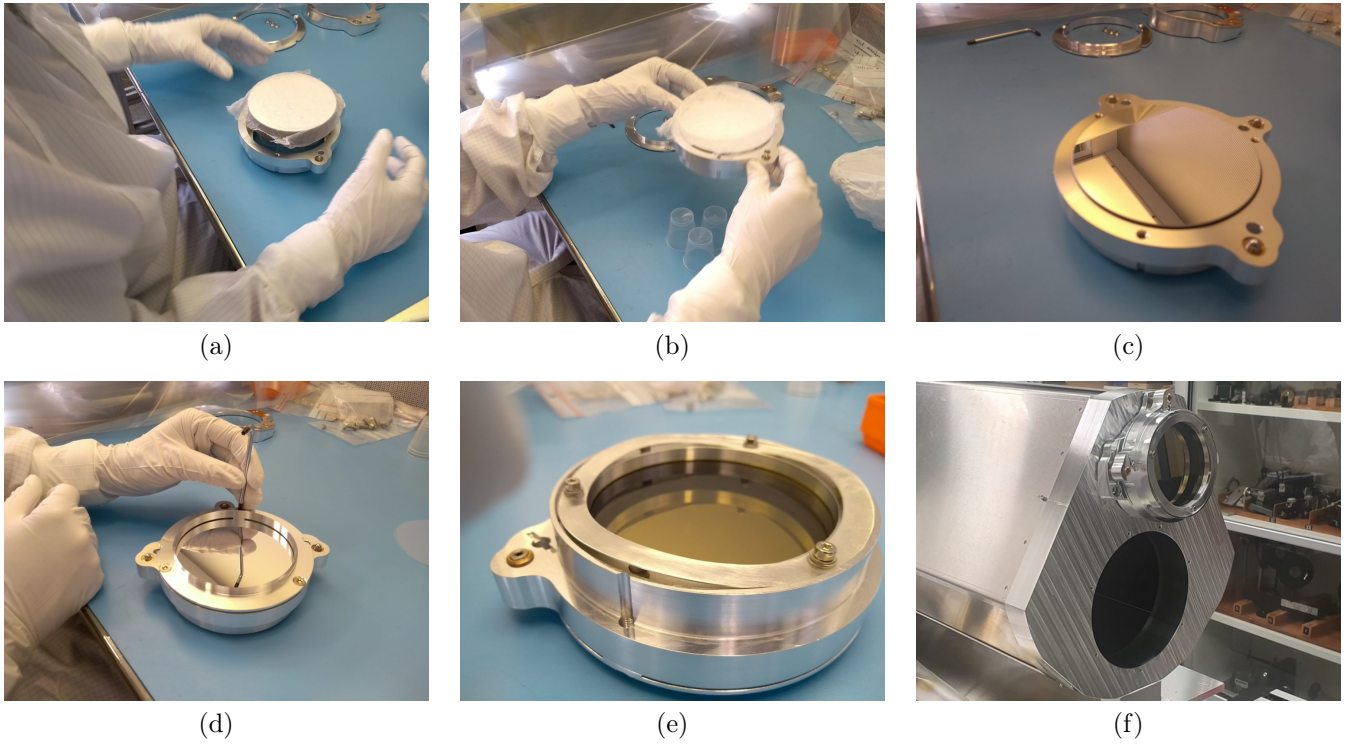


Figure 33: Implementation of fold flat placement strategy during assembly.

4.1.3 Integration of Pinhole Assembly

The pinhole system being assembled and integrated.

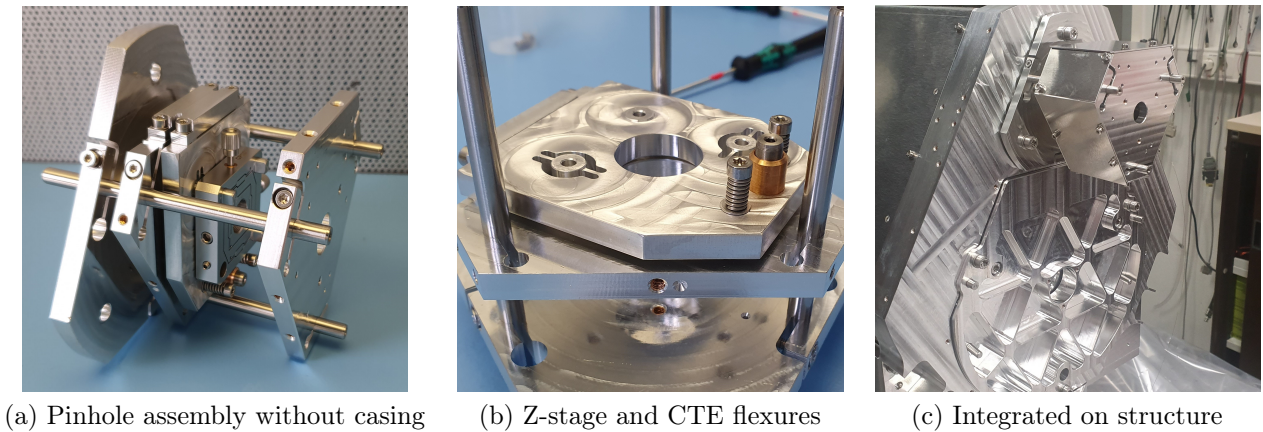


Figure 34: Pinhole subsystem being assembled and integrated.

4.2 Alignment

For the collimator to have the required optical performance, alignment is necessary. As such, the structure and corresponding elements have to be able to reside in an aligned state for the specifications to be met. In Sec. 2.2.2 the need for alignment has been discussed, based on the single element tolerances, Tab. A.1.5. However, aligning an optical system is not trivial, especially with multiple optical elements and partially defined pieces of optics. As is the case with the collimator of this project. The collimator and the alignment procedure has been designed concurrently.

4.2.1 Procedure

The alignment procedure document consists of 4 chapters. Where the final chapter is the collimator alignment procedure, this in itself is based on 4 major alignment phases, as listed below [AD1]

1. Defining the optical axis of the OAP
2. Rough alignment using theodolite
3. Final alignment of focus position and LoS using Mahr interferometer
4. External reference cube LoS

Each of these phases have structured step by step instructions and pass/fail criteria in order to converge to a well aligned collimator. Adhering to the set performance requirements, see Tab. 2.

Theodolite

For alignment and LoS characterization, a theodolite is used. This measuring equipment can be seen in operation in Figs. 37b and 37c. More information about the theodolite and its use can be found in App. A.5.

Autocollimator

Using interaction with the collimator structure will be required. For example during mounting of the subassemblies or adjusting using the alignment mechanisms. For checking the stability of the collimator with respect to the optical bench an autocollimator is used. More about the autocollimator in App. A.5.

4.2.2 Report

The alignment report is essentially the filled in alignment procedure. Where each step has been marked pass/failed and important values of measurements are noted, following the procedure. Final measurements/offsets are averaged.

Results: 1. Defining the optical axis of the OAP

When the direction of the OAP's optical axis has been found. The offset of the line of sight of the OAP reference mirror, Sec. 3.2.1, with respect to the OAP's optical axis has been calculated and expressed in the coordinate system of the OAP, Tab. 14. These are averaged values over multiple measurements [AD2].

The single OAP, mounted sideways can be seen in Fig. 37a.

Δ OAP Ref θ_x	$0^\circ 6' 45''$
Δ OAP Ref θ_y	$-7^\circ 6' 45''$

Table 13: Offsets of OAP Reference LoS with respect to the OAP optical axis in the OAP coordinate system [AD2]

Results: 2. Rough alignment using theodolite

The result of this second step is a roughly aligned collimator. For the next step, *fine alignment of the focus position and LoS using Mahr interferometer*, it is good practice that an initial alignment already produces a usable signal. To get the measuring optical devices to work right away proves to be valuable and very time efficient. [AD2]

To obtain the orientation of the OAP the previously characterized OAP reference mirror has been used. In Fig. 37b a theodolite obtains the LoS of the OAP reference mirror. With the known offsets of the OAP reference mirror LoS and the OAP's optical axis (from 1. *Defining the optical axis of the OAP*) a first approximation of the collimator LoS has been made. This is further explained in the Alignment Procedure [AD2].

During assembly it became clear that one of the endplates of the collimator structures had not been manufactured to the correct dimensions. Fastener holes had been offset by a significant amount, leaving the collimator structure shorter than expected. Finding the extra alignment range using the rough z positioning (Sec. 3.1.3) during this alignment phase became crucial.

Results: 3 Final alignment of focus position and LoS using Mahr interferometer

In the alignment procedure, the focus position (generated by the interferometer) is optimized for minimal WFE. To optimize the WFE produced by the OAP, the alignment procedure of the manufacturer Optical Surfaces is used. A final alignment with a peak to valley WFE of 134 nm has been achieved, Fig. 35. Which translated, at 700 nm to $\sim \lambda/5.2$. This is an averaged value over 30 measurements. Fig. 35 shows the surface contour plot of the measured WFE. In the left column, the individual Zernike term contributions are shown. [16] [2]

When the surface plot of the WFE, Fig. 35, is compared with the surface contour plot of the test report from the manufacturer of the OAP, A.1.2, similarities can be spotted. Certain shapes in the surface plot seem to correspond, which raises the assumption that the surface error of the OAP is the main contributor to the final WFE. Giving the idea that the other optical surfaces contribute less, as expected. And that an optimum of collimator alignment has been found.

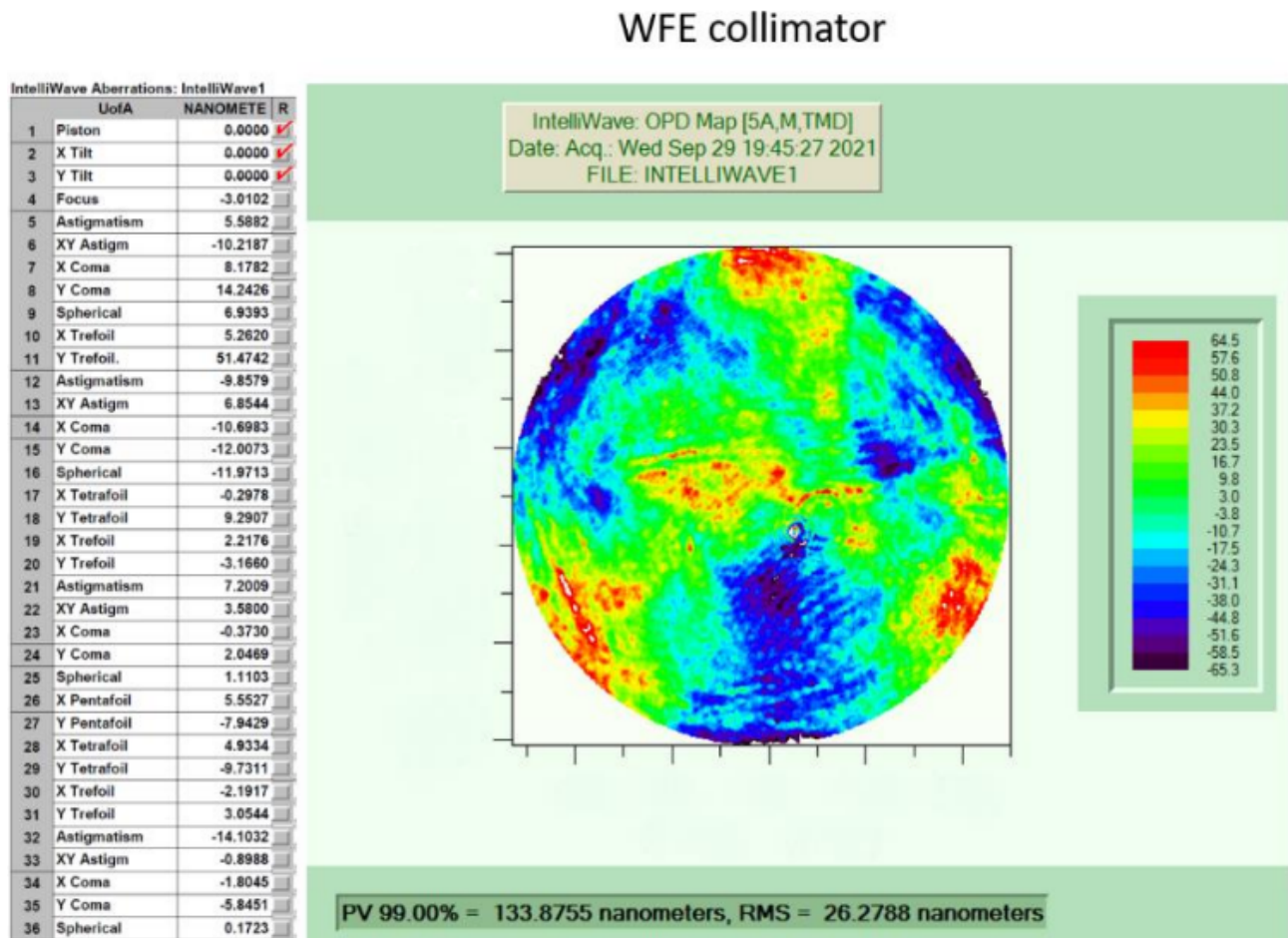


Figure 35: Summary of averaged WFE results.[AD2]

Note that the *X Tilt* and *Y Tilt* have not been included in the WFE measurement. As the *XTilt* and *YTilt* will be nulled out in the test set-up using the gimbal stages, Sec. 1.3.

Following the alignment procedure, the interferometer is used in a double-pass configuration. The surface errors of the collimator reflective surfaces therefor are added twice in the interferogram. To measure the output wavefront as is, the Mahr interferometer is set to 2 waves per fringe. Correctly measuring the output WFE. The wavefront measurement, analysis and averaging have been done using the IntelliWave software, delivered with the Mahr interferometer. [24] [AD2]

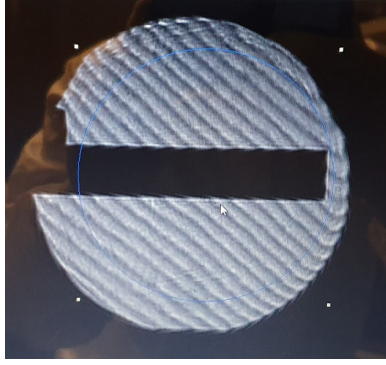


Figure 36: Physically checking the digital mask definition

The Mahr interferometer has adjustable magnification option. Which is mechanically regulated and difficult to quantitatively characterize. To be certain that the required 150 mm diameter bundle is under survey, extra steps have been made. By physically measuring a diameter of 150 mm correct digital mask dimensions can be checked. Fig. 36 exhibits how a quick check with a ruler and a piece of tape can be carried out. This example is given for illustrative purposes and is not used for mask definition. Another strategy implemented were introducing a 150 mm diameter aperture, with the similar effect.

Results: 4. External reference cube LoS

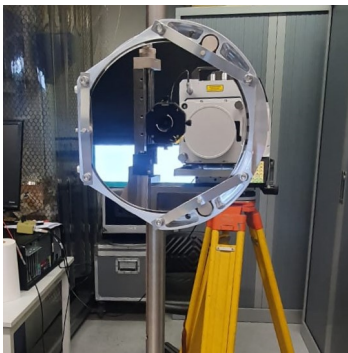
Phase 4 of the procedure expresses the offset of the alignment cube line of sight(LoS) with respect to the collimator LoS in the coordinate system of the collimator. Doing so, the collimator LoS can later easily be determined by examining the alignment cube LoS.

In App. A.5, *in situ* external alignment using a theodolite can be seen.

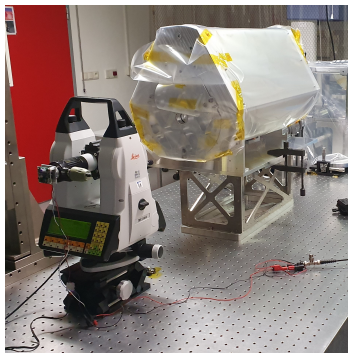
The theodolite is used for these characterizations. In Fig. 37c, the theodolite is used to obtain the collimator LoS.

$\Delta\theta_x$ OGSE Cube wrt OGSE LoS	$0^\circ 26' 3''$
$\Delta\theta_y$ OGSE Cube wrt OGSE LoS	$0^\circ -7' 36''$

Table 14: Offsets of OGSE Cube with respect to the OGSE LoS in the OGSE coordinate system. [AD2]



(a) Single OAP assembly for alignment step 1.



(b) Measuring LoS of the OAP reference mirror.



(c) Measuring LoS of the collimator.

Figure 37: Pictures of carrying out the alignment procedure [AD2].

5 Validation

5.1 Tests

5.1.1 Wavefront

During the alignment procedure, Sec. 4.2 ([AD1]). The metric for optimization has been the WFE. For this measurement, as described in the report ([AD2]), the Mahr interferometer generates a interferogram which travels double-pass through the collimator. The outgoing output beam is reflected using a large 200 x 200 mm reference flat.

As test and verification that the collimator performs well, this WFE test is used. Fig. 35 shows the contour plot and Zernike decomposition of the WFE.

The WFE measurement, Fig. 35, also includes the surface error of the reference flat. A check with a smaller circular, 4" flat, which has been recently characterized to be $\lambda/10$, proves no significant changes in WFE when using the same mask. No other large high quality flats have been readily available to improve the statistic.

5.1.2 Bake-Out

Changing the PLATO camera in between test cycles, a bake-out is performed of the entire test facility, Sec. 2.1.2. This consists of elevating the temperature in the vessel from room temperature ($\sim 20^\circ\text{C}$) up to 100°C), during which the facility experiences a vacuum. This state is then held for multiple days before it is cooled back to room temperature and the vacuum is removed.

To check for creep of the optical components the orientation of the optical component is measured, before and after a bake-out. Using a theodolite the LoS of the alignment cube, the OAP reference flat and the fold flat can easily be measured. Where the LoS of the fold flat can be obtained through its rear, as explained in Sec. 3.1.2. The line of sight of the collimator can also be picked up with a theodolite.

Using a theodolite, the following offsets have been measured.

- Fold flat LoS with respect to the collimator LoS
- Alignment cube LoS with respect to the collimator LoS
- Alignment cube LoS with respect to the OAP reference mirror LoS

The above mentioned offsets have each been averaged over three times. Before and after a bake-out cycle. The difference of the averaged values before and after the cycle can be found in Tab. 15. The values show that after bake-out virtually no movement has been detected. Especially realizing that the offsets from Tab. 15 resemble individual measurement inaccuracies. The measurements can be found in App. A.6.1.

Fold flat with respect to Collimator LoS	ΔH_z	1.7''
	ΔV	3.7''
Alignment Cube with respect to Collimator LoS	ΔH_z	6.0''
	ΔV	4.3''
Alignment Cube with respect to OAP reference	ΔH_z	1.3''
	ΔV	4.3''

Table 15: Difference in LoS offsets before and after bake-out

5.2 Requirements

Revisiting the requirements of Sec. 2, the individual requirements can be determined a pass or fail.

Property	Requirement	Unit	Pass/Fail
WFE (peak-to-valley)	$\leq \lambda/4$ at 700	nm	Pass

Table 16: Table of collimator performance requirements.[AD2]

WFE (peak-to-valley)

The optimal WFE, after alignment, has been measured and averaged in Fig. 35. For $\leq \lambda/4$ at $\lambda = 700$ nm the WFE is ~ 174 nm. The WFE after alignment has been found to be ~ 134 nm, which is well below the $\lambda/4$, thus the optical performance is met. [AD2]

Property	Requirement	Unit	Pass/Fail
Temperature	20	$^{\circ}C$	Pass
Pressure	1	mPa	Pass
Cleanliness		Stable after bake-out	Pass

Table 17: Table of environmental collimator requirements.

Temperature

The assembly and alignment have been accomplished in room temperature environments, being the same expected thermal environment for the collimator to be used in. Therefore, it is expected to be able to perform likewise.

Pressure

Assembly, alignment and characterization have been done in a sea-level atmospheric environment. Which is not the atmospheric pressure during operation. However, during the bake-out, the collimator has experienced an elevated thermal environment as well as a vacuum. As the bake-out has been successful, it can be concluded that the collimator is able to maintain a vacuum, without an excess of virtual leaks. Moreover, performance is maintained after the atmospheric pressure is reinstated, which has been analyzed in Sec. 5.1.2. Thus it can be concluded that the collimator can operate in a vacuum environment. [AD3] [AD7] [AD8]

Cleanliness

Part of ensuring cleanliness of the structure is the bake-out protocol, Sec. 2.1.2. Maintaining optical performance after bake-out is proven in Sec. 2.2.3. Which has been analyzed in Sec. 5.1.2.

To keep the structure clean from contamination. Thorough attention has been given to avoid exposing the collimator to contamination threads. A test facility bake-out will be held, during which contamination will be measured to finalize the facility readiness.

Property	Requirement	Unit	Pass/Fail
Output beam diameter	150	mm	Pass
Volume envelope (\odot x L)	394 x 900	mm	Pass
Mass	≤ 15	kg	pass
Angular beam stability	0.1	$arcsec$	TBD
Positional accuracy	2	mm	TBD
External Alignment	Characterized alignment cube		Pass
Integration	\odot 651	mm	Pass [AD3] [AD5]

Table 18: Table of collimator performance requirements.

Output beam diameter

The required collimator output beam diameter of 150 mm has successfully been reached. As the required beam diameter has been used during the alignment phase, Sec. 4.2.2.

Volume envelope

The outer dimensions of the OGSE collimator, as is, are: 362 mm x 751 mm (\odot x L). Which is within the maximum volume envelope from, Tab. [AD3].

Mass

Using the assembly model CAD model, a total mass has been found of 11.24 k, which is well below the maximum allowable mass. Even though this has not been verified experimentally, handling the collimator suggest this to be correct. The mass requirement can be concluded to be met.

The collimator can easily be handled by one person. Integrated in the test set-up, the support structure behaves as expected.

Angular beam stability

The long term angular beam stability has yet to be characterized. Resolution of the test equipment has not been high enough to test collimator budget for angular stability directly. Such tests are planned and will most likely be performed with the collimator integrated in the test facility, characterizing the total stability budget.

Translational accuracy

Lateral positional accuracy has not yet been verified. Tests are planned to verify test facility alignment as an complete system.

External alignment

As part of the external alignment, the alignment cube has been placed and has been fully characterized, Sec. 4.2.2. The offsets of the alignment cube LoS with respect to the collimator LoS in the coordinate system of the collimator have been found. Thus external alignment has been successful.

Integration

The OGSE collimator has an outer diameter volume claim of 362 mm. This enables the entire structure to fit through the rearward opening hole of the vacuum tank, which has a diameter of 651 mm.

As a validation, the collimator has already been integrated in the test facility.

Property	Requirement	Pass/Fail
Time	5 October 2021	Fail
Cost	\leq €30.000, –	Pass

Table 19: Table of organizational requirements [AD4]

Time

The final alignment of the collimator was performed on 29 September 2021 (see Fig. 35), Sec. 4.2.2, and marked the system as ready. However, integration with the input optics and verification after bake-out had yet to commence. The collimator as a complete system was therefore not ready for integration at the required time. Other crucial components, that had to be integrated before the collimator were not ready yet as the whole project encountered some unexpected delays.

Cost

For the PLATO project at SRON, the available budget is closely monitored by the project leader. The project lead has been satisfied with the total costs of the collimator, therefore we can conclude that the realization of the collimator has been within budget.

6 Conclusion and Recommendations

The objective of this thesis was to provide final design, realization and characterization of a 150 mm diameter collimator with a wavefront error (WFE) of $\leq \lambda/4$ at 700 nm. This collimator will be a component of the PLATO camera test facility at SRON. The test set-up will be used to test and characterize single PLATO mission cameras separately. The thermal vacuum test set-up mimics the operating conditions during flight while a star will be simulated by a collimated beam, filling the full entrance pupil of the camera.

6.1 Conclusion

To determine which key aspects drive the design, the requirements have been broken down for each phase of the project. This results in structured design selections for final design and required specifications for validation and characterization.

The most demanding requirements include stable and reproducible optical performance, vacuum environmental conditions and cleanliness demands. The vacuum requirements enforce material restrictions, and the cleanliness demands require the TV test facility to undergo a periodical bake-out, cycling through a temperature profile under vacuum conditions, after which the required optical performance has to be retained.

Based on the requirements, several opto-mechanical concepts were generated for the collimator's optical components and alignment tooling. After concept selection, a detailed opto-mechanical design was made for all components and structures.

The conceived design includes mounting a 170 mm diameter off-axis parabolic mirror, 100 mm diameter fold flat and a pinhole in a 9.6 mm diameter foil. Alignment mechanisms have been designed for the sensitive degrees of freedom of the fold flat and pinhole.

For the realization phase, a comprehensive alignment procedure has been designed to guarantee successful alignment and validation.

The collimator has been manufactured, assembled, aligned and validated. The alignment procedure resulted in a WFE of $\lambda/5.2$ at a 700 nm wavelength over a 150 mm diameter beam.

The objectives of this thesis have been fulfilled. The collimator as a characterized well performing subsystem of the thermal vacuum test facility has been integrated into the test facility. This finalizes the integration of the thermal vacuum test facility which is now successful in operation.

6.2 Recommendations

Testing

To improve the understanding of the collimator behavior, and building more statistics on collimator performance, extra characterization and validation tests should be introduced.

Angular beam stability should be characterized as the collimator is integrated in the system, validating that long term angular drift is within the testing limitations. Also, a positioning check on lateral beam location should be conducted, ensuring that the full entrance pupil of the PLATO camera is always being filled.

Thermal stability should be checked periodically after a bake-out, to verify that drifts due to thermal effects have not occurred.

Collimator Limitations

Real-time WFE measurements during operation cannot be obtained due to lack of available optical measuring equipment. Thus, once aligned and in operation, the optical quality of the outgoing beam cannot be measured. As such the WFE after bake-out has not directly been characterized. Also, *in situ* or periodically WFE measurement will reduce optical performance uncertainty of the test set-up. Implementing this feature for the full 150 mm output beam diameter will require extra tooling and equipment.

The collimator is required to produce a uniform light intensity profile. This performance requirement has not been part of this thesis. Hence no further research in optimizing or validating the light uniformity profile has been done.

Uniformity can be improved by for example adding structure such as baffles or an anti-reflective coatings to reduce stray light which will improve camera test results

Input Optics

One of the most important interfaces of the collimator is the input optics. The OFP has been well defined by positioning the pinhole plate while modularity. Multiple input optics solutions that illuminate the pinhole plate can be integrated if required.

Illuminating the pinhole has not been part of this thesis. However, integration options have been investigated and a working solution has been presented, as can be found in App. [A.7](#).

Applicable Documents

Ref.	Title	Doc. no.	Issue
[AD1]	PLATO Collimator Alignment Procedure	PLATO-SRON-PL-PRO-0002	1.0
[AD2]	PLATO Collimator Alignment Reports	PLATO-SRON-PL-RP-0032	1.0
[AD3]	PLATO test facility - Mechanical Design Description	PLATO-SRON-PL-TN-0002	3.0
[AD4]	Detailed WFE analyses of OGSE collimator	PLATO-SRON-PL-TN-0001	2.2
[AD5]	OGSE Design Description for PLATO CAM TVAC Test	PLATO-SRON-PL-DD-0002	1.0
[AD6]	Requirement Specification for the PLATO Camera Test Facility	PLATO-SRON-SP-0002	1.0
[AD7]	Cleanliness Control Plan for Camera test facility	PLATO-SRON-PL-PLN-0001	1.0
[AD8]	SRON-PLATO Contamination budget breakdown	PLATO-SRON-PL-PLN-0001	1.0

Bibliography

- [1] Thorlabs Inc., *Thorlabs*. <https://www.thorlabs.com>, 2021.
- [2] Optical Surfaces LTD, *OptiSurf*. <https://www.optisurf.com>, 2021.
- [3] Amatec Technische Veren B.V., *Amatec*. <https://www.amatec.nl/nl/w1004011.html>, 2021.
- [4] Edmund Optics inc, *Edmund Optics*. <https://edmundoptics.com>, 2021.
- [5] EO Portal, *PLATO*. <https://directory.eoportal.org>, 2021.
- [6] SRON, *PLATO*. <https://www.sron.nl/missions-exoplanets/plato>, 2020.
- [7] G. Aitink-kroes, “PLATO Mechanical Design Trade Off,” *Design Trade Off*, vol. 2.0, no. PLATO-SRON-PL-TN-005, 2019.
- [8] Energetiq, “Eq-99xfc ldlTM,” tech. rep., 2020.
- [9] Energetiq, “Fiber Optic Cable Assemblies,” tech. rep., Energetiq Energetiq, 2020.
- [10] B. Vandenbussche, P. Royer, and W. Laauwen, “PLATO Camera Test Specification,” vol. 2.7, no. PLATO-KUL-PL-TS-0001, pp. 1–156, 2020.
- [11] Alcatel Vacuum Technology France, *Undetectable “ virtual ” leaks What is a virtual leak ?* Adixen, 2020.
- [12] D. Edwards, “The influence of virtual leaks on the pressure in high and ultra-high vacuum systems,” *Vacuum*, vol. 29, no. 4-5, pp. 169–172, 1979.
- [13] M. Verhaegen, G. Vdovin, O. Soloviev, P. Pozzi, and D. Wilding, *Control for High Resolution Imaging*. Delft Center for Systems and Control, Delft University of Technology, 2017.
- [14] ECSS, *ECSS-Q-ST-70-01C: Space Product Assurance - Cleanliness and contamination control*. No. November, 2008.
- [15] M. Laauwen, “SRON Camera AIT Plan STM,” *Plan*, vol. 1.0-, no. PLATO-SRON-SP-PLN-0006, 2020.
- [16] Optical Surfaces LTD, “Off-Axis Paraboloid Alignment Procedure,” tech. rep.
- [17] H. Soemers, *Design Principles for Precision Mechanisms*. T-Point Print VoF, Enschede, 2010.
- [18] Qioptiq Photonics GmbH & Co., *Qioptiq*. <http://www.qioptiq-shop.com/en/Precision-Optics/>, 2021.
- [19] J. Cool, *Werktuigkundige Systemen*. Delft Academic Press, 2013.
- [20] JPE, *Precision Point*. JPE Innovations, 2021.
- [21] MKS, *Newport*. <https://www.newport.com/>, 2021.
- [22] M. Koster, *Constructieprincipes*. Amersfoort: Universiteit Twente, 5 ed., 1998.
- [23] TR Fastenings, *Stainless Steel Fasteners*. <https://www.trfastenings.com>, 2021.
- [24] Intellwave Technologies, *IntelliWave*. <https://www.intellwavetechnologies.com/>, 2021.
- [25] OHARA Inc., “OHARA product information,” *CLEARCERAM*, 2006.
- [26] Schott, “ZERODUR[®] Zero Expansion Glass Ceramic Catalogue,” <https://www.schott.com/zerodur>, 2011.

A Appendix

A.1 Optical Elements

A.1.1 Zemax Nominal Design

Lens Data X

Update: All Windows

Surface 0 Properties Configuration 2/2

Surface	Surface Type	Commer	Radius	Thickness	Material	Coating	Clear Semi-Dia	Chip Zone
0	Standard	Point so...	Infini...	0,00000000000000			0,00000000000000	0,0000...
1	Coordinate Break			672,03760756680083	-		0,00000000000000	-
2	Coordinate Break	Rot_fold		0,00000000000000	-		0,00000000000000	-
3	Standard	Fold	Infini...	0,00000000000000	MIR...		40,13638173708949	0,0000...
4	Coordinate Break	-Rot_fold		0,00000000000000	-		0,00000000000000	-
5	Coordinate Break	w_colli		-602,14977034882702	-		0,00000000000000	-
6	Standard	OAP 2501...		0,00000000000000	MIR...		170,80000000000001	U -
7	Coordinate Break	w_colli		600,00000000000000	-		0,00000000000000	-
8	Standard	STOP	Infini...	0,00000000000000			75,00000057790226	U 0,0000...
9	Standard	Image	Infini...	-			75,00000000000000	U 0,0000...

1: 3D Layout X

Settings Line Thickness

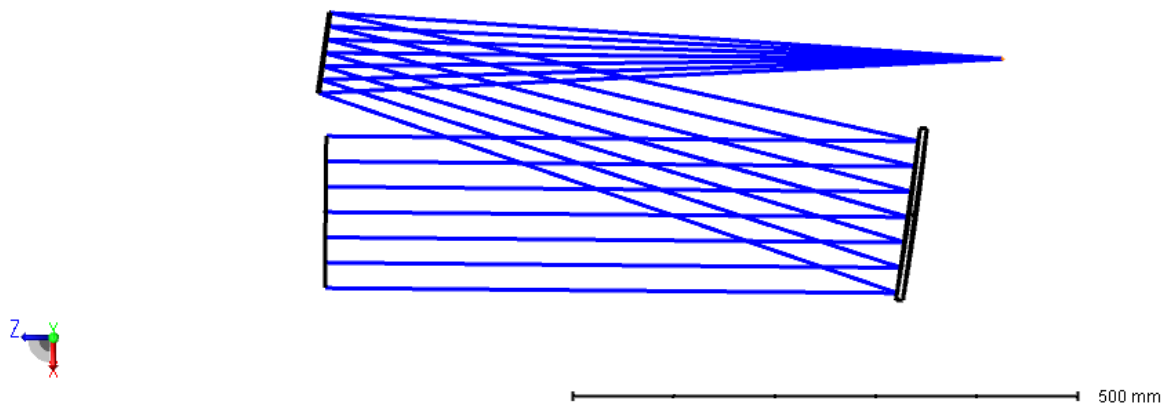


Figure 38: ZEMAX software screenshot of nominal positioning of optical components. Top: Lens Data Editor window. Bottom: Schematic representation of collimator layout.

A.1.2 Off-Axis Parabolic Mirror Specifications

Diameter	170 mm
Clear Aperture	150 mm
Focal Length	1250 mm $\pm 1\%$
Apparant Focal Length	1272 mm (nominal)
Off-Axis Distance	300 mm (+5/-0 mm)
Off-Axis Angle	15° (nominal)
Edge Thickness	23 mm
Surface Accuracy	$\lambda/8$ at 633 nm
Substrate Material	ClearCeram-z (HS)
Coating	Protected Aluminium (AL + MgF)
Mounting	Unmounted

Table 20: Specifications of the OAP catalog.

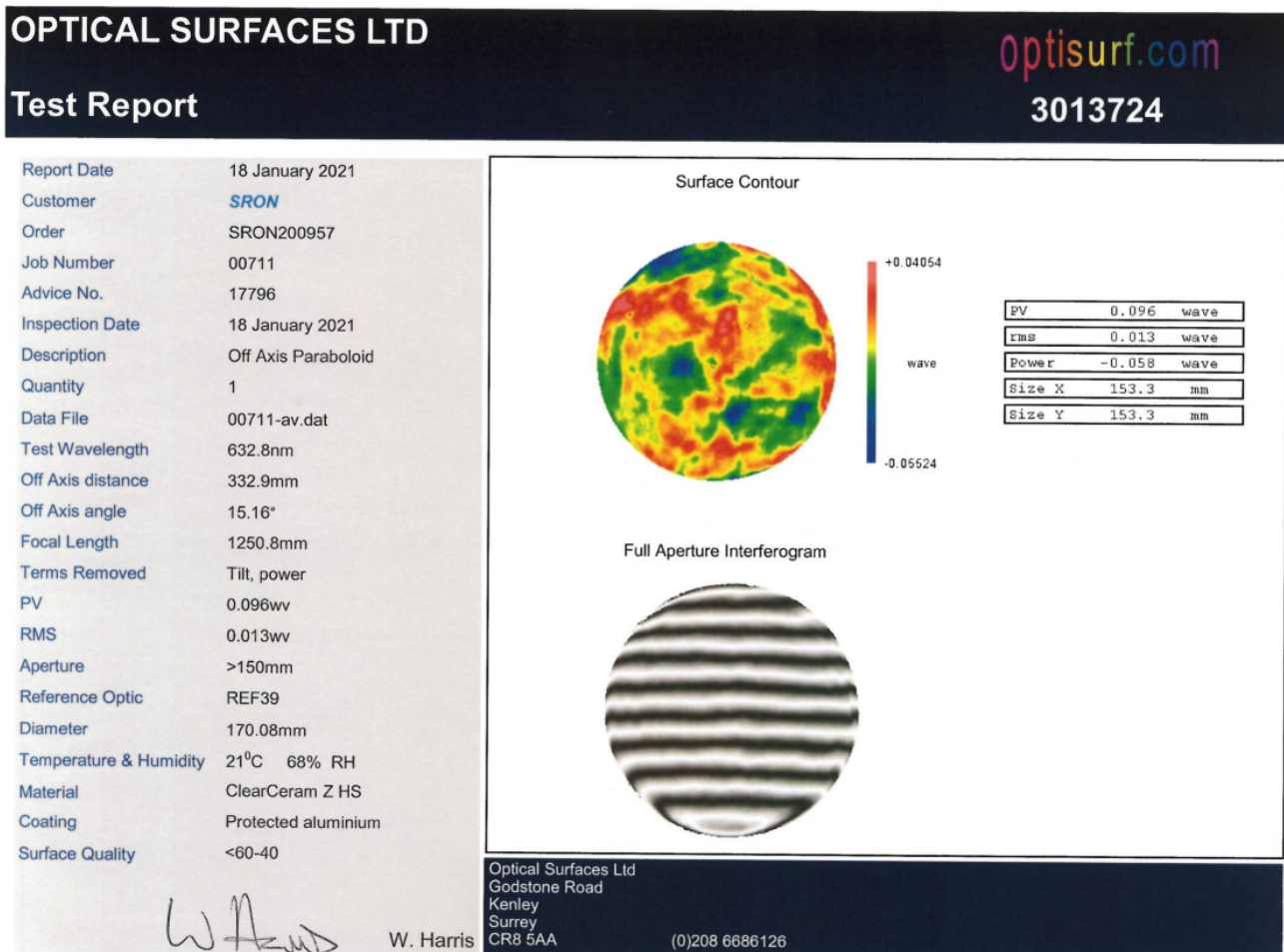


Figure 39: Test data from the manufacturer or the off-axis parabolic mirror. [2]

A.1.3 Fold Flat Specifications

Diameter	101.6 mm +0.0-1.0 mm (4 inch)
Clear Aperture(CA)	91.44 mm
Edge Thickness	19.1 mm \pm 1.5 mm
Surface Flatness	$\lambda/4$ at 633 nm Peak-to-Valley
Surface Quality	60-40
Substrate Material	ZERODUR
Coating	Protected Aluminium
Back surface	Commercial Polish
Wavelength Range	400 nm - 2000 nm
Mounting	Unmounted

Table 21: Specifications of the fold flat. [4]

A.1.4 Pinhole Plate Specifications

Diameter foil	9.6 mm
Diameter aperture	30 μ m \pm 2 μ m
Foil thickness	50 μ m
Mounted	Mounted in 1 inch holder
Foil material	300 series Stainless Steel

Table 22: Specifications of the pinhole foil [1].

A.1.5 Tolerances Collimator Optics

Parameter	Sensitivity	Limit	Notes
Fold mirror			
xi	Parameter Limit ($\partial x_i / \partial \Phi$)	Limit	
x	NA	NA	
y	NA	NA	
z	$dz = \Delta y * \cos(\alpha/2) / \tan(\alpha/2)$ or $dz = 0.5 * \cos(\alpha/2) * \Delta y$	225,9231415 or 24,78612153	μm
Θ_x	$d\Theta_x = 0.5 * \arctan(\Delta y / L_1)$	0,002565483	deg 0,00 ° 0,00 ' 9,24 "
Θ_y	$d\Theta_y = 0.5 * \arctan(\Delta x / L_1)$	0,002565483	deg 0,00 ° 0,00 ' 9,24 "
Θ_z	NA	NA	
OAP			
x	$dx = - \Delta x$	-30	μm Defocus effects due to
y	$dy = \Delta y / \cos(\alpha)$ or $dy = - \Delta z / \sin(\alpha)$	30,25886882 or -383,0648788	μm Θ_x and Θ_y
z	$dz = - \Delta z / \cos(\alpha)$ or $dz = - \Delta y / \sin(\alpha)$	-50,43144803 or -229,8389273	μm are negligible
(wedge angle) Θ_x	$d\Theta_x = - 0.5 * \arctan(\Delta y / L_2)$	0,001427636	deg 0,00 ° 0,00 ' 5,14 "
Θ_y	$d\Theta_y = \arctan(\Delta x / L_2 * \cos(\alpha))$	0,002855264	deg 0,00 ° 0,00 ' 10,28 "
Θ_z	$d\Theta_z = \arctan(\Delta x / L_2 * \sin(\alpha))$	0,002855264	deg 0,00 ° 0,00 ' 10,28 "
Point Source			
x	$dx = \Delta x$	30	μm Coordinate system of point
y	$dy = \Delta y$	30	μm source coincides with
z	$dz = \Delta z$	50	μm
Θ_x	NA	NA	
Θ_y	NA	NA	
Θ_z	NA	NA	

Δx	30 μm
Δy	30 μm
Δz	50 μm
α	15 deg
L_1	670 mm
L_2	602 mm

Figure 40: Individual tolerance on optical element sensitivities

A.2 List of Components

Assembly	Subassembly	SRON name	Common name	[P/M]	Note
Collimator	OAP [343-G-1277]	343-J-1278	OAP Mount	M	Optic PEEK AISI316 AISI316, 3 times Optic PEEK
		343-X-9089	OAP Reference Flat	P	
		343-J-1285	OAP Ref Mirror Protection	M	
		343-J-1284	OAP Ref Mirror Cover	M	
		343-X-9090	OAP Axial Wavespring	P	
		343-J-1282	OAP Radial Spring	M	
		343-J-1280	OAP Axial Spring	M	
		343-X-9088	OAP Mirror	P	
		343-J-1283	OAP Radial Spring Plug	M	
	Fold Flat [343-G-1300]	343-J-1305	FF Mount Wedge	M	3 times PEEK, 3 times 3 times AISI316 Optic
		343-J-1303	FF Mount	M	
		343-J-1304	FF Mount Plate	M	
		343-X-9099	Adjuster Bushing	P	
		343-J-1301	FF Axial Plug	M	
		343-X-9089	Adjuster Screw	P	
		343-J-1302	FF Axial Preload	M	
		343-X-9097	FF Adjuster Spring	P	
		343-X-9100	Fold Mirror	P	
	Pinhole [343-G-1348]	343-X-9108	P30HK Pinhole Plage	P	Stainless Steel 2 times 2 times
		343-X-9107	CP1XY Stage	P	
		343-J-1353	Z Base	M	
		343-J-1352	Z Hinge	M	
		343-J-1351	Z Plate	M	
		343-J-1350	Endplate	M	
		343-J-1359	Z Plate Cover	M	
		343-X-9099	Adjuster Bushing	P	
		343-X-9089	Adjuster Screw	P	
		343-J-1349	Collimator IF Plate	M	
		343-J-1355	Bottom Cover	M	
		343-J-1354	Mount Stud	M	
		343-J-1356	Top Cover	M	
		343-J-1361	Pinhole Mount	M	
		343-J-1357	Side Cover	M	
		343-J-1358	Endplate Cover	M	
		343-J-1360	Collimator Baffle	M	
	343-J-1353	Z Base	M		
	343-J-1367	Angled Cover	M		
	Collimator Structure* [343-G-1041]	343-J-1308	Collimator Base	M	3 times 2 times IF to OAP Assy
		343-J-1309	Collimator Top	M	
		343-J-1044	Collimator Skin Bottom	M	
		343-J-1312	Collimator Basis	M	
		343-J-1313	Collimator Cover Plate	M	
		343-J-1340	Mirror-mount	M	
	*	343-J-1368	Alignment Cube Mount	M	Optic PEEK, 2 times PEEK 2 times
		000-009-0881	Ref Cube Retro	P	
		343-J-1310	Collimator Foot	M	
343-J-1311		Kinematic Guidance	M		
343-J-1327		OGSE Support Bracket R	M		
343-J-1329		OGSE Bracket Shim	M		
343-J-1326		OGSE Support Bracket L	M		
343-X-9102		Bal-tec TRH-75SM	P		
343-X-9103		Bal-tec VB-75-SM	P		

Table 23: Overview of the parts of the collimator assembly. [P/M] denotes whether the component is being manufactured inhouse or being procured. If the material is not specified, the component is either procured or manufactured of Al 6082-T6. *Detailed design not introduced in this thesis.

A.3 Materials

Material	Property	Symbol	Value	Unit
Aluminium 6082-T6 ¹	Youngs Modulus	E_{AL}	70	GPa
	Density	ρ_{AL}	2.71×10^3	kgm^{-3}
	Thermal Expansion Coefficient	α_{AL}	23×10^{-6}	K^{-1}
	Yield Strength	σ_{AL}^{max}	250	MPa
AISI 316 ¹ (Stainless Steel)	Youngs Modulus	E_{316}	186	GPa
	Density	ρ_{316}	7.916×10^3	kgm^{-3}
	Thermal Expansion Coefficient	α_{316}	16×10^{-6}	K^{-1}
	Yield Strength	σ_{316}^{max}	303	MPa
PEEK ¹	Youngs Modulus	E_{PEEK}	3.86	GPa
	Density	ρ_{PEEK}	1.28×10^3	kgm^{-3}
	Thermal Expansion Coefficient	α_{PEEK}	5.5×10^{-5}	K^{-1}
	Yield Strength	σ_{PEEK}^{max}	91.1	MPa
ClearCeram-Z HS ²	Youngs Modulus	E_{OAP}	92	GPa
	Density	ρ_{OAP}	2.55×10^3	kgm^{-3}
	Thermal Expansion Coefficient	α_{OAP}	0.2×10^{-7}	K^{-1}
ZERODUR ³	Youngs Modulus	E_{OAP}	92	GPa
	Density	ρ_{OAP}	2.55×10^3	kgm^{-3}
	Thermal Expansion Coefficient	α_{OAP}	0.2×10^{-7}	K^{-1}

- 1) SRON library
- 2) Manufacturere Ohara Inc. [25]
- 3) Schott AG [26]

A.3.1 Procured Mechanical Components

XY flexure stage

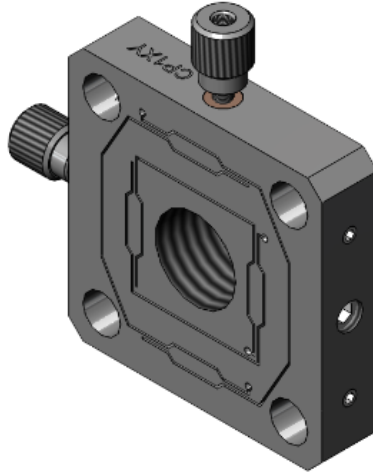


Figure 41: CAD representation of Thorlabs XY flexure stage. [1]

30 mm Cage XY Flexure Adjustment Plate	
Item	CP1XY
Travel	± 0.25 mm
Drive	M2.5 x 0.20 Fine Pitch Adjusters
Optic Mounting	SM05 (0.535" - 40) Thread
ER Cage Rod Connection	4 Through Holes with Side-Located Locking Screws
Vacuum compatibility	10^{-5} Torr
Material	Stainless Steel Construction
Resolution	200 $\mu\text{m}/\text{rev}$
Mass	0.12 kg

Table 24: Specifications of the xy flexure stage from Thorlabs. [1]

M6 adjuster



Figure 42: CAD representation of the M6 x 0.25, 25 mm adjustment screw from Thorlabs. [1]

Fine Hex Adjuster M6, 25 mm	
Item	F6MSS25
Diameter	M6
Pitch	0.25
Length	25 mm
Mass	0.01 kg
Tools	2 mm Hex Key

Table 25: Specifications of the M6 x 0.25, 25 mm adjustment screw from Thorlabs. [1]



Figure 43: CAD representation of the M6 x 0.25 bushing from Thorlabs. [1]

Fine Hex Adjuster M6 x 0.25 Bushing	
Item	F6MSSN1P
Diameter Threading	M6
Pitch	0.25
Bore Diameter	0.3395" +0.0005/-0.0000
Material	510 Phosphor Bronze
Vacuum Rating	10 ⁻⁶ Torr
Application	Slip Fit
Mass	≤ 0.01 kg

Table 26: Specifications of the M6 x 0.25 bushing from Thorlabs. [1]

Wave washer

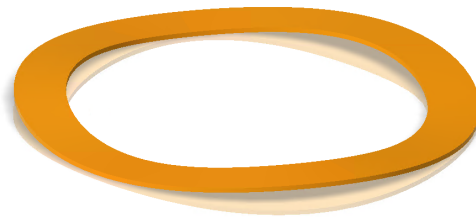


Figure 44: CAD of the wave washer from Amatec. [3]

Wave Washer	
Item	W1004011
Thickness (t)	0.27 mm
Outer Diameter (D_0)	25.50 mm
Inner Diameter (D_i)	19.81 mm
Unloaded Length (L_0)	1.80 mm
Loaded Length (L_1)	0.89 mm
Load at L_1 (P_1)	37.85 N
Material	AISI 316
No. of Waves	3

Table 27: Specifications of the wave washer from Amatec. [3]

Fold flat adjuster springs



Figure 45: CAD of the tension spring from Amatec. [3]

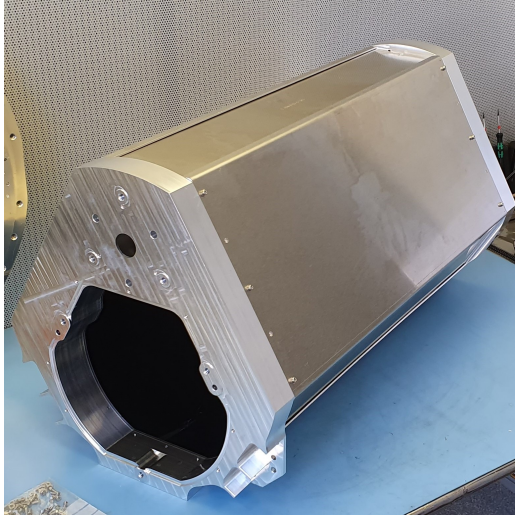
Wave Washer	
Item	E0240-041-1370X
Outer Diameter (D_0)	6.10 mm
Wire Diameter (d)	1.04 mm
Unloaded Length (L_0)	34.80 mm
Loaded Length (L_1)	42.40 mm
Load at L_1 (P_1)	27.74 N
Material	AISI 316
Pre-tension (T)	3.89 N
Spring constant (P_f)	3136.00 Nmm ⁻¹

Table 28: Specifications of the tension spring from Amatec. [3]

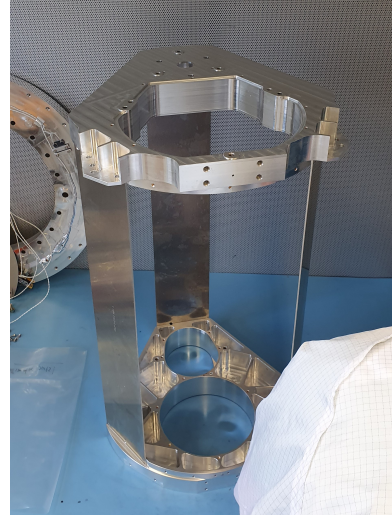
A.4 Assembly

- Some more assembly pics

A.4.1 Assembly of the Collimator Structure



(a) Assembled collimator structure.



(b) "Upright" position during assembly, as explained in Sec. 3.2.4.

Figure 46: Assembly of the collimator structure

A.5 Alignment

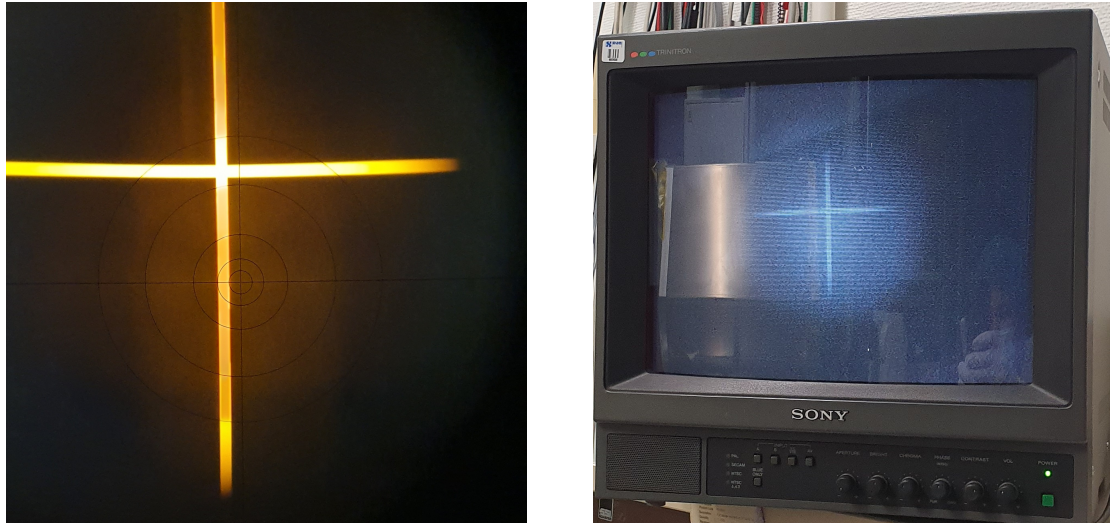
Theodolite

During alignment, a theodolite has been extensively used. In Sec. 4.2 the theodolite can be seen as being used. In Fig. 37b, the LoS of the collimator is measured and in Fig. 37b the OAP reference flat LoS is measured.

In Fig. 47a, the view is seen as one looks through the theodolite's ocular. The theodolite is aligned with the flat's LoS as the black crosshair is aligned with the bright orange return signal.

In some cases, a camera and an external display is required to view the theodolite's alignment. Such has been the case in Figs. 37b and 37b. The theodolite crosshair and return signal can be seen printed on an external display in Fig. 47b.

Resolution of the theodolite is characterized as ≤ 1 arcsec. Realistic alignment accuracy is limited by the user.



(a) User view of theodolite. The black crosshair denotes the theodolites alignment. Orange cross is the external display return signal from a reflective flat.

(b) User view of theodolite, used with a camera and return signal from a reflective flat.

Figure 47: Theodolite alignment views.

Autocollimator

The autocollimator is used to periodically check stability of the collimator with respect to the optical table. The following figures show how such a set-up is used.

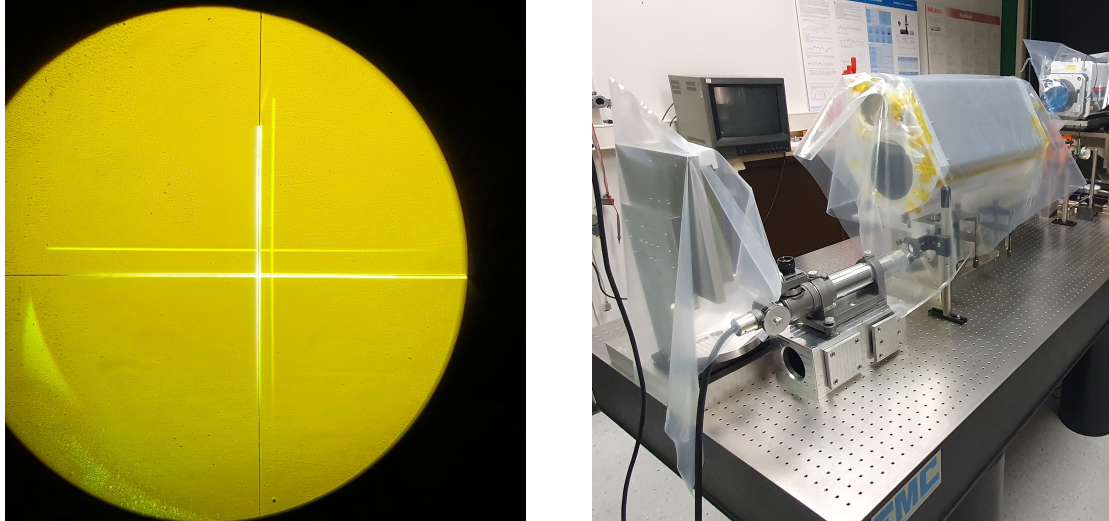
Fig. 48 shows the equipment denoted as autocollimator. This equipment is used to measure LoS of reflective surfaces and has a FoV of 10 *arcmin*. Light generation cannot be seen in Fig. 48.

In the stability set-up, Fig. 49b, two flats are presented to the autocollimator. A flat, rigidly mounted on the optical bench with high reflectivity and a flat mounted to the collimator structure with limited reflectivity. In Fig. 49a it can be seen how two different return signals are detected, where brightness correlates with reflectivity.

The two returnsignals from Fig. 49a show the LoS of two flats which are misaligned and a black crosshair, this crosshair is aligned with the brightest signal. Measuring the LoS offsets requires the autocollimator to align with both of the return signals and note both LoS respectively.



Figure 48: Autocollimator. Black ocular is used for measurement.



(a) View of autocollimator with two misaligned return-signal crosses. The autocollimator crosshair is aligned with the brightest return signal. (b) Autocollimator in the set-up. The collimator, interferometer and return flat are covered with clean-room plastics.

Figure 49: Autocollimator in use.

External Alignment

During external alignment of the OGSE with respect to the camera, 3 references are measured. With the measured reference LoS, the LoS of the collimator and of the camera are aligned, as explained in Sec. 1.3.1. In Fig. 50 a theodolite is able to see the CAM Cube, MaRi Cube and OGSE Cube, a schematic representation of this setup can be found in Fig. 5. During the measurement, the LoS of all 3 references can be seen in the theodolite window. A schematic representation of the 3 crosshairs can be seen in Fig. 51a, as well as an approximation of the Theodolite's FoV. Finally, in Fig. 51b the real 3 crosshairs as seen by the theodolite.

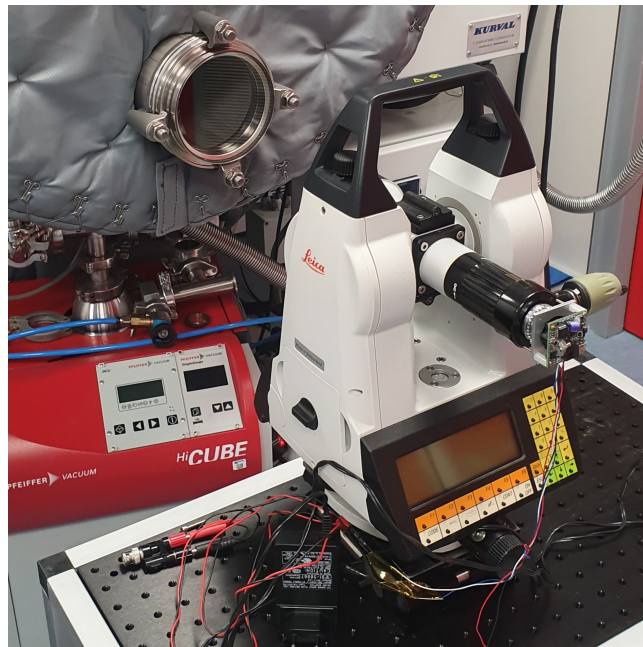
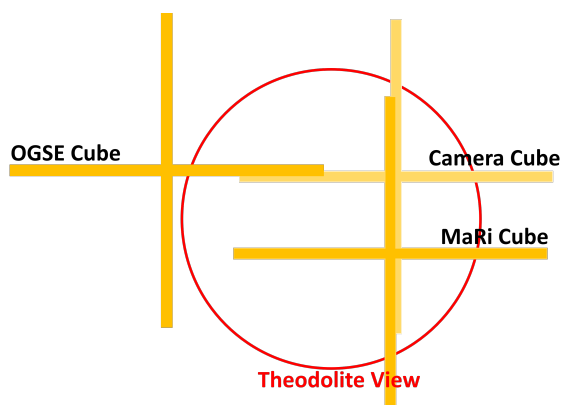
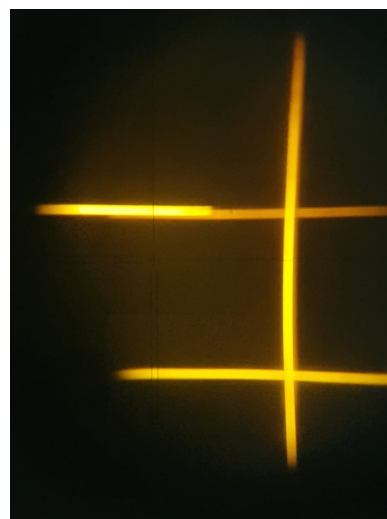


Figure 50: External alignment using the theodolite as explained in Sec. 1.3.1.



(a) Schematic overview of return crosshairs.



(b) Theodolite view.

Figure 51: Measurements during external alignment.

A.6 Validation

A.6.1 Bake-out

Offset of Alignment Cube LoS with respect to Collimator LoS											
Before bake-out											
Hz			V			V1			V2		
deg	min	sec	deg	min	sec	deg	min	sec	deg	min	sec
0	26	19	0	7	57	89	54	19	89	46	16
0	26	14	0	7	58	89	54	15	89	46	17
0	26	15	0	7	58	89	54	16	89	46	18
0	26	16,0	0	7	57,7						
After bake-out											
Hz			V			V1			V2		
deg	min	sec	deg	min	sec	deg	min	sec	deg	min	sec
0	26	7	0	8	1	89	54	22	89	46	21
0	26	11	0	8	4	89	54	26	89	46	21
0	26	12	0	8	1	89	54	23	89	46	22
0	26	10,0	0	8	2,0						
Difference of before/after bake-out											
ΔHz			ΔV								
deg	min	sec	deg	min	sec						
0	0	6,0	0	0	0						

V1 = Vertical theodolite measurement 1
 V2 = Vertical theodolite measurement 2
 Hz = Offset in vertical theodolite measurements
 V = Offset in horizontal theodolite measurements

Figure 52: Offset of fold flat LoS with respect to Collimator LoS

A.7 Recommendation Input Optics

One of the most important interface of the collimator is the input optics. Ensuring the pinhole plate to be illuminated and be coupled into the collimator. However, the coupling in of light is not part of this thesis. Integrating options have been investigated and a possible solution has been presented.

Illumination of the pinhole is proposed to a direct illumination of the interface through a fiber tip, housed in a SMA905 connector. This connector has to be positioned in front of the pinhole, with a given offset.

The suggested solution, as seen in Fig. 55, is proposed to be directly mounted to the xy flexure stage, Sec. 3.2.3. The internal thread of the Thorlabs stage, Fig. 13, houses the pinhole mount, Fig. 55a. The pinhole mount contains the pinhole plate, locked in place by a pretension ring.

Mounting the fiber connector a "connector receiver" can be built, Fig. 55a. This receiver could be retained using the SMA905 fiber connector retaining ring, resulting in the connector and its receiver to have a rigid structure.

The connector and receiver can be locked into place using a connector lock. Using the inner thread of the xy flexure stage, Sec. 3.2.3. This ensures easy placement and removal of rigid fiber connector - receiver pair.

Introducing the required distance of the pinhole plate with respect to the fiber tip can be achieved. By first measuring the distance "Interface Surface - Pinhole Plate", Fig. 55b and tuning the distance "Fiber Tip - Interface Surface" post process.

Light input via the fiber, is now rigidly connected to the pinhole and moves as the pinhole itself moves. Ensuring correct alignment if the initial integration has been done correctly.

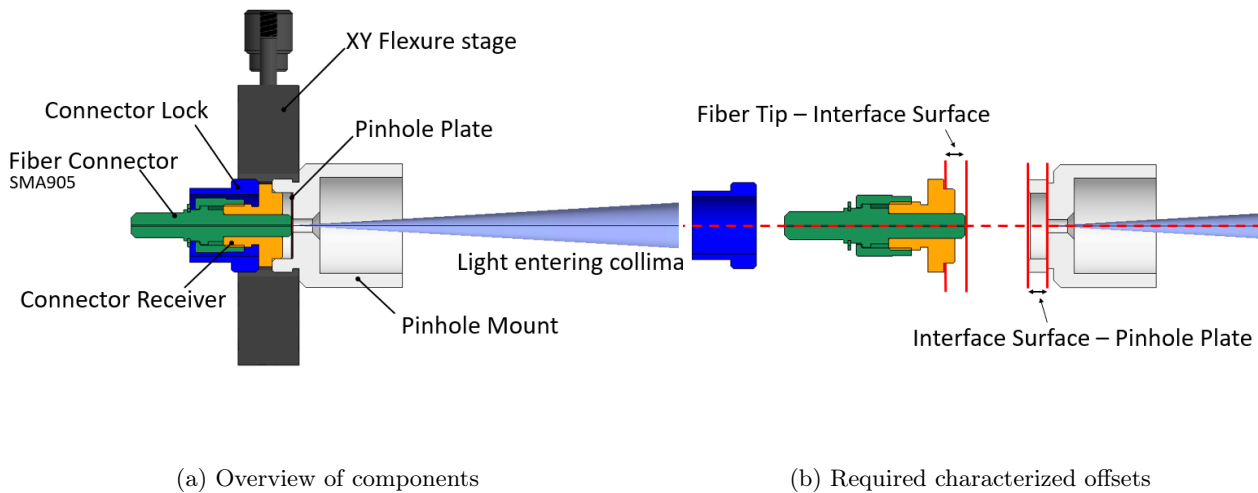


Figure 55: Proposed input optics fiber coupling